Water in *Pinus radiata* wood secondary cell walls:

An investigation using Nuclear Magnetic Resonance and Synchrotron X-ray Diffraction.

By

Stefan James Hill

A thesis
submitted to the Victoria University of Wellington
in fulfilment of the requirements for the degree of
Doctor of Philosophy
in Chemistry

Victoria University of Wellington
2010

Abstract

The mechanical properties of wood allow it to be used for numerous purposes. For most purposes, drying of the wood material from the green state, sawn from the log, is first required. This drying step significantly improves the strength properties of wood. It is therefore clear that moisture in wood plays an important role in determining the bulk mechanical properties. Over the last century, many studies have been carried out to investigate the way in which the water content wood affects the bulk mechanical properties. More recent studies have focused to the individual chemical components that make up wood to understand the observed changes in bulk mechanical properties. Models of the nanostructure of wood contained; *cellulose*, *hemicellulose*, and *lignin*, and the arrangement and location of these components in terms of their mechanical properties was interpreted through what was described as the 'slip-stick' mechanism, by which wood, in its green state, maintained its molecular and mechanical properties under external stresses. This model, while insightful, failed to account for the presence and the role of water in the nanostructure of wood.

In this work, synchrotron based X-ray diffraction and NMR studies, have been used to develop a new model, in which water plays a vital role in the determination of the mechanical properties of wood in its green, part-dried, and rewet states. X-ray diffraction showed that changes occur to the molecular packing of cellulose crystallites with change in moisture content, and that these changes begin to occur under mild drying conditions, *i.e.* drying in air at ambient temperatures. These changes depend on the severity of drying, whether ambient or forced oven drying, and are to some extent reversible. A spin-diffusion model was constructed using dimensions obtained from X-ray diffraction, comparisons between predictions and experimental data from an NMR study showed that the location of water was dependent on the moisture history of wood. In the green state, at least some of the water in the wood cell wall forms a layer, between the cellulose crystals and the hemicellulose and lignin matrix. If dried and then rewet, this water associated with the cellulose crystals was not present to the same degree as in the green state, allowing a closer association of the hemicellulose with the cellulose. The effect of this change in water distribution in the wood cell wall on the bulk mechanical wood properties was shown in mechanical testing. The nanostructure of the wood cell wall therefore should be considered to contain *cellulose*, *hemicellulose*, *lignin* and *water*, where each component contributes, according to its molecular properties, dynamic mechanical properties which are reflected in the bulk material properties.

Acknowledgements

I would like to first thank Drs Roger Newman and Robert Franich for their tireless and greatly appreciated efforts to keep the work and resulting thesis on track focussed. Roger always made time to discuss my work and resulting issues and never seemed to become disheartened by some of my more “interesting” conclusions. Roger and Christine’s invitation to spend part of Christmas with them so I could continue writing and still have access to Roger’s knowledge and guidance was appreciated more than words can express. Robert’s unending enthusiasm for this work was inspiring when things seemed dim and dark, and his critique of the thesis was invaluable in producing a document that I was truly happy with.

Without the financial support and flexible working environment supplied by Drs Elspeth MacRae and Tom Richardson over the last five years, none of this would have been anything other than “an interesting idea”, and my thanks go to them both. Yet even with a good idea, great local supervisors, and funding, again this project would not have been possible without the assistance of my third supervisor, Professor Sir Paul Callaghan. Professor Callaghan is a bit of a science folk-hero in New Zealand, and the chance to have him part of this undertaking was a heartening endorsement of what was intended to be done.

I would like to thank Bridget Ingham for her offer to carry out some initial synchrotron work on my behalf and for accompanying me to the Australian Synchrotron where I carried out a bulk of the X-ray work. On that note I would like to thank Nigel Kirby, Stephen Mudie, and Adrian Hawley of the Australian Synchrotron for all their help getting me underway and helping produce some truly amazing X-ray diffractograms.

Besides the academic support during these five years, I have had numerous people keeping my head up in the hard times and there to share in the triumphs (even if they didn’t fully understand them). The difficulty with composing such a list is they invariably end up missing some important persons, or ending up with an acknowledgements section larger than the thesis. To those not mentioned, I nonetheless appreciated your collegiality and friendship.

In particular, I want to thank Marie Joo Le Guen for helping keep the home life as smooth and restful as possible, also for keeping me well fed on French food. Christine Newman’s encouraging words to keep me on track and even with problems of her own she found the time to support my sometimes flagging morale. Christine is an amazingly strong and caring person.

I would also like to thank Professor Brian Nicholson for his kind words at the outset of this project. His opinion carried a lot of weight with me and his support was greatly received.

To Peugeot I thank you for your complete lack of interest in the maelstrom that was me at home – demanding no more than your (entitled) three meals a day. Cats have a great way of grounding people in reality and making it clear that troubles you may have aren't as important as their very feline existence.

Lastly, I would also like to thank my parents, Vernon John and Agnes Hill for their unfailing support. Never once did they question my sometimes questionable decisions in life. They gave me the freedom and drive to do the things I have wanted to do in life.

Addendum

Sadly Christine passed away before I defended this work in an oral examination. She therefore did not get to see that her efforts to educate me in correct English grammar were rewarded. I would like to think that somewhere she has a smile on her face at the outcome, and isn't too disappointed that I snuck in a couple of extra commas.

Preface

The work presented in this PhD thesis was carried out part-time over a five year period at Scion (Rotorua, New Zealand), where I am currently employed as the NMR spectroscopist and research chemist. The project was kindly funded by Scion Capability funding, initially under auspices of Dr Tom Richardson, and later Dr Elspeth MacRae. Specific funding for the synchrotron X-ray work was derived from a contested capability fund awarded to Dr Roger Newman to further his work on nanobiotechnology.

Parts of this thesis have been previously presented at conferences as either a verbal or poster presentations. Of note, the initial synchrotron results were presented at the New Zealand Microscopy conference in 2009, and the oral presentation was awarded the 'Keith Williamson medal for excellence in microscopy research'.

To date two publications in peer reviewed journals have been obtained from work in this thesis.

Work presented in this thesis has been published in the New Zealand Journal of Forestry Science reporting the initial evidence for the existence of water separating the cellulose microfibrils from the matrix in wood secondary cell walls. The location, distribution, and function of this water structure were the foci of the thesis.

Hill SJ, Franich RA, Callaghan PT, Newman RH. *Nature's nanocomposites: a new look at molecular architecture in wood cell walls.* New Zealand Journal of Forestry Science, 39(2009) 251-257.

A follow up article with final results is planned after submission of the thesis.

During the investigation of the role water as a functional component in wood, it was discovered that even at the level of the cellulose crystallites conformation, water has an effect. This effect on the cellulose crystallites has been accepted for publication in the journal Holzforschung.

Hill SJ, Kirby NM, Mudie ST, Hawley AM, Ingham B, Robert A. Franich RA, Newman RH. *Effect of drying and rewetting of wood on cellulose molecular packing.* Holzforschung, in press (2010).

Water in *Pinus radiata* wood secondary cell walls:

An investigation using Nuclear Magnetic Resonance and Synchrotron X-ray Diffraction.

List of Figures

Chapter 1

Chapter 2

Chapter 3

Chapter 4

Chapter 5

Chapter 6

Appendix A

Appendix B

Appendix C

Appendix D

Appendix E

List of Tables

Chapter 1

Chapter 2

Chapter 3

Chapter 4

Chapter 5

Chapter 6

Appendix D

Appendix E

List of Abbreviations

%MC	percent moisture content
CELL	cellulose
CP-MAS	cross-polarisation magic-angle spinning
DMTA	dynamic mechanical thermal analysis
DRW	double radial cell wall thickness
EMC	equilibrium moisture content
EW	earlywood
FESEM	field emission scanning electron microscopy
FID	free induction decay
LD	lumen diameter
LW	latewood
MOR	modulus of rupture
NMR	nuclear magnetic resonance
P2VPy	poly-4-vinyl pyridine
PAN	poly-acrylonitrile
PE	poly-ethylene
PEG	poly-ethylene glycol
PEO	polyethylene oxide
PMMA	poly-methyl methacrylate
PPO	poly-propylene oxide
PS	poly-styrene
RF	radio frequency
RMS	root mean square
SAXS	small angle X-ray scattering
TEM	transmission electron microscopy
VCT	variable contact time
VSL	variable spin lock
WAXS	wide angled X-ray scattering

“If we lived on a planet where nothing ever changed, there would be little to do. There would be nothing to figure out. There would be no impetus for science. And if we live in an unpredictable world, where things changed in random or very complex ways, we would not be able to figure things out. Again, there would be no such thing as science. But we live in an in-between universe, where things change, but according to patterns, rules, or, as we call them, laws of nature. If the sun sets in the west, it always rises in the east. And so it becomes possible to figure things out. We can do science, and with it we can improve our lives.”

Carl Sagan (Cosmos)

1 General introduction

1.1 Introduction

It has long been known that individual wood fibres have differing mechanical properties when dried and rewet compared with those of never-dried (Klauditz et al. 1947). Therefore, it seems reasonable to extrapolate and propose that the mechanical properties of timber will be also affected by dry-wet cycling. Little work however has been presented in this area in peer-reviewed literature, some of which may be questionable due to sampling methods and specimen selection choice (Tiemann 1906). This thesis will test a hypothesis that changes to the distribution of water within the wood cell wall nanostructure can help explain the observed differences in the mechanical properties of wood in the never-dried, dried, and rewet states.

The dry wood cell wall model (Model 1, Figure 1.1) is inadequate, and a wet wood cell wall model (Model 2, Figure 1.3) is needed in order to relate mechanism of hydrated-state and bulk material mechanical properties.

In order to probe the nanostructure of wood cell walls in the never-dried (*i.e.* green), fully-hydrated, dried, and rewet states, complementary methods of X-ray scattering and nuclear magnetic resonance spectroscopy were used. Stress-relaxation mechanical testing of small specimens of latewood bulk material was used to characterise the properties as a consequence of change in the hydration state of lignocellulosic materials.

1.2 Background

Effects of drying on wood

Kiln drying of green wood at elevated temperatures generally causes a decrease in the material modulus of rupture (MOR) among other material properties, compared with that of passively-dried wood carried out under ambient conditions (Kozlik 1976; Gerhards 1979). The decrease in this important mechanical property has been shown to be severe in some wood species with, e.g., MOR decrease of *ca.* 55% when Southern Pine wood was dried at 115 °C drying relative to drying at 23 °C (Millett and Gerhards 1972). In addition the heating process during drying is also known to affect the hygroscopicity of the wood, where the reduced ability of heated wood to re-uptake water is seen as a reduction in the equilibrium moisture content (EMC) as the drying temperature increases (Spiller 1948; Kininmonth 1976). The reduction to the EMC and reduction in MOR due to drying suggests that these changes in mechanical

properties are in part due to modifications occurring at the supra-molecular level. These changes occur in the cell wall components of cellulose, hemicellulose, and lignin with a re-organisation resulting in an increased brittleness and an altered hydrogen-bonded nano-molecular network assembly.

It has been shown that there is a hysteresis effect caused by water desorption and resorption on lignocellulosic polymers in wood. This effect during moisture content change is dependant not only on the amount of water lost or resorbed, but also on the direction of moisture content change, i.e. of adsorption or desorption process. Adsorption (i.e. moisture content increased from a dry state) results in material having an increased modulus of rupture and increased modulus of elasticity compared with the dry starting material. This has been attributed to "coupling and decoupling" of hydroxyl groups on the cellulose structure (Ishimaru et al. 2001).

This change in the hydrogen-bonded assembly has been demonstrated in a model system by solid state ^{13}C NMR where the hemicellulose chains are seen to "straighten" and adhere to the cellulose crystal surface (Newman and Hemmingson 1998). This can be visualised in terms of molecular Velcro® theory.

Molecular Velcro® theory

Wood has been found to have a remarkable property when wet. When stretched beyond the elastic limit wet wood shows irreversible deformations and yet does not flow as plastics do (Keckes et al. 2003). As soon as the excess stress is released the original stiffness is restored. In other words wet wood shows permanent plastic deformation without significant mechanical damage. This behaviour is known as "stick-slip" deformation and has been compared to Velcro® mechanics (Kretschmann 2003). When Velcro® is deformed beyond a yield point the hooks open and slip until the excess stress is released, the hooks then close on a different set of loops. The outstanding question is what components of the wood cell wall correspond to the hooks and loops of Velcro®? The stick-slip deformation process challenges our current understanding of the molecular architecture of wood when wet. In this thesis a new model of the wood cell wall is proposed, when wood material is wet, that takes into account the role of water not simply as molecules of hydration of the lignocellulosic polymers, but molecules with a structure of their own, which can carry and distribute an applied force, and which display the dynamics of molecular Velcro®.

The extant wood cell wall model

The earliest model of a wood cell wall showed microfibrils of crystalline cellulose wound in helical springs and embedded in an amorphous matrix of hemicelluloses and lignin (Mark 1965; Cowdrey and Preston 1966; Frey-Wyssling 1968). This model provided satisfactory foundations for calculations of the elastic properties of dry wood (Cave 1968), but it did not seem adequate to explain the strength of wet wood. This problem was later addressed by suggesting that hemicellulose chains act as coupling agents between cellulose microfibrils and lignin (Page 1976). Incorporated into this idea was a three-phase model for a wood cell wall, with partial segregation of the lignin-hemicellulosic matrix into a hemicellulose-rich region adjacent to the cellulose and a lignin-rich region remote from the cellulose (Ruel et al. 1978). Partial segregation of hemicellulose from lignin was retained in more recent models (Bergander and Salmen 2002; Gravitis 2006). The idea of partial segregation has been refined by distinguishing between the two major hemicelluloses, i.e., glucomannan and xylan. Dynamic infra-red spectroscopy indicated close cooperation between glucomannan and cellulose molecules, but no mechanical interaction between xylan and cellulose (Akerholm and Salmen 2001). The current model for a softwood cell wall (Model 1, Figure 1.1) is not greatly different from that proposed by Page (1976), except for the different locations of glucomannan and xylan.

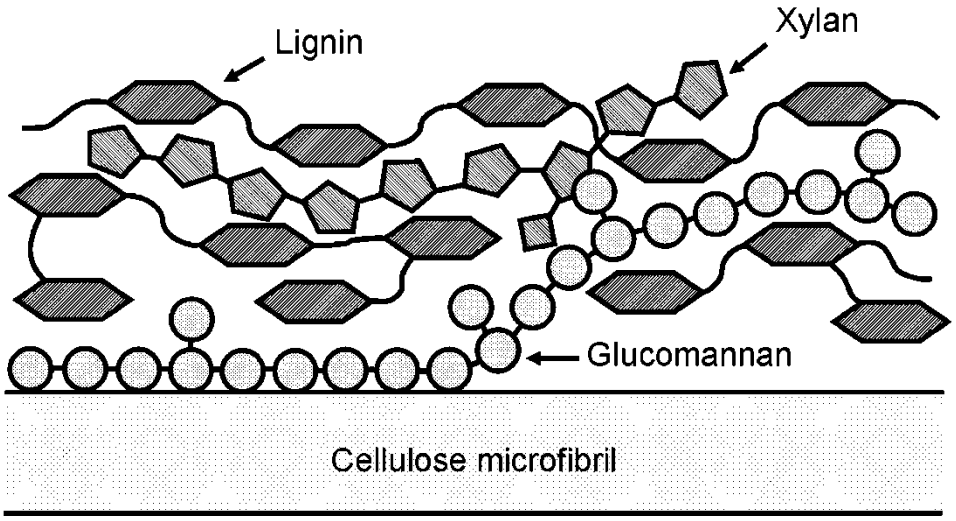

Figure 1.1 *Model 1 for a softwood cell wall has an interface between a cellulose microfibril and the adjacent matrix, in this case showing a glucomannan chain locking the components together as suggested by Page (1976).*

The commonly-cited model accounts for strength of wet wood with hemicellulose acting as a coupling agent between cellulose and the matrix (Page 1976), but it does not account for the stick-slip deformation observed (Keckes et al. 2003).

In a model which proposed that hydrogen bonding between hemicellulose and cellulose imparts a self-repair mechanism, likened to Velcro® (Keckes et al. 2003; Kretschmann 2003), Keckes and Kretschmann proposed that any change in molecular spatial arrangement of the cellulose-hemicellulose polymers is *via* a change in their hydrogen-bonding network. Initially by a "tearing" of the hydrogen bonds (the 'rip') in response to an applied force occurs, followed by translation of the polymer chains relative to each other (the 'slip'), and finally a reattachment of the hydrogen bonding network (the 'stick'). A graphical representation based on the Velcro® theory description is given as Figure 1.2.

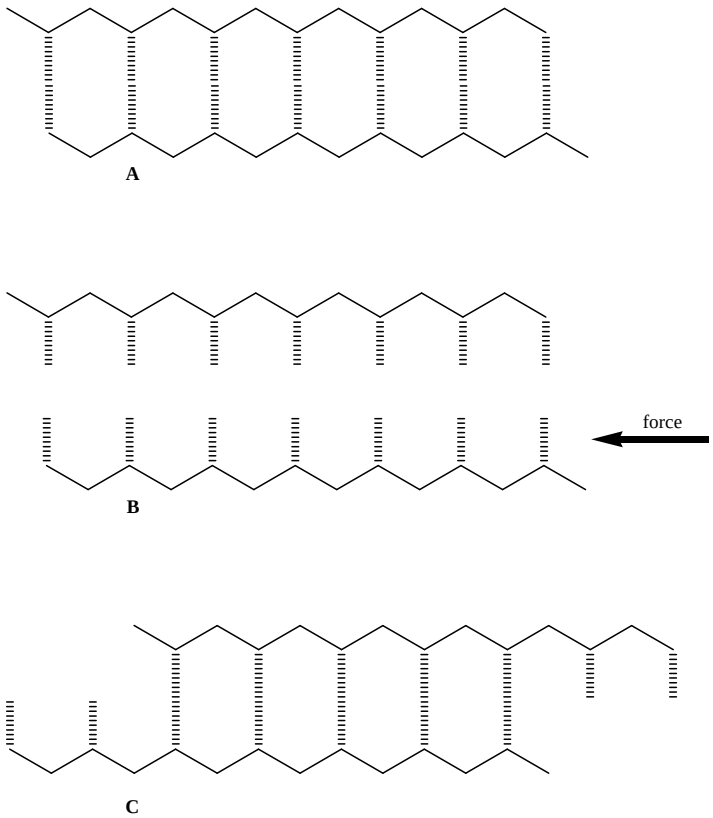

Figure 1.2 *"Rip, Slip, and Stick" model of molecular translation in a lignocellulosic material. From the initial hydrogen bonding conformation (A), a force is applied that causes the hydrogen bonded network to separate (B), then after the force has ceased, the hydrogen-bonding network reforms (C).*

While Model 1 (Figure 1.1) does not show glucomannan covalently bonded to either cellulose or lignin, the multiplicity of hydrogen bonds to cellulose and the entanglement with lignin seems unlikely to allow slippage at the cellulose-matrix interface. A single hydrogen bond is an order of magnitude weaker than a single covalent C-O bond linking two glucosyl structural units in cellulose, but given the multiplicity of hydrogen bonds between glucomannan and cellulose in the Model 1 (Figure 1.1), the likely response to shear force is a broken chain. Extracted glucomannan from spruce wood was reported to have a degree of polymerisation >60 (Lundqvist et al. 2003) so the

short chain shown in Model 1 (Figure 1.1) is a simplified representation. Given the energy required to disentangle tens of structural units from the matrix the likely response to shear force is again a broken chain. Stick-slip Velcro® mechanic deformation and recovery would require a weaker coupling between cellulose and matrix, relative to that represented by Model 1 (Figure 1.1).

1.3 Hypothesis

Water is the fourth structural component in the wood cell wall nano-composite, where its location and distribution has an impact on the bulk material mechanical properties.

The fibre saturation point

At fibre saturation point, *ca.* 30% moisture content by dry weight, the cell lumens are empty of water, yet the cell walls have the same water content as a never-dried specimen (Tiemann 1906). Given the hydrophilic nature of carbohydrates it is reasonable to assume that both the cellulose crystal surfaces and the non-acetylated hemicellulose will be in a hydrated state.

If we apply that to the previously presented model for the nanostructure of wood we end up with a model that has a layer, or layers, of water separating the matrix from the cellulose (Model 2, Figure 1.3).

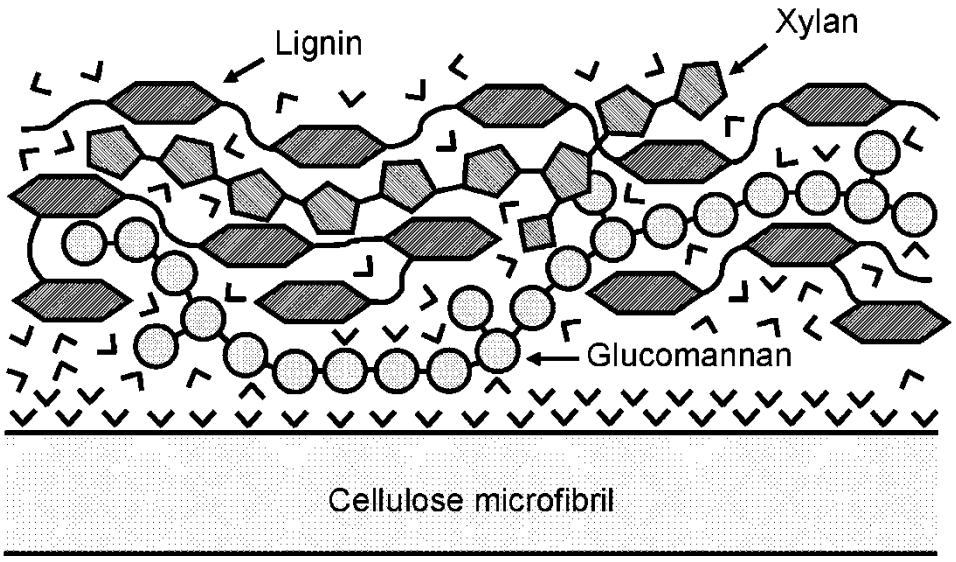

Figure 1.3 *Model 2 for a softwood cell wall has the interface between a cellulose microfibril and the adjacent matrix, with a layer of water molecules (v symbols) adhering to the microfibril.*

This model is consistent with the Velcro® mechanics theory the only difference being, that in the wet state the hooks and loops of the Velcro® are hydrogen bonded water rather than direct hemicellulose – cellulose interactions. In this hypothesis, as the

moisture content decreases from fibre saturation point, the number of direct hemicellulose – cellulose interactions increase, thereby changing the bulk material properties of the wood. Wood dried at high temperature, (e.g. 120 °C), shows an irreversible decrease in its equilibrium moisture content (Spiller 1948), which is understood to be due to co-crystallisation of hemicelluloses onto the cellulose surfaces, as represented in Model 1 (Figure 1.1). Depending on the severity of the drying conditions, the irreversible changes of equilibrium moisture content and MOR that occur can be accounted for in part, by the concept of changes in a water mediated Velcro® mechanics Model 2 (Figure 1.3).

Model 2 (Figure 1.3) shows a layer (or layers) of water molecules attached to the surface of the cellulose microfibril and permeating the hydrophilic regions of the matrix. This idea has been reported previously in the literature but those authors did not offer any experimental evidence (Hansen and Bjorkman 1998). Model 2 (Figure 1.3) differs from Model 1 (Figure 1.1) in another important detail in that the interaction between glucomannan and cellulose is confined to a short segment of the chain between structural units bearing side groups. In the case of softwoods the glucomannans bear galactosyl and acetyl side groups. It has been shown that the degree of acetylation of glucomannan influences the strength of sorption onto cellulose (Laffend and Swenson 1968). Solid-state NMR has been used to show that the acetylated segments of glucomannan in *Pseudotsuga menziesii* (Douglas fir) wood are intimately mixed with lignin, but remote from cellulose (Newman 1992). Hansen and Bjorkman pointed out that the solubility parameter for an acetylated hemicellulose increases its compatibility with lignin rather than with cellulose (Hansen and Bjorkman 1998). The overall conclusion from these observations is that side groups provide two independent mechanisms for limiting hydrogen-bonding coupling to cellulose:

1. Galactosyl side groups provide steric interference, hindering contact with the surface of the cellulose.
2. Acetyl groups promote incorporation of the glucomannan in the matrix. In Model 2 the stick-slip deformation occurs at the interface between a glucomannan segment and a layer of water molecules.

The representation in Model 2 (Figure 1.3) might remain valid for air-dried wood with an equilibrium moisture content of approximately 12% at 65% relative humidity. The final monolayer of water bonded to the surface of the cellulose microfibrils of wood is not removed until a much lower moisture content is reached by forced high-temperature drying (Weatherwax 1974). Complete removal of water would bring glucomannan into contact with cellulose and the hydrogen bonds thereby formed might not be easily

broken upon rehydration. There are literature references to support this idea, e.g., it was found that the wet strength of pulped wood fibres doubled when the fibres were dried and rewet (Klauditz et al. 1947).
Evidence for Model 2 (Figure 1.3), a dynamic wet cell wall model, will be acquired using X-ray diffraction and nuclear magnetic resonance (NMR) spectroscopy in order to test the stated hypothesis.

1.4 Instrumental techniques

Synchrotron based wide angled X-ray diffraction spectroscopy (WAXS) was used to measure the dimensions of the cellulose nano-crystals and to observe changes occurring due to differing moisture histories (see Chapter 2). A synchrotron light source with its extreme brilliance was required to achieve a good signal to noise ratio per unit time from wet samples. This allowed high-resolution diffractograms to be obtained with minimal time of sample exposure to the X-ray beam. This is important to reduce the chance of X-ray energy induced changes to the wood nanostructure or redistribution of water resulting from any localised heating.

Solid state NMR was used to measure the spin diffusion times between the matrix and the cellulose to test the hypothesis of moisture distribution. To do this the water in specimens was exhaustively replaced with deuterium oxide to create a spin diffusion barrier (see Chapter 4).

The effect of the redistribution of water in the nanostructure on the mechanical macro-properties of wood was tested using stress-relaxation mechanical testing (see Chapter 5).

1.5 Basic anatomy of softwoods stems

Pinus radiata is a conifer or cone-bearing tree. It shares with other conifers a relatively simple gross basic structure (Figure 1.4).

Figure 1.4 *Cross section showing the heartwood (darker middle) and sapwood (lighter).*

The growth rings are due to environmental, or more rightly, seasonal changes in cambial biosynthesis. These rings are the products of different cell structures grown in both the early part and the later part of the growing cycle. In the early part of the growing cycle the cells are larger in diameter compared with later, but have a much thinner secondary cell wall. The smaller diameter and thicker cell walls gives the latewood a slightly darker appearance compared to that of earlywood. However, colour must be used only as an indicator of latewood, as other factors can cause darker coloration, such as the presence of compression wood, or other defects. Wood material is deemed to be latewood if twice cell wall thickness equals or exceeds the diameter of the lumen (Mork 1928). As a tree matures the distance between growth rings decreases and there is an increase in the wood density. The outer wood of a mature tree also has a low microfibril angle, with the direction of the cellulose crystals being closer to that of the direction of the grain.

Figure 1.5 gives a scanning electron micrograph (SEM) indicating the cross sectional microstructures common to *Pinus radiata*.

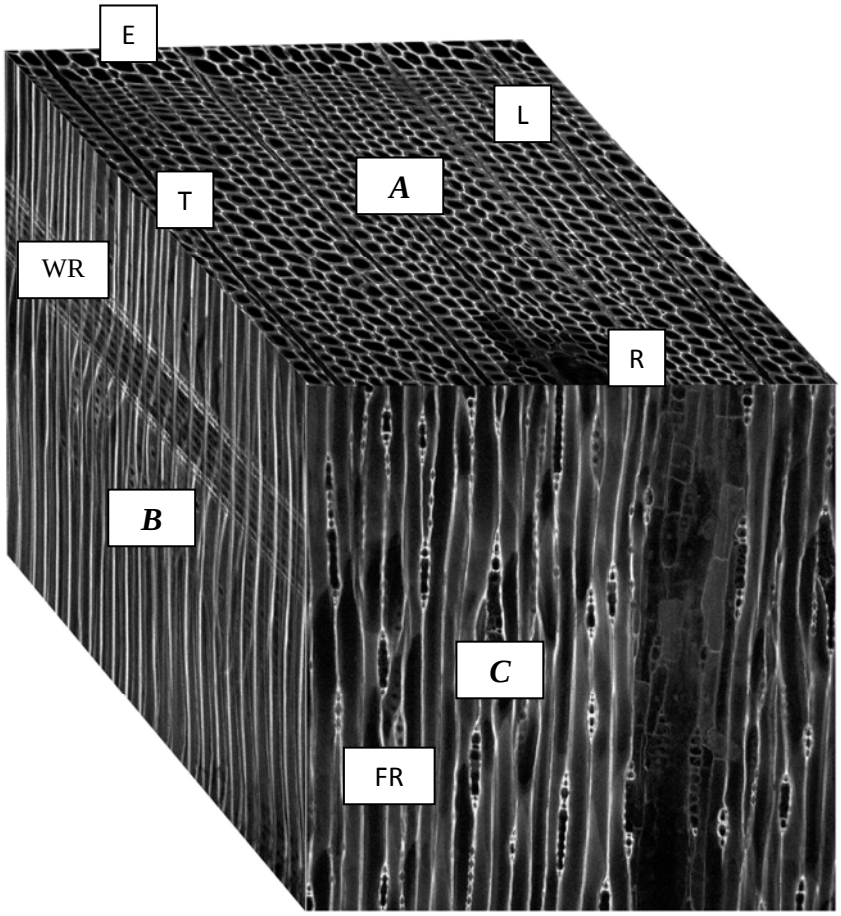

Figure 1.5 *SEM indicating the Transverse face (A), showing tracheids (T), latewood (L), earlywood (E), and resin canals (R). Radial/Longitudinal face (B), showing wood rays (WR). Tangential/Longitudinal face, showing fusiform rays (FR). Adapted from Kininmonth and Whitehouse (Kininmonth and Whitehouse 1991), picture courtesy of Dr Jacqueline Bond, Scion (2006).*

By choosing latewood from the outer growing edge of a mature tree, specimens of high density, high cellulose content, and a low microfibril angle can be obtained. This type of specimen is the optimum for the purposes of analysis by both X-ray diffraction and NMR spectroscopy. As previous studies have shown there are no significant differences between cellulose obtained from either latewood or earlywood pine by X-ray (Nomura and Yamada 1972) or solid state NMR (Newman 2004) methods. Results from these latewood specimens may be generalised to whole wood.

1.6 Chemistry of Softwood Stems

Although wood by no means has a consistent chemical composition, within limits typical values can be reported. These values have been obtained in most cases from

chemical extraction methods of increasing severity. In the first fraction is found the solvent extractable polyphenolics, resin, fatty acids (and esters), and alcohols. Lignin can then be analysed for from the remaining extractive-free wood by the hydrolysis of the remaining carbohydrates *via* the use of sulphuric acid. Alternatively the carbohydrate fraction can be isolated by oxidation using a chlorite treatment to remove the lignin and then alkali treatment to separate the hemicelluloses (such as xylan and glucomannan) and cellulose (Kininmonth and Whitehouse 1991). Typical values are given in Table 1.1.

Table 1.1 *Representative values for the chemical composition of Pinus radiata wood based on oven-dry weight (Kininmonth and Whitehouse 1991).*

Component	***% composition (wood)***
Extractables	
Non-polar	2
Phenols	*ca.* 0.1
Non-extractables	
Cellulose	40
Hemicelluloses	31
Lignin	27
Ash	*ca.* 0.2
Total	*100*

Further discussion of the main components, cellulose, hemicellulose, and lignin, along with the properties of water follows.

Cellulose

Cellulose is a linear chain polysaccharide, consisting of repeating β-(1→4) linked glucose units, with cellobiose (one di-glucose unit) being the repeat unit (Figure 1.6) (Collins and Ferrier 1995).

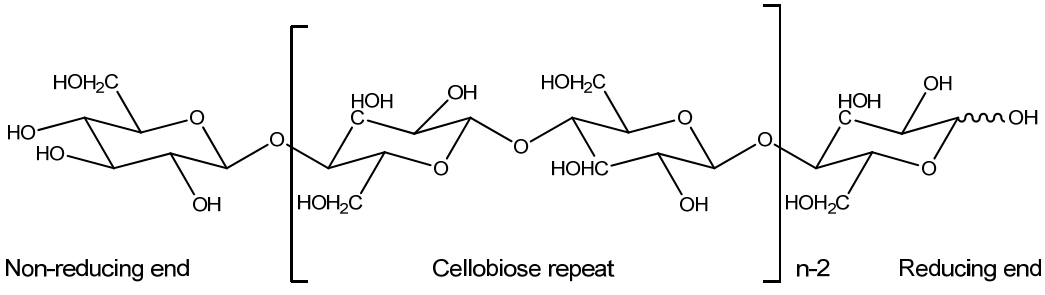

Figure 1.6 *Chemical structure of cellulose, β(1→4) linked glucose pyranose residues. Repeating units are comprised of cellobiose.*

The general numbering scheme adopted for use with carbohydrates, as shown for the monosaccharide β-D-glucopyranose, is given below as Figure 1.7.

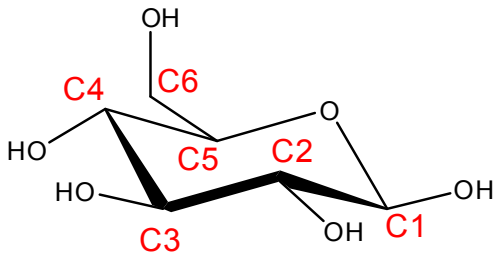

Figure 1.7 *Carbon numbering used for carbohydrates (as shown for β-D-glucopyranose).*

From solid state NMR studies wood specimens from *Pinus radiata* have been shown to have both triclinic cellulose Iα and monoclinic cellulose Iβ existing in nearly equal proportions (Newman 1999). Both the Iα and Iβ forms have similar fibre repeat distances of 1.040 nm and 1.038 nm respectively (Nishiyama et al. 2002; Nishiyama et al. 2003). The differences between cellulose Iα and Iβ is in the crystal fibre repeat direction with cellulose Iα having a staggered conformation between chains (Figure 1.8) (Sugiyama et al. 1991; Nishiyama et al. 2002; Nishiyama et al. 2003).

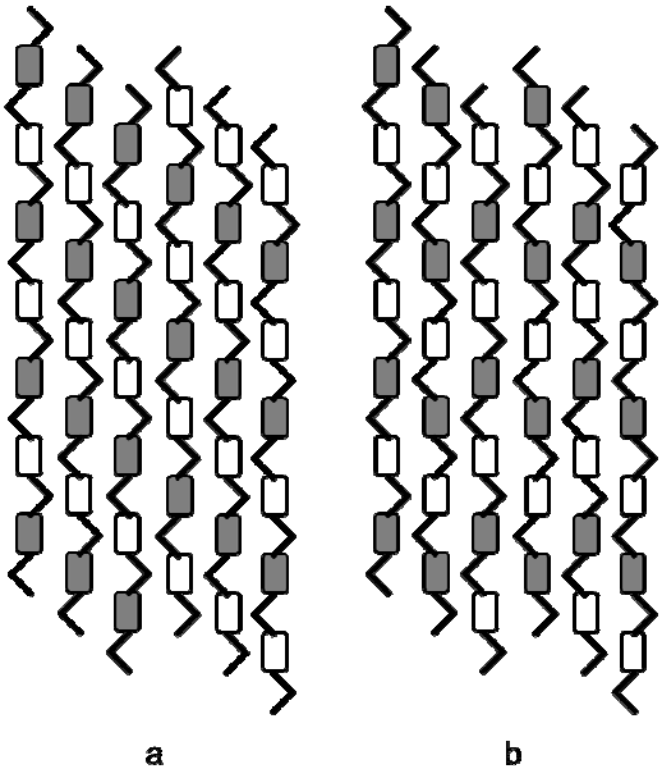

Figure 1.8 *Conformation of (a) cellulose Iα and (b) cellulose Iβ [rectangles = glucose units, < & > = β1→4 linkages].*

There is little evidence to support the existence of amorphous cellulose as reported in the literature. It has been reported as likely to be a result of mechanical damage or wood pulping treatment rather than being a state of native cellulose (Newman et al. 1993; Kim and Newman 1995). It is likely that wood cellulose exists in more complex and varied conformational states than pure cellulose (Newman 2003). Crystalline cellulose can be sub-divided into crystal-surface and crystal-interior, and then the crystal-surface into "well ordered" and "poorly ordered" crystal domains (Newman and Hemmingson 1994).

The differences in cellulose crystal environments have been well studied by the use of solid-state magic angle spinning NMR. These experiments have shown a difference in the:

- Chemical shifts (Earl and VanderHart 1981)
- Carbon spin-lattice relaxation time constants, T_{1C} (Hirai et al. 1990)
- Rotating frame proton spin-lattice time constants, $T_{1\rho H}$ (Newman et al. 1993)
- Proton spin-spin time constants T_{2H} (Callaghan et al. 2005)

These differences arise due to differing degrees of freedom for molecular motion to occur. The cellulose interior has a much more restricted environment to motions such as rotation, whereas on the surface the cellulose chains have more freedom to move (Newman and Davidson 2004). The nature of this increased mobility on the surface could be considered to be a reflection of the incomplete intramolecular cellulose-cellulose hydrogen bonding, having the effect of diminishing the rigidity of the cellulose structure by the allowance of chain twisting (Vietor et al. 2002) (Figure 1.9).

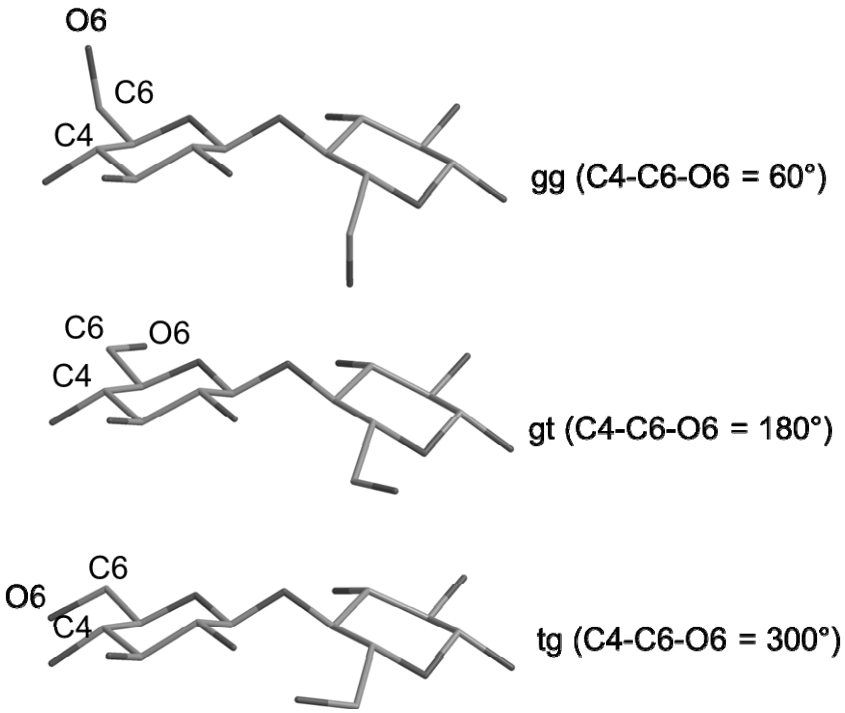

Figure 1.9 *Cellulose C4-C6-O6 torsion angle conformations (gt = gauche-trans, gg = gauche-gauche, tg = trans-gauche).*

In the case of the *gauche-trans* (*gt*) and *gauche-gauche* (*gg*) conformations, hydrogen bonding of the O6H6 is possible with adjacent molecules. For example in the case of the *gg* intramolecular hydrogen bonding between the O6 and an adjacent cellulose H2'–O2' can occur (Shen and Gnanakaran 2008). This has the effect of weakening intramolecular hydrogen bonding as compared with the *trans-gauche* (*tg*) cellulose conformer while increasing the rigidity of the cellulose chain. It has been found that at the cellulose crystal surfaces the conformations of *gt* and *gg* dominate and in the interior of the cellulose crystal *tg* is the preferred conformation (Newman and Davidson 2004).

Hemicelluloses

Hemicelluloses are defined as the alkali soluble carbohydrates removed after the cold/hot water soluble carbohydrates (pectic polysaccharides) were removed (Harris 2005). The function of hemicelluloses in cell wall architecture and mechanics has been speculated as serving the purpose of both assisting with load-bearing (Navi et al. 2005) and stopping the cellulose microfibrils aggregating after their biosynthesis (Hayashi et al. 1987).

The two major hemicellulose families present in *Pinus radiata* secondary cell walls are galactoglucomannans and 4-*O*-methyl-glucurono-arabinoxylans (Harris 2005). The

exact compositions of these hemicelluloses are variable, and it is more appropriate to refer to them as classes of carbohydrates under the terms mannans and xylans.

The structures of monosaccharide component monomers that make up hemicelluloses are given below as Figure 1.10 (Aspinall 1970).

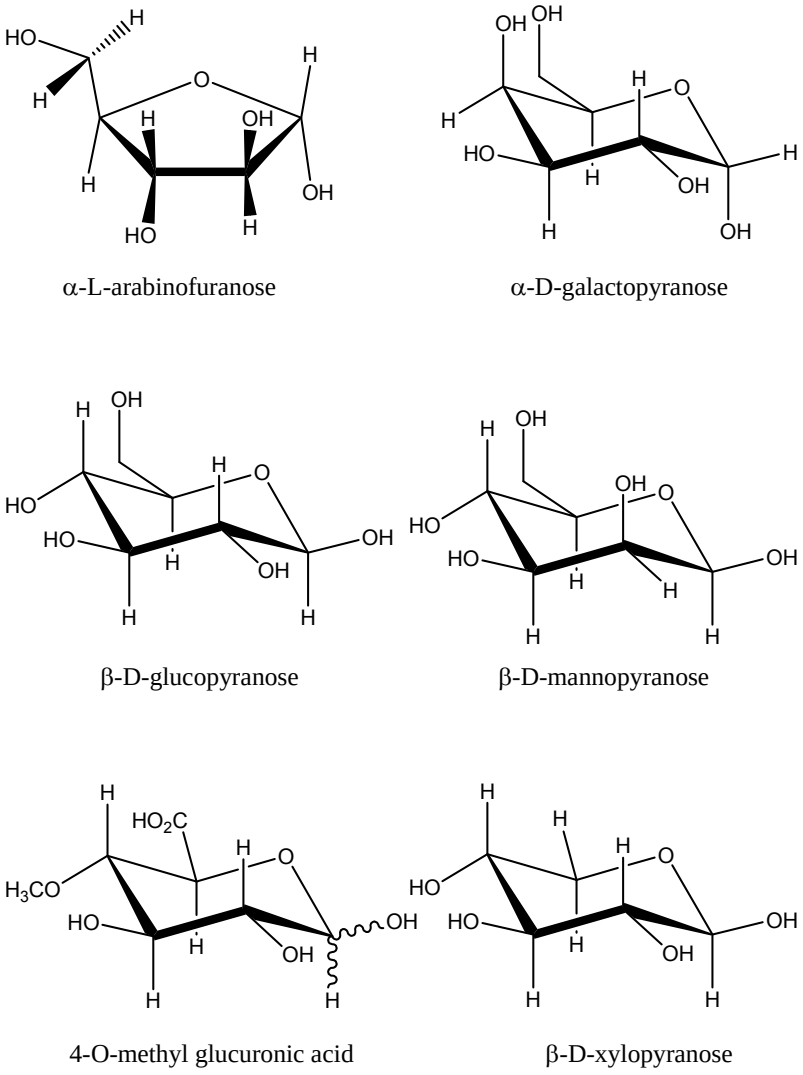

Figure 1.10 *Structures of the monosaccharides that are the building blocks for hemicelluloses (pyranose/furanose forms shown as present in softwoods).*

The function of the hemicelluloses is understood to be the glue that holds the lignin to the cellulose thus providing the mechanical strength of the wood. More recently, there has been an appreciation that the hemicelluloses may take a more active role in the wood structure and dynamics by regulation of the chemical architecture of the cell wall (Atalla 2005).

The spatial arrangement of hemicelluloses has been investigated by solid state NMR showing that glucomannan is deposited closer to cellulose than either galactoglucomannan or xylan (Newman 1992).

Softwood Lignin

Lignin is a polyphenolic polymer present at about *ca.* 30% by weight in *Pinus radiata* wood. The basic units of lignin are formed in softwoods from the enzymatic transformation of phenylalanine to *p*-coumaryl and coniferyl alcohols in a multi-step process (Vanholme et al. 2008). The structures of these alcohols are given in Figure 1.11.

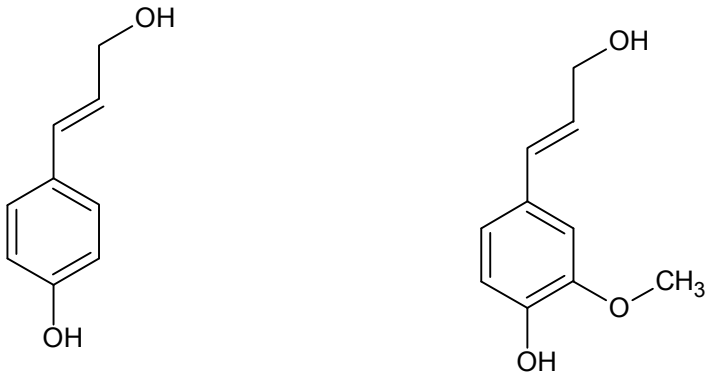

Figure 1.11 *Basic chemical precursor components of lignin, (A) p-coumaryl alcohol, (B) coniferyl alcohol.*

Lignin is a material difficult to define due to its complex and heterogeneous nature (Ralph 1997). There are two schools of thought on the formation of lignin. The first is that the structure is formed by an enzyme-mediated polymerisation (Gang et al. 1999), and the other that the formation of lignin is *via* an undirected enzyme initiated radical polymerisation (Boerjan et al. 2003). In the first case, dirigent proteins determine the structure of the lignin by controlling the radical coupling reactions, resulting in structure under genetic control. In the latter case, the formation of the lignin structure is due to chemically driven radial polymerisation reactions, resulting in a random structure.

To give a structure for lignin is not possible due to the high number of possible chain linking reactions that can take place (Kininmonth and Whitehouse 1991). Lignin sub-structures have been isolated and characterised resulting in over 480 compounds identified from lignin that are chemically distinct *via* solution state NMR techniques (Ralph et al. 2004), allowing representative structures to be drawn, in this case, for a softwood lignin (Figure 1.12).

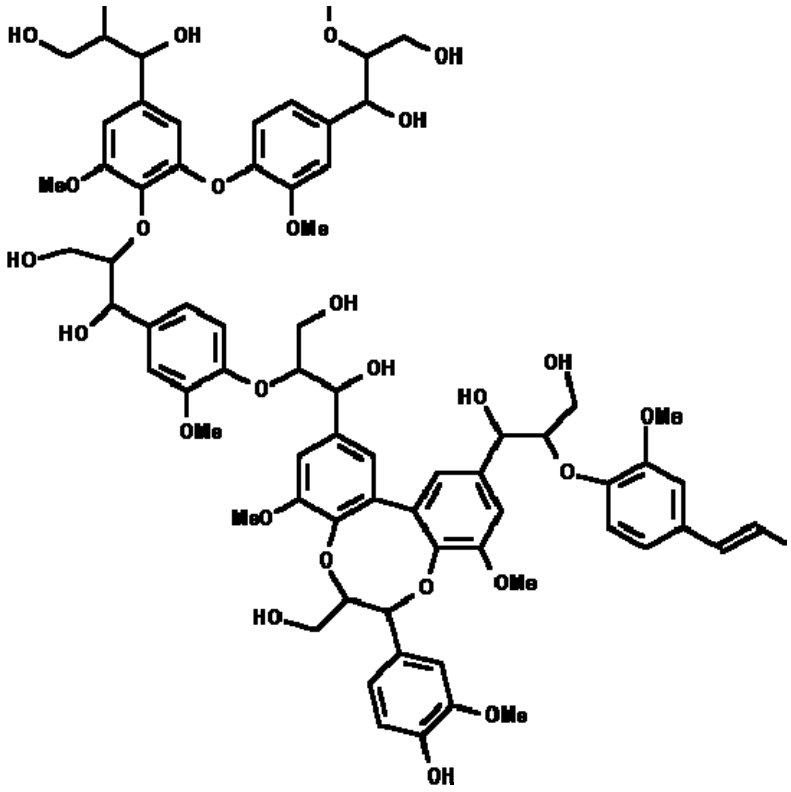

Figure 1.12 *Hypothetical sub-structure of a softwood lignin polymer.*

In the wood structure lignin and hemicellulose forms the matrix, within which the cellulose microfibrils reside. Lignin is also found covalently linked to carbohydrates and but mostly the polymer structure of lignin can be thought of as hydrophobic in nature (Kininmonth and Whitehouse 1991).

Water

Much has been written on the topic of hydrogen bonding in nucleic acids and proteins. Hydrogen bonding is paramount in determining the tertiary and quaternary protein structure, and therefore functions, of a protein. The role that hydrogen bonding plays in the structure and properties/functions of carbohydrates is less clear (Jeffrey 1992). It could be suggested that given the vast array of hydrogen bonding capable between and within groups present in carbohydrates, that hydrogen bonding plays some role in the determination of molecular structure and properties. Cellulose hydroxyl residues (up to three per carbohydrate moiety) can hydrogen bond with water. In the case of water interacting with carbohydrates there can be two cases envisioned.

The first is one in which the water/carbohydrate hydrogen bonding causes an individual water molecule to have a much lower diffusion coefficient compared to its non-hydrogen bonded counterpart. This type of water has been termed as “bound water”, although an exact definition of bound, *vs.* free or bulk water, is at best arbitrary. The

main problem is how to measure such interactions and how to decide at what level of association determines bound from non-bound water. The relatively simple hydrogen-bonding picture is complicated in wood carbohydrates by the presence of dissolved salts, carbohydrate-carbohydrate interactions, and other solutes (*e.g.* dissolved gases). Because of this a whole gambit of molecular interactions can occur and competition between them for available water is likely resulting in water redistribution with change in moisture content. Unlike small molecule carbohydrates, cellulose has less potential of hydrogen bonding with water due to steric considerations of the molecular polymer backbone. It has been shown that the greater the order in a carbohydrate system the greater the order there will be in the associated water structures (Hayashi et al. 2002).

Chaplin (Chaplin 2005) described the hydrogen bonding of water present in carbohydrates under five classes;

- Dense, strongly-bound water associated with disoriented strongly hydrogen-bonding groups and charged groups plus their counter ions.
- Low-density, weakly-bound water associated with dense water.
- Low-density, strongly-bound water associated with orientated strongly hydrogen-bonding groups.
- Low-density, weakly-bound water associated with hydrophobic groups.
- Unbound, compartmentalised water (as would be encountered in wood cell lumens).

Unlike non-carbohydrate groups, such as N/C=O functions, carbohydrate (hydroxyl) hydrogen bonding allows the possibility to form extended hydrogen bond networks to form due to an almost equal affinity of donor and acceptor.

Hydrogen bonding is a low energy (*ca.* 3-50 $kJmol^{-1}$) attractive force between atoms, which occur predominately between compounds containing oxygen, nitrogen, or fluorine, and the protonated form of each such atom. Hydrogen bonding can occur in all three common phases of matter (solid, liquid, or gas), and indeed forms part of the mechanism for many chemical reactions. The lifetime of this bonding depends upon the donor and the acceptor atom, but usually is in the order of picoseconds (10^{-12} s) (Smith and March 2001). Hydroxyl to oxygen hydrogen bonding has energies in the order of 12-25 $kJmol^{-1}$, compared with that of covalent bonding oxygen to hydrogen of some 460 $kJmol^{-1}$. An array of hydrogen bonds has a greater energy than the simple sum of the number of hydrogen bonds involved in the array (Jeffrey 1992). Two types of hydrogen bonding have been designated:

- Strong, with a narrow bonding length of 1.2-1.5 Å.
- Weak, with a broad bonding length range of 1.5-3.0 Å.

In the case of the strong hydrogen bond the bond length and bond energy can become comparable to a covalent bond (Jeffrey 1992).

The hydrogen-bonding present in water is both enhanced and ordered by the ionisation of water. At the pH found in softwood (pH *ca.* 4-6) (Campbell and Bryant 1941), there is about an 80 fold increase in the presence of H_3O^+ ion compared to a neutral solution (at 25 ^oC). These oxonium ions consist of three protons covalently bound to an oxygen atom, and have C_{3v} symmetry (i.e. the protons are all equivalent). These H-O bonds are slightly shorter than normal H-O-H bonds (0.961 Å verses 1.002 Å), and have a flattened trigonal pyramidal structure with an H-O-H angle of 114.7^o, compared with the same angle in H_2O being 106.7^o (Hermida-Ramon and Karlstrom 2004). This flattened structure can not only act to form three hydrogen bonds stronger than a water/water hydrogen bond but the shallow pyramid can invert, allowing rotation in a hydrogen bond cluster with minimal energy barriers (*i.e.* less than breaking or rotating about a hydrogen bond).

Another property is that the extra proton can be delocalised and shared over several water molecules. This proton sharing forms islands of stronger hydrogen bonding within the bulk liquid water. Figure 1.13 gives the proposed resonance structures for $H_7O_3^+$. It is suggested that once a favourable orientation is reached the energy barrier for the transfer of the proton is quite small (Marx et al. 1999).

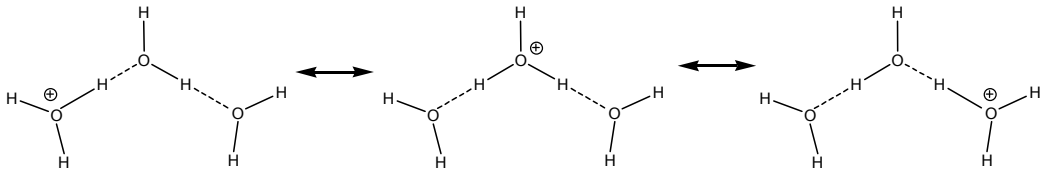

Figure 1.13 *Proposed resonance structures of $H_7O_3^+$ (Headrick et al. 2005).*

Given the high proportion of water present in green wood, it seems likely that water may play a role in the determination of the wood nanostructure. It then follows that perturbation of these water structures would result in changes to the wood nanostructure and ultimately the wood mechanical properties.

1.7 Project Goals

Nanocomposite materials composed of Nature's polymers (e.g., carbohydrates, proteins, polyphenols, and minerals) also have as an intimately involved component molecules of water interleaved and hydrogen bonded within their structures.

The goal of the project was to understand the role that water plays in the structure, the viscoelastic, and dynamic properties of the natural nanocomposite material, wood.

The fundamental importance of molecular interactions in biological nanocomposite materials with complex hierarchical architecture of fibrils and matrices is the basis of their remarkable mechanical properties. Their ability to respond when strained or perturbed, even in the case of wood, to recover mechanical properties after strain beyond the plastic limit.

The tertiary structure of carbohydrates is controlled by bond angles and chirality of the inter-atomic covalent bonds, van der Waals forces, and by intra-and inter-molecular hydrogen bonds in which the water content is a variable that may have a substantial influence on the mechanical properties of the material.

Understanding the nature of hydrogen bonding in hierarchical nano-composites composed of carbohydrates and polyphenols gives insight into the relationship of the bulk mechanical properties of natural materials. However the nature of intra- and inter-molecular bond changes (including the role of hydrogen bonding and of water) in natural nanocomposites undergoing dynamic change such as drying is not yet clear.

The importance that water plays in the form of dynamic hydrogen bonding has to date not been studied in depth relating to the overall mechanical behaviour of wood. In this thesis the effect of physical strain/stress on the composite material will be investigated from the point of view of the changes in the "water network" present between composite material polymer components. It is hypothesized that water hydrogen bonded between cellulose and the matrix can act in a load-bearing sense.

In the load bearing capacity the hydrogen bonds are translated via a "rip, slip, and stick" process similar to that termed molecular Velcro® theory. This theory proposes that the macro-dynamic behaviour of wood rich in hydroxyl groups can at least in part be ascribed to the translocation of the hydrogen bonding of the cellulose, microfibrils, and hemicelluloses in the matrix and not just simply the bending of the cellulose backbone. We propose that this translocation is mediated by water in wet wood.

This phenomenon was investigated by the techniques of synchrotron based X-Ray diffraction, solid-state nuclear magnetic resonance (NMR) spectroscopy, and mechanical testing. Specimens with a known history for this study were taken from a mature pine tree (*Pinus radiata*) from the latewood band closest to the bark layer in order to give the best signal to noise ratio per time given time unit from X-ray and NMR techniques. The project was divided into objectives in the following outline.

1.8 Thesis outline

Chapter 2 explores the dimensions of a cellulose crystallite for the purposes of developing a wood cell wall model. The dimension of the cellulose crystallite was estimate from wide angled X-ray scattering using a synchrotron light source. Aside from the dimensional data, it was found that the cellulose crystallite changes geometry in response to moisture content change, and this is explored in detail.

Chapter 3 presents a review of methods of applying NMR spectroscopic techniques to the investigation of polymer system by the use of a model high-density polyethylene polymer. The main NMR technique used for analysis was solid-state NMR proton spin-diffusion and various methods of gathering and, processing the NMR data are discussed. From the review, NMR methodologies to be applied to a solid wood system were selected.

Chapter 4 utilised information presented in Chapter 2 and Chapter 3 to develop two models for the distribution of water in the wood cell wall. One model proposed a random distribution of water, while the other proposed that water preferentially (but not exclusively) was localised about the cellulose crystallites.

Chapter 5 tests the two models presented in Chapter 4, by applying NMR methods developed in Chapter 3.

Chapter 6 tests the consequences of knowledge gained from Chapter 5 about the nanostructure of the hydrated wood cell wall by the use of mechanical testing (stress-relaxation) on bulk solid wood specimens.

Chapter 7 summaries the findings presented in the preceding chapters and draws conclusions from them.

1.9 References

Akerholm, M., Salmen, L. (2001) Interactions between wood polymers studied by dynamic FT-IR spectroscopy. Polymer. 42:963-969

Aspinall, G.O. Polysaccharides. Pergamon Press Ltd., Oxford, England., 1970

Atalla, R.H. (2005) The role of the hemicelluloses in the nanobiology of wood cell wall. The hemicellulose workshop. Entwistle, K.M., Walker, J.C.F. The Wood Technology Research Centre, University of Canterbury, Christchurch, New Zealand

Bergander, A., Salmen, L. (2002) Cell wall properities and their effects on the mechanical properities of fibers. Journal of Materials Science. 37:151-156

Boerjan, W., Ralph, J., Baucher, M. (2003) Lignin biosynthesis. Annual Review of Plant Biology. 54:519-546

Callaghan, P.T., Franich, R.A., Hill, S.J., Newman, R.H. (2005) Spin-echo CP/NMR for probing supramolecular structure in biological systems. Pacifichem2005. Hawaii.

Campbell, W.G., Bryant, S.A. (1941) Determination of pH in wood. Nature. 147:357

Cave, I.D. (1968) The anisotropic elasticity of the plant cell wall. Wood Science and Technology. 2:268-278

Chaplin, M. (2009) Water structure and behavior. Polysaccharide Hydration. London South Bank University. http://www1.lsbu.ac.uk/water/hydrat.html (09/09/2009)

Collins, P., Ferrier, R. Monosaccharides - Their chemistry and their roles in natural products. John Wiley & Sons Ltd, Chichester, England, 1995

Cowdrey, D.R., Preston, R.D. (1966) Elasticity and microfibrillar angle in the wood of Sitka spruce. Proceedings of the Royal Society B. 166:245-272

Earl, W.L., VanderHart, D.L. (1981) Observations by high resolution carbon-13 nuclear magnetic resonance of cellulose I related to morphology and crystal structure. Macromolecules. 14:570-574

Frey-Wyssling, A. (1968) The ultrastructure of wood. Wood Science and Technology. 2:73-83

Gang, D.R., Costa, M.A., Fujita, M., Dinkova-Kostova, A.T., Wang, H.B., Burlat, V., Martin, W., Sarkanen, S., Davin, L.B., Lewis, N.G. (1999) Regiochemical control of monolignol radical coupling: A new paradigm for lignin and lignan biosynthesis. Chemistry & Biology. 6:143-151

Gerhards, C.C. (1979) Effect of high-temperature drying on tensile strength of douglas-fir 2 by 4's. Forest Products Journal. 29(3):39-46

Gravitis, J. (2006) Nano level structures in wood cell wall composites. Cellulose Chemistry and Technology. 40(5):291-298

Hansen, C.M., Bjorkman, A. (1998) The ultrastructure of wood from a solubility parameter point of view. Holzforschung. 52:335-344

Harris, P.J. (2005) Non-cellulosic polysaccharides in plant cell walls. The hemicellulose workshop. Entwistle, K.M., Walker, J.C.F. The Wood Technology Research Centre, University of Canterbury, Christchurch, New Zealand

Hayashi, T., Marsden, M.P., Delmer, D.P. (1987) Pea xyloglucan and cellulose. Plant Physiology. 83:384-389

Hayashi, Y., Shinyashiki, N., Yagihara, S. (2002) Dynamical structure of water around biopolymers investigated by microwave dielectric measurements using time domain reflectometry method. Journal of Non-Crystalline Solids. 305:328-332

Headrick, J.M., Diken, E.G., Wlaters, R.S., Hammer, N.I., Christie, J., Cui, J., Myshakin, E.M., Duncan, M.A., Johnson, M.A., Jordon, K.D. (2005) Spectral signatures of hydrated proton vibrations in water clusters. Science. 308:1765-1769

Hermida-Ramon, J.M., Karlstrom, G. (2004) Study of the hydronium ion in water. A combined quantum chemical and statistical mechanical treatment. Journal of Molecular Structure: Theochem. 712:167-173

Hirai, A., Horii, F., Kitamaru, R. (1990) Carbon-13 spin-lattice relaxation behaviour of the crystalline and noncrystalline components of native and regenerated celluloses. Cellulose Chemical Technology. 24:703-711

Ishimaru, Y., Arai, K., Mizutani, M., Oshima, K., Iida, I. (2001) Physical and mechanical properties of wood after moisture conditioning. Journal of Wood Science. 47:185-191

Jeffrey, G.A. (1992) Hydrogen bonding in carbohydrate and hydrate inclusion compounds. Advanced Enzymology & Related Areas in Molecular Biology. 65:217-254

Keckes, J., Burgert, I., Fruhmann, K., Muller, M., Kolling, K., Hamilton, M., Burghammer, M., Roth, S.V., Stanzl-Tschegg, S., Fratzl, P. (2003) Cell-wall recovery after irreversible deformation in wood. Nature Materials. 2(810-814)

Kim, Y.S., Newman, R.H. (1995) Solid state ^{13}C NMR study of wood degraded by the brown rot fungus *Gloeophyllum trabeum*. Holzforschung. 49:109-114

Kininmonth, J.A. (1976) Effect of timber drying temperature on subsequent moisture and dimensional changes. New Zealand Journal of Forestry Science. 6(1):101-107

Kininmonth, J.A., Whitehouse, L.J. (1991) Properties and uses of New Zealand radiata pine. Forest Research Institute, Rotorua, New Zealand. Volume One - Wood Properties

Klauditz, W., Marscall, A., Ginzel, W. (1947) Zur technologie verholzter pflanzlicher zellwane. Holzforschung. 1:98-103

Kozlik, C.J. (1976) Kiln temperature effect on tensile strength of douglas-fir and western hemlock lumber. Forest Products Journal. 26(10):30-34

Kretschmann, D. (2003) Velcro mechanics in wood. Nature Materials. 2:775-776

Laffend, K.B., Swenson, H.A. (1968) Effect of acetyl content of glucomannan on its sorption onto cellulose and on its better additive properties. Tappi. 51:118-123

Lundqvist, J., Jacobs, A., Palm, M., Zacchi, G., Dahlman, O., Stalbrand, H. (2003) Characteriztion of galactoglucomannan extracted from spruce (*Picea abies*) by heat-fractionation at different conditions. Carbohydrate Polymers. 51:203-211

Mark, R. (1965) Tensile stress analysis of the cell walls of coniferous tracheids. In: Cellular Ultrastructure of Woody Plants. Ed. Cote, W.A. Syracuse University Press, New York. pp. 493-533

Marx, D., Tuckerman, M.E., Hutter, J., Parrinello, M. (1999) The nature of the hydrated excess proton in water. Nature. 397:601-604

Millett, M.A., Gerhards, C.C. (1972) Accelerated aging: Residual weight and flexural properties of wood heated in air at 115^{o} to 175^{o}C. Wood Science. 4(4):193-201

Mork, E. (1928) Die qualitat des fichtenholzes unterbesondere rucksicht nahme auf schied- und papierholz. Papier Fabrikant. 48:741-747

Navi, P., Plummer, C.J.G., Spycher, M., Heger, F. (2005) Role of hemicellulose in stress relaxation. The hemicellulose workshop. Entwistle, K.M., Walker, J.C.F. The Wood Technology Research Centre, University of Canterbury, Christchurch, New Zealand

Newman, R.H. (1992) Nuclear magnetic resonance study of spatial relationships between chemical components in wood cell walls. Holzforschung. 46(3):205-210

Newman, R.H. (1999) Estimation of the relative proportions of cellulose I_a and I_b in wood by carbon-13 NMR spectroscopy. Holzforschung. 53:335-340

Newman, R.H. (2004) Homogeneity in cellulose crystallinity between samples of *Pinus radiata* wood. Holzforschung. 58:91-96

Newman, R.H., Davidson, T.C. (2004) Molecular conformations at the cellulose-water interface. Cellulose. 11:23-32

Newman, R.H., Hemmingson, J.A. (1994) Carbon-13 NMR distinction between categories of molecular order and disorder in cellulose. Cellulose. 2:95-110

Newman, R.H., Hemmingson, J.A. (1998) Interactions between locust bean gum and cellulose characterized by ^{13}C n.m.r. spectroscopy. Carbohydrate Polymers. 36:167-172

Newman, R.H., Hemmingson, J.A., Suckling, I.D. (1993) Carbon-13 nuclear magnetic resonance studies of kraft pulping. Holzforschung. 47:234-238

Nishiyama, Y., Langan, P., Chanzy, H. (2002) Crystal structure and hydrogen-bonding system in cellulose Ib from synchrotron x-ray and neutron fiber diffraction. Journal of the Amercian Chemical Society. 127:9074-9082

Nishiyama, Y., Sugiyama, J., Chanzy, H., Langan, P. (2003) Crystal structure and hydrogen bonding system in cellulose Ia from synchrotron X-ray and neutron fiber diffraction. Journal of the Amercian Chemical Society. 125:14300-14306

Nomura, T., Yamada, T. (1972) Structural observation on wood and bamboo by X-ray. Wood Research. 52:1-12

Page, D.H. (1976) A note on the cell-wall structure of softwood tracheids. Wood Fiber. 7:246-248

Ralph, J. (1997) Solution state NMR of lignins. TAPPI Proceedings, ACS meeting. Eds. Argyropoulos, Rials. Cancun. ACS. pp. 55-108

Ralph, J., Ralph, S., Landucci, L. (2004) NMR database of lignin and cell wall model compounds. http://www.ars.usda.gov/Services/docs.htm?docid=10491

Ruel, K., Barnoud, F., Goring, D.A.I. (1978) Lamellation in the S2 layer of softwood tracheids as demostrated by scanning transmission electron microscopy. Wood Science and Technology. 12:287-291

Shen, T., Gnanakaran, S. (2008) The stability of cellulose: A statistucal perspective from a coarse-grained model of hydrogen-bond networks. Biophysical Journal. 96:3032-3040

Smith, M.B., March, J. March's advanced organic chemistry - Reactions, mechanisms, and structure. John Wiley & Sons, Inc., 5th Edition, 2083, 2001

Spiller, D. (1948) Effect of heat treatment on equilibrium moisture content of three New Zealand-grown woods. New Zealand Journal of Science and Technology. 30B:24-26

Sugiyama, J., Vuong, R., Chanzy, H. (1991) Electron diffraction study on the two crystalline phases occurring in native cellulose from an algal cell wall. Macromolecules. 24:4168-4175

Tiemann, H.D. (1906) Effect of moisture upon the strength and stiffness of wood. Agricultural and Forest Service Bulletin. 70:82-84

Vanholme, R., Morreel, K., Ralph, J., Boerjan, W. (2008) Lignin engineering. Current opinion in plant biology. 11:278-285

Vietor, R.J., Newman, R.H., Ha, M.A., Apperley, D.C., Jarvis, M.C. (2002) Conformational features of crystal-surface cellulose from higher plants. The Plant Journal. 30(6):721-731

Weatherwax, R.C. (1974) Transient pore structure of cellulosic materials. Journal of Colloid and Interface Science. 49:40-47

2 Synchrotron WAXS studies of *Pinus radiata* wood nanostructure

2.1 Introduction

The effect of wood drying on the nano-scale cellulose crystals that exist at the core of the cell wall microfibrils has been previously investigated using synchrotron source X-rays. Many of these studies have focused on the use of small-angle X-ray scattering (SAXS) to examine structures at the nanometre-scale in cell walls. This gave information regarding the size of the pores and cavities in cell walls, along with data to describe the distances between cellulose fibrils (Jakob et al. 1996; Suzuki and Kamiyama 2004). More recently, a WAXS study of the effects of moisture adsorption into and desorption from cell walls showed that reversible changes to the cellulose crystal lattice could also occur due to change in water content alone at ambient temperatures (Sugino et al. 2007). Coupling of hydroxyl groups exposed on crystallite surfaces was likely to have changed the conformation of the surface cellulose chains thereby changing the nature of its packing in the crystallite and causing a measurable change in the WAXS diffractogram.

This chapter presents an investigation of molecular changes to the hydration state of the cellulose microfibrils during the drying process and the reversibility of these changes during moisture resorption.

2.2 X-ray diffraction

Matching the wavelengths of electromagnetic radiation to the scale of atoms or molecules under investigation is the fundamental principle of spectroscopic techniques. For atomic dimensions (angstroms), X-rays are required, with wavelengths ranging from 10 nm (100 Å) to 0.01 nm (0.1 Å). A standard X-ray source consists of a vacuum tube with a high voltage applied to accelerate electrons that are produced by a heated cathode. These electrons impact a metal anode and produce X-rays. The wavelength of the resulting X-rays is dependent on the metal anode used, and is a result of X-ray fluorescence, the ejection of an inner shell electron followed by an outer shell electron occupying the vacancy. This method of generating X-rays is limited by the amount of energy that can be applied to the vacuum tube and the amount of resulting waste heat that can be dispersed.

When a diffraction experiment is carried out in reflection mode using a water-wet specimen, the depth of penetration of the beam is limited, due to absorption by water. The reflected beam then comes from a thin layer offset from the centre of the specimen so the diffractogram peak appears relatively narrow and displaced. This problem can be overcome by using transmission mode, but conventional X-ray sources lack the brilliance needed to produce a WAXS diffractogram from a wet specimen. Even without the presence of water conventional X-ray sources lack resolving power, making analysis of diffractograms of wood cellulose difficult (Leppanen et al. 2009). The solution to this limitation is to use a synchrotron X-ray beam.

A synchrotron generates X-rays by accelerating electrons (produced from a cathode source) using a linear accelerator RF field (Linac) and then further accelerated using a further RF field in a booster ring. These high-energy electrons are then injected into a storage ring for experimental use with RF fields used to replace some energy loss during magnetic bending. X-rays are then produced by the use of an insertion device known as an undulator that is made up to a series of dipole magnets. These cause the electrons to oscillate, and by using an appropriate frequency of oscillation, achieved by adjusting the period of the dipole magnets, energy is released in the form of very bright, very narrow band (*i.e.* well-defined wavelength) X-rays (Bilderback et al. 2005).

X-ray scattering

X-rays scattered from crystal planes can be considered in terms of reflections from differing crystal planes (Figure 2.1). These X-rays are considered elastic, meaning they have the same wavelength before and after scattering. A set of parallel X-rays hitting the crystal will have some X-rays being reflected from the surface crystal layer with an angle θ, and some penetrating further to reflect of the n^{th} crystal plane, again with an angle θ. X-rays reflected from a single layer will be in phase, but only under certain conditions will reflection from all planes be in phase and act constructively to produce a detectable signal; this is known as a Bragg reflection. This condition occurs when the extra distance travelled by an X-ray reflected from the n^{th} crystal plane is an integer of the wavelength (λ), i.e. nλ. The extra distance travelled by the reflections of the second crystal layer can be shown to be twice dsinθ (2dsinθ) to remain in phase.

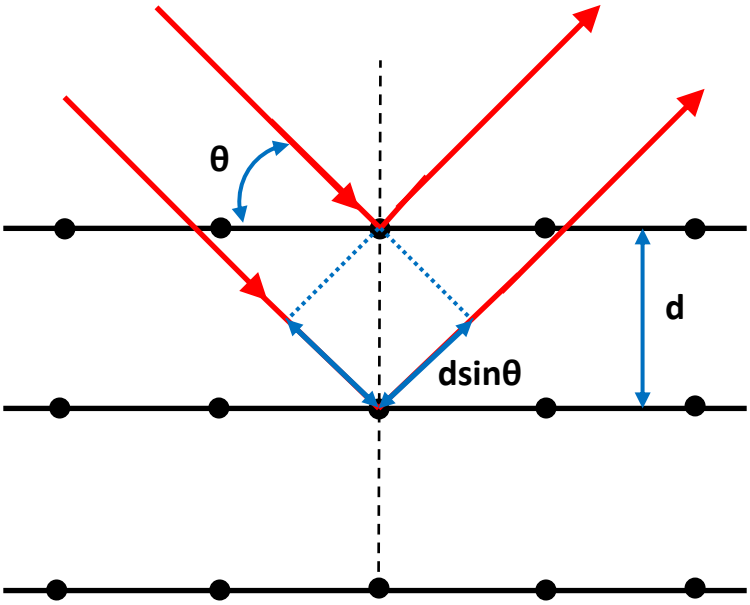

Figure 2.1 *Origin of Bragg reflections.*

The more general form of this is the Bragg equation (Equation 2.1). Rearrangement of this equation shows us that the minimum distance (d) which can measured is λ/2, when sinθ is equal to 1. The consequence of this is that the smaller the wavelength (higher energy the X-rays), the finer the structures that can be observed.

$$n\lambda = 2d\sin\theta \qquad 2.1$$

Wide Angle X-ray Scattering (WAXS)

Wide angle scattering is defined as X-rays scattered at angles greater than *ca.* 5°. From the Bragg equation (2.1) it can be shown that the larger the scattering angle the smaller the d-spacing, and hence the smaller is the periodic structure being probed. These wide-angle diffraction patterns are obtained by placing the detector at a further distance from the source of the scattering.

Using the Scherrer equation (Equation 2.2), the average size of a cubic crystalline domain (L) can be determined from scattering angles, where β is the width at half peak height, λ is the X-ray wavelength, and K is a constant taken to be 0.93 ($2[\text{Ln } 2/\pi]^{1/2}$) (Murdock 1930).

$$L_{hkl} = K\lambda / \beta_{hkl}\cos\theta_{hkl} \qquad 2.2$$

In this equation *hkl* define the relevant crystal plane.

The value of K is not a true constant in that it depends on those crystal planes and the cross-sectional shape (Murdock 1930). In other words it should be expressed as K_{hkl}. Values are available for simple systems, such as cubic crystals (Murdock 1930), but not for polymer crystals such as cellulose. The length values calculated for cellulose using Equation 2.2 are therefore approximate values based on K = 0.93 for all *h,k, and l*.

Australian Synchrotron

The Australian Synchrotron is a 3rd generation synchrotron with nominal lattice energy of 3 GeV and an operating current of 200 mA (*ca.* 24-hour lifetime). The synchrotron has a circumference of 216 m with 12 straight sections for insertion devices (wigglers for a broad spectrum or undulators for a narrow spectrum). Available wavelengths range from infrared to hard X-rays (Australian_Synchrotron 2009).

2.3 Preparation of specimens for X-Ray diffraction

Algal cellulose preparation

A specimen of algal cellulose was prepared for a validation experiment for cellulose peak positions in a diffractogram. Algal cellulose from *Chaetomorpha coliformis* (Figure 2.2) was chosen as it has been found to have large crystal dimensions giving rise to sharp diffraction peaks and proportions of cellulose Iα (57%) and Iβ (43%), similar to that of *Pinus radiata* (51% and 49% respectively) (Davidson et al. 2004).

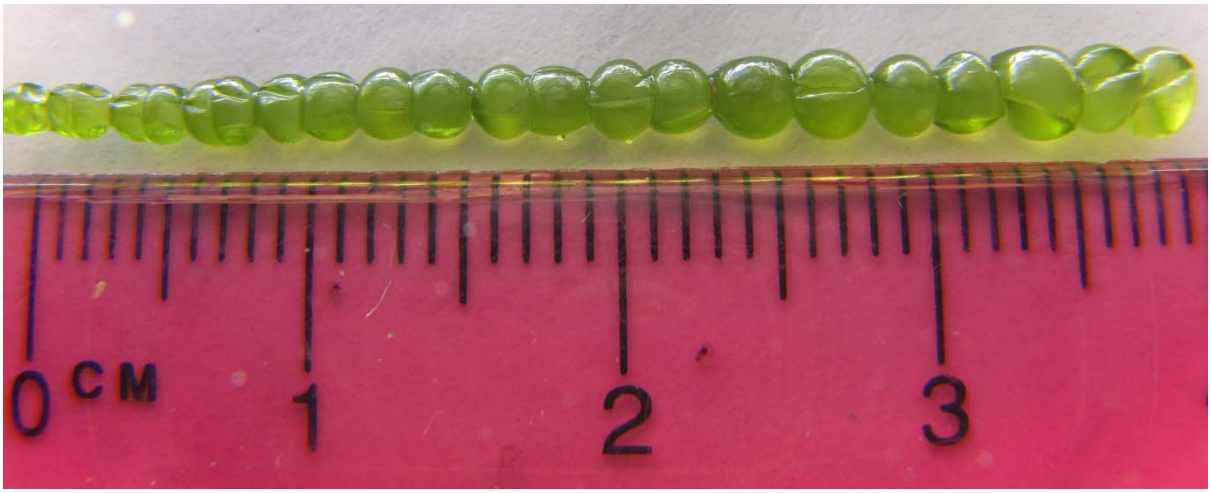

Figure 2.2 *Representative specimen of C. coliformis (each "bubble" is an individual cell).*

Specimens of *C. coliformis* were collected from the Wairarapa coast (New Zealand, 41° S 176° E) by Dr Roger Newman. The cells were mechanically burst and their contents washed out with water followed by preservation in methylated spirits.

Algal paper was prepared according to literature (Clair et al. 2006). Specimens of *C. coliformis* preserved in methylated spirits were washed with distilled water then pressed to remove excess moisture. Approximately 23 g of material was then added to a 500 mL round bottom flask. To this 100 mL of 0.1M NaOH was added, and the mixture was heated under reflux for 3 h. The mixture was then cooled, and then decanted and the solid material was washed with distilled water. To the solid material was then added 200 mL of 0.05M HCl, and the mixture allowed to stand overnight. The resulting white mass was then washed with distilled water and then pressed between two flat aluminium plates. A weight (*ca.* 2 kg) was placed on top of the plates and then left overnight. The top plate was then removed and the white algal paper preparation was allowed to air-dry.

Pinus radiata wood specimen preparation

Specimens of *Pinus radiata* wood were collected as described in the general sampling procedure detailed in Appendix A. A summary is shown in Table 2.1.

Specimens were prepared of never-dried latewood (specimens **1a**, **2**), air-dried latewood (specimen **3**) and oven-dried (105 °C) latewood (specimen **4**). Four times oven-dried (105 °C) latewood (specimen **5**) specimens were prepared by repeating three cycles of oven drying followed by a 24-hour soak in distilled water, ending with a final oven-drying step at 105 °C.

Other specimens prepared were never-dried earlywood (specimen **C1**), never-dried latewood boiled in water and cooled (specimens **C2**, **C3**, **C4** & **C5**), and never-dried latewood soaked in glycerol as a moisture preservative (specimen **C6**). Results for these specimens are discussed fully in Appendix C (C.4, C.6, and C.7 respectively).

All never-dried specimens were stored in distilled water. These specimens were wrapped in wet cotton fabric and placed in sealed plastic bags also containing a small volume of distilled water for transport from New Zealand to the Australian Synchrotron. All dried specimens were dried in an air-conditioned room (20-23 °C / 42-46% RH), for no less than 168 hours and until constant air-dried weights were obtained. All oven-dried specimens were dried at 105 °C until a constant weight was achieved.

A summary of the specimens used in this study is given as Table 2.1.

Table 2.1 *Summary of wood specimens and moisture contents used in the x-ray study (latewood unless specified).*

Specimen	*Moisture content (%)*	*Specimen treatment*
1a	126	Never dried
1b	58	Specimen 1 partly dried at RT
1c	13	Specimen 1 further dried at RT
2	111	Never dried
3	9	Dried at RT
3a	--[a]	Specimen 3 rewet
4	9	Dried at 105 °C & exposed to air
4a	--[a]	Specimen 4 rewet
5	8	Dried 4 times at 105 °C, exposed to air[b]
5a	--[a]	Specimen 5 rewet
C1	--[c]	Never-dried earlywood
C2	--[c]	Boiled in water
C3	--[c]	Boiled in water, quench cooled
C4	--[c]	Boiled in water, slow cooled
C5	--[c]	Glycerol preserved

[a] not measured. [b] rewet 24 h between drying steps. [c] see Appendix C. RT = room temperature.

Preparations prior to synchrotron WAXS analysis on the Australian Synchrotron

For the X-ray diffraction experiments, specimens were encased in Kapton® (4,4'-oxydiphenylene-pyromellitimide) self-adhesive tape (Tesa® 51408 from Beiersdorf AG, Hamburg) immediately prior to mounting for WAXS to minimise moisture loss or gain by diffusion through the tape (Figure 2.3).

Figure 2.3 *Two wood specimens encapsulated in Tesa® 51408 self-adhesive Kapton® tape.*

The manufacturer's data sheet for the tape specified Kapton® (35 μm thick) with a silicone adhesive backing (25 μm thick). Kapton® is routinely used in X-ray techniques for windows due to its high X-ray transmittance, low background signal, and resistance to degradation (Suzuki et al. 1998). The presence of a silicone adhesive coating on the Tesa® 51408 Kapton® tape made encapsulation easy and quick providing an immediate barrier to loss or gain of moisture. The tape is designed to withstand high

temperatures (180 °C continuous or up to 350 °C for 10 hours) without losing adhesiveness making it ideal for synchrotron X-ray use (Tesa_SE 2010). See Appendix B for tests on Tesa® 51408 tape as encapsulation material.

Kapton® tape encasement was used on all specimens including those dried that were to be analysed. A pair of encased specimens were then affixed by Scotch™ tape to the WAXS specimen holders aluminium arms such that the encased specimens were roughly centred (a "U" shaped holder, Figure 2.4). This holder was then placed as close as possible at the front of the X-ray beam exit aperture.

An X-ray beam energy of 13 keV was used, giving an X-ray wavelength of 0.9537 Å. A Mar-CCD detector (1,024 x 1,024 pixels) was located 250 mm from the specimen allowing detection of 2θ angles out to approximately 30° to be achieved. The beam size was 0.2 mm by 0.1 mm, and the detector pixel size was 0.158 mm^2. The exposure time was 1 s using an automated rastered 5 x 5 grid spaced 1 mm apart to obtain 25 diffraction patterns per specimen. The diffractograms presented in this chapter are the average of 25 data sets obtained per specimen (Appendix C.1).

Once the first specimen of the pair on the holder was completed, the second specimen was moved into position under computer control and the rastering process repeated. After this, another pair of specimens were affixed to the holder and the process was repeated for all specimens. A further never-dried specimen was subjected to 100 one-second exposures to the X-ray beam, recording each diffractogram to check for radiation-induced damage (Appendix C.2).

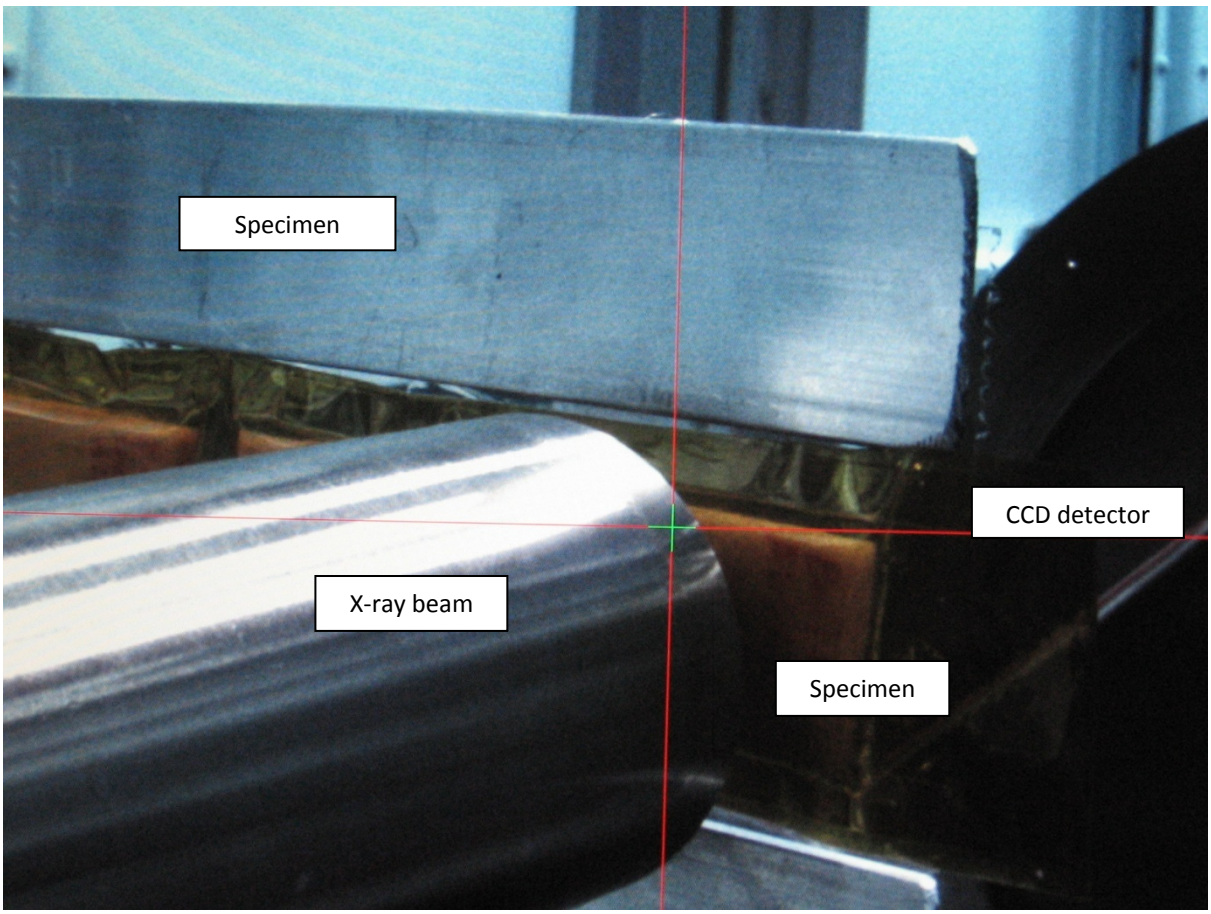

Figure 2.4 *Specimen setup for scattering experiments perpendicular to the direction of the grain (cellulose crystals).*

2.4 Results from WAXS diffraction studies

Check of WAXS diffraction calibration

A specimen of silicon powder encased in Kapton® was used to check the calibration of the WAXS detector. A single major diffraction peak was identified at a 2θ of 17.4734° translating to a *d*-spacing of 3.139 Å (Figure 2.5). This agrees well with the published data for the silicon powder *d*(111) peak at 3.136 Å (Hubbard et al. 1975).

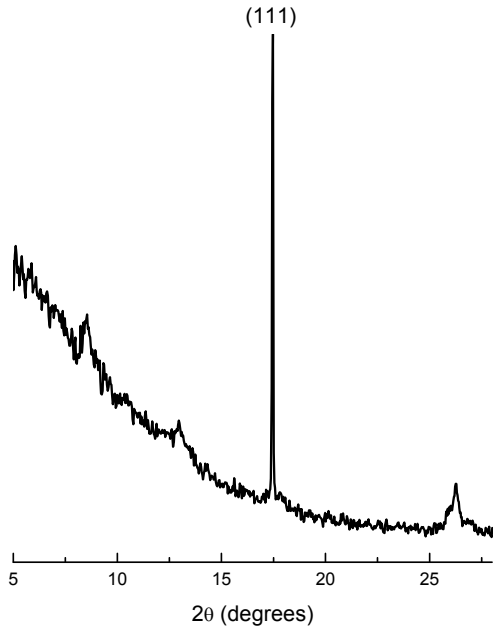

Figure 2.5 *Diffractogram of Si powder encased in Kapton®.*

Diffraction pattern for water

At moisture contents above fibre saturation point, liquid-like water can have a significant contribution to the resulting diffractogram. Water alone produces a WAXS diffractogram, with the major peak having a *d*-spacing of ca. 0.314 nm and shoulder peak with a *d*-spacing of *ca.* 0.229 nm (Hura et al. 2003) that complicates the interpretation of diffractograms of never-dried wood specimens. To better account for this interference, the WAXS diffractogram of water encased in Kapton® tape was determined. The resulting diffractogram is presented in Figure 2.6. The diffractogram of water showed two broad peaks centred at 2θ values of approximately 17.5° and 25°, with calculated *d*-spacings of 0.318 nm and 0.224 nm respectively, agreeing closely with the literature values of Hura et al.

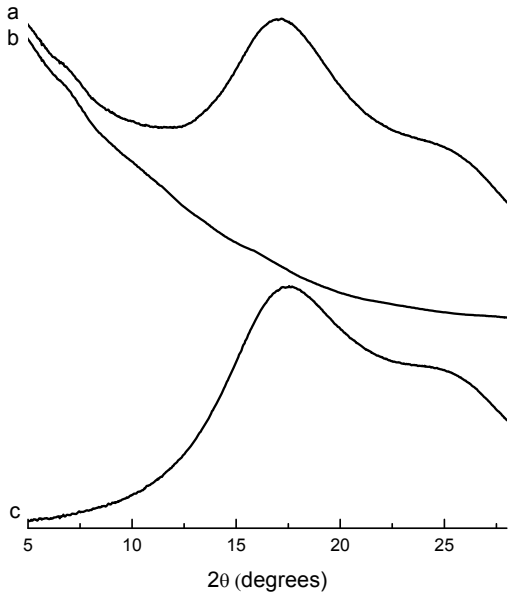

Figure 2.6 *WAXS diffractograms of (a) water encased in Kapton®, (b) Kapton® alone and (c) the difference between (a) & (b).*

Simulation of cellulose Iα and Iβ diffractograms using CCDC Mercury 2.2

The following assumptions are used in the diffraction pattern simulation (CCDC 2010):

- The Lorentz-polarisation correction assumes a laboratory X-ray source. No absorption is simulated. Fixed slit widths are assumed. No background is included.
- All non-hydrogen atoms are assumed to have isotropic atomic displacement parameters (U_{iso}) of 0.05 Å^2. Hydrogen atoms for which 3-D coordinates are available are taken into account and assigned U_{iso} values of 0.06 Å^2.
- The powder pattern simulator considers site occupation factors.
- All reflections have a symmetric pseudo-Voight peak shape with a full width half maximum of 0.1 degree 2θ.
- The (0, 0, 0) reflection is excluded.

Simulated powder diffraction patterns obtained for cellulose Iα and Iβ showed the major reflections along the crystal planes from which they originate, are shown in Figures 2.7 and 2.8 respectively. Comparing literature d-spacings for the major peaks of cellulose Iα and Iβ, it was found that the (100) peak of Iα overlapped with the $(1\bar{1}0)$ peak of Iβ, the (010) peak of Iα overlapped with the (110) peak of Iβ, and the (110) peak of Iα peak overlapped with the (200) peak of Iβ (Sugiyama et al. 1991). This simulation showed that no differentiation would be made between cellulose Iα and Iβ in the following discussions of experimental WAXS data. Due to this diffraction overlap, and the main differences between cellulose Iα and Iβ being in the fibre repeat direction, this study will

describe reflections in terms of the $(1\bar{1}0)$, (110) and (200) reflections of cellulose Iβ only (Figure 2.9). Specifically these peaks are chosen as unlike the simulations that assume a three-dimensional crystal array, the cellulose found in algae and wood have two-dimensional packing.

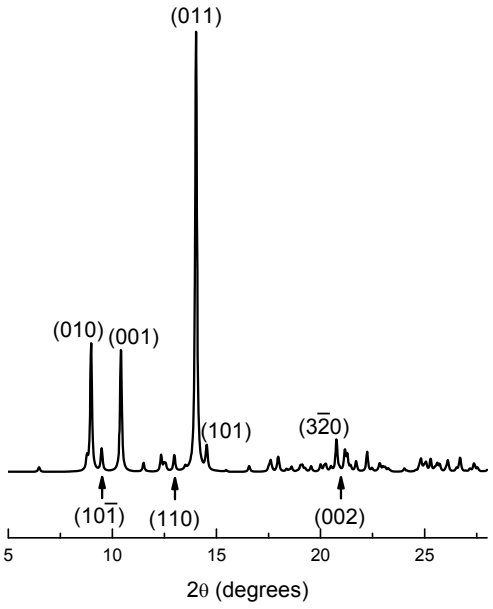

Figure 2.7 *Simulated WAXS pattern for cellulose Iα using an X-ray wavelength of 0.9537 Å and applying a 2θ broadening factor of 0.1.*

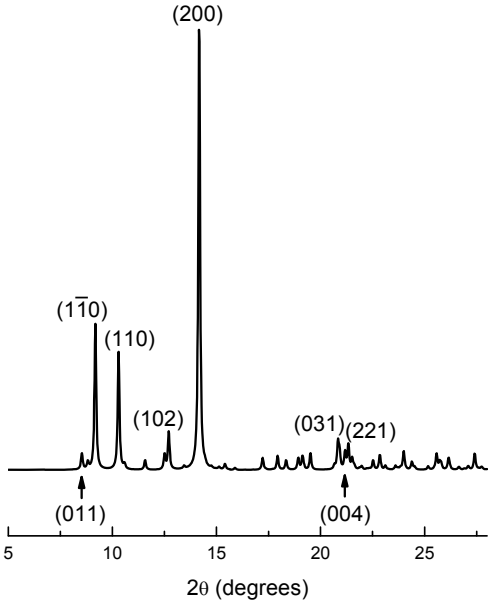

Figure 2.8 *Simulated WAXS pattern for cellulose Iβ using an X-ray wavelength of 0.9537 Å and applying a 2θ broadening factor of 0.1.*

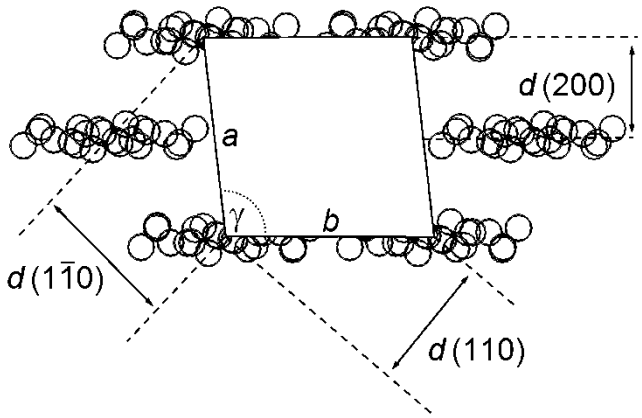

Figure 2.9 *Cellulose chains arranged on a monoclinic (cellulose Iβ) lattice and projected along the fibre axis. Circles indicate carbon and oxygen atoms, centre cellulose chain omitted for clarity.*

Synchrotron analysis of algal (C. coliformis) paper

The X-ray diffractogram of *C. coliformis* shows sharp peaks due to the large cellulose crystal size assigned as for cellulose Iβ (Figure 2.10). This large crystal size is indicated by the high proportion of interior cellulose chains (0.852) (Davidson et al. 2004). The positions of the peaks agree strongly with the simulated diffraction patterns of cellulose Iα and Iβ given above (Figures 2.7 and 2.8), indicating that cellulose Iα and Iβ are indeed indistinguishable in the diffractogram obtained. If the WAXS peaks for cellulose Iα and Iβ forms are not distinguished by diffraction when using a model algal system, then it is concluded there would be no possibility of distinguishing the cellulose forms in wood, as wood has smaller cellulose crystals which results in diffraction peak broadening.

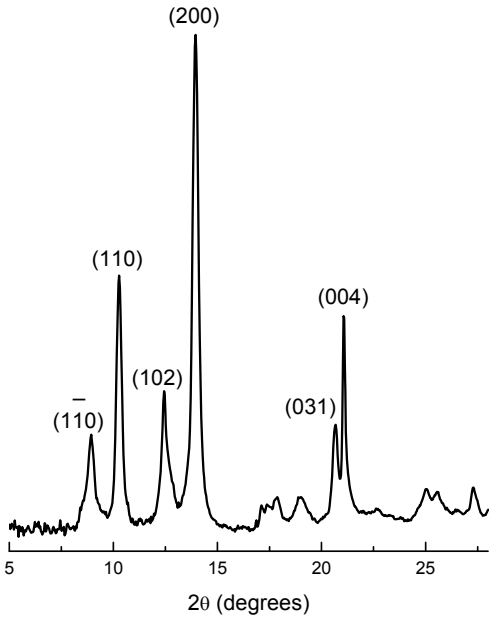

Figure 2.10 *X-ray diffractogram of algal (C. coliformis) paper (peaks labelled for cellulose Iβ as in Figure 2.8).*

By measuring the centroid of the above peaks, and using labelling for cellulose Iβ the following d-spacings were obtained: $d(1\bar{1}0)$ 6.12 Å, d(110) 5.33 Å, d(200) 3.93 Å, and d(004) 2.61 Å. These values compare well with those previous reported of 6.12 Å, 5.36 Å, 3.96 Å, and 2.59 Å respectively (Sugiyama et al. 1991). This result confirms not only the reliability of the results obtained from the synchrotron, but also acts as a template to identify peaks in the specimens of wood. However, wood cellulose crystals are highly aligned in the direction of the microfibril angle, and as previously discussed in the case of latewood, this microfibril angle is low and is aligned in the direction of the wood grain. This means the major diffraction peaks from wood cellulose are from equatorial reflections, *i.e.* those with hk0.

2.5 Synchrotron WAXS data analysis

Data processing for Pinus radiata specimens

The CCD camera detector captures an image of the diffraction pattern and this is stored as a Tagged Image File Format "tiff" format graphic (Figure 2.11).

Analysis of diffraction patterns was carried out by specialised image analysis software (provided by the Australian Synchrotron). The software uses ITT Visual Information Solutions (VIS) IDL Virtual Machine

(http://www.ittvis.com/ProductServices/IDL/VirtualMachine.aspx) to run software written by David J. Cookson of the Australian Synchrotron (SAX15ID v3.296).

Processing of the diffraction images consists firstly of masking off areas that will not be included in the image analysis. These regions include the beam stop and beam stop support. The software then converts the image to a plot of pixel intensity as a function of the distance (angle) from the beam origin (the middle of the beam stop). This plot can be expressed in term of intensity as it relates to CCD pixel location, scattering angle (2θ), Q ($Å^{-1}$) or *d*-spacing (Å). In this thesis results will be presented in terms of scattering angles (2θ) and *d*-spacings (Å).

Diffraction traces were extracted from diffraction patterns using a 10° cake slice orthogonal to the grain direction (Figure 2.11) and from this a 10° cake slice centred on 60° from the grain direction (Figure 2.11) was subtracted to minimise contributions from crystalline cellulose. Taking a "cake slice" involves averaging signal intensities over all pixels within a given arc. This subtraction removes the background from the Kapton® tape and the diffuse halo of reflections of non-cellulose origin such as hemicelluloses and water. A specimen of distilled water encased in Kapton® was used to acquire a diffractogram for water alone. A 10° cake slice parallel with the grain direction (Figure 2.11, specimen **1a**) was used to determine the (002) peak position (fibre repeat direction). The advantage of using a cake slice subtraction step is an increased signal to noise ratio by isolating only the reflections of interest (Figure 2.12, specimen **1a**) due to not averaging signal over the entire diffractogram. It was noted that a (004) reflection appeared in to orthogonal cake slice with an intensity stronger than predicted from the simulation (Figure 2.8 and Figure 2.12, specimen **1a**). The origin of the (004) peak in this diffractogram is from cellulose in the ray cells which run *ca.* 90° to fibre cells of xylem. The intensity of this (004) peak in the 90° cake slice is determined by the number of ray cells present in the specimen, and as such it is of little relevance to the present study.

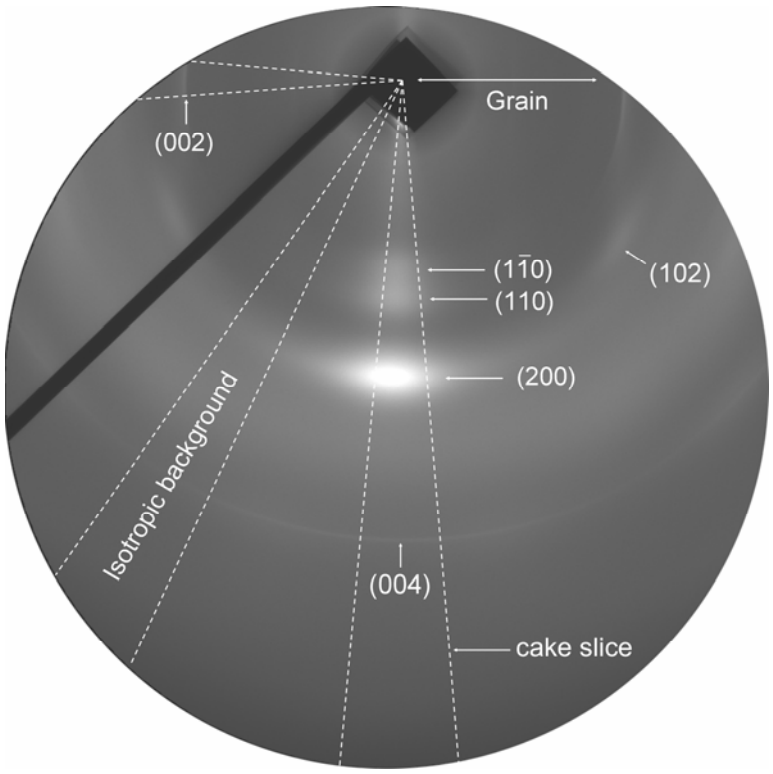

Figure 2.11 *Example WAXS diffraction pattern obtained. Labelled "spots" are diffraction planes. The dashed line represents an example of a "cake slice" (specimen **1a**, see below for details).*

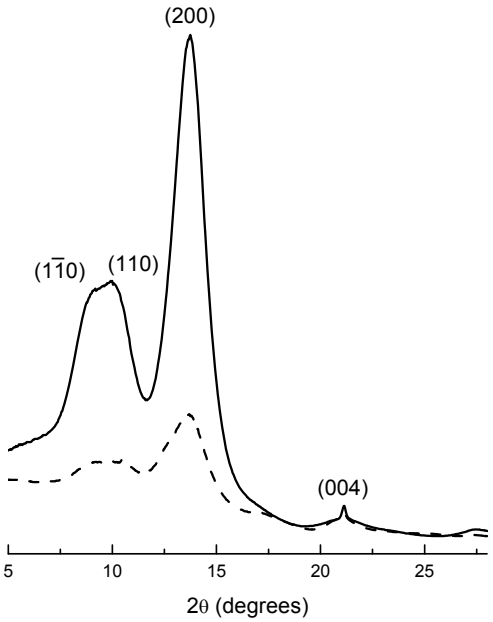

Figure 2.12 *Diffraction plot showing differences between processing the entire image (dashed line) or only a 10° "cake slice" (specimen **1a**, solid line).*

Modelling diffractogram peak shapes for wood

A Lorentzian (Cauchy) curve fit was used to approximate peak positions of the ($1\bar{1}0$), (110) and (200) peaks (Equation 2.3 & 2.4).

$$\Delta = (2\theta - 2\theta_{hkl}) / 2\theta_{width} \qquad 2.3$$

$$I = h / (1 + \Delta^2) \qquad 2.4$$

Where Δ is the distance from the peak maximum position ($2\theta_{hkl}$) normalised by the scaling parameter ($2\theta_{width}$) and h is used to scale the intensity.

A Lorentzian function has been shown to most closely approximate the diffractogram shape seen in cellulose (Gjonnes et al. 1958). Although the (200) peak is clear and distinct, the ($1\bar{1}0$) and (110) peaks have considerable overlap in wood. These three peaks were modelled using the following Lorentzian function.

The peaks for the ($1\bar{1}0$) and (110) reflections were fitted separately from the (200) to simplify the fitting process.

Comparing modelled diffractograms with experimental data

Figures 2.13 and 2.14 show examples for the ($1\bar{1}0$) and (110) diffractogram peaks of never-dried (specimen **1a**) and 4x oven-dried (specimen **5**) latewood diffractograms respectively.

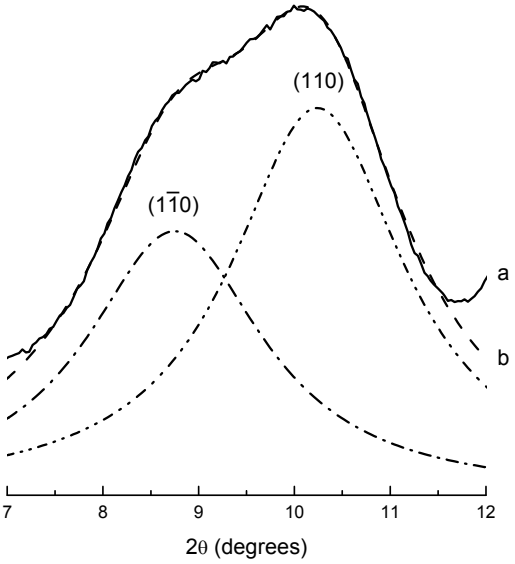

Figure 2.13 *Lorentzian model fit of the ($1\bar{1}0$) and (110) peaks of never-dried wood (specimen **1a**, a = experimental data, b = model total fit, dashed lines = individual fit components).*

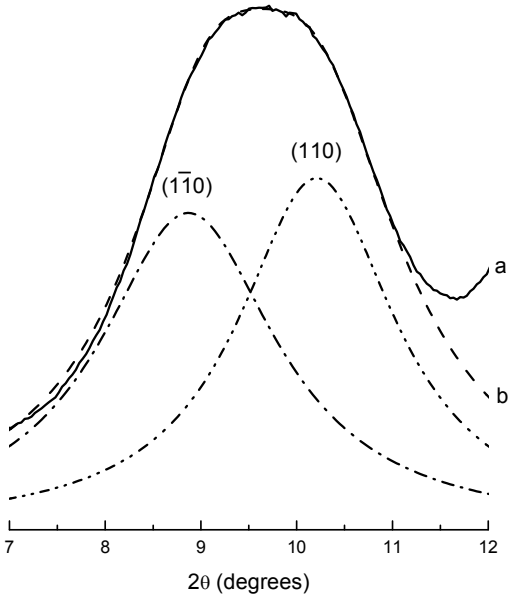

Figure 2.14 *Lorentzian model fit of the (1$\bar{1}$0) and (110) peaks of 4x oven-dried wood (specimen **5**, a = experimental data, b = model total fit, dashed lines = individual fit components).*

2.6 Drying experiments with *Pinus radiata* specimens

Drying to fibre saturation point and below fibre saturation point

A specimen of never-dried latewood initially at a moisture content of 126% (specimen **1a**) was then partially dried to a moisture content of 58% (specimen **1b**). Two similar diffractograms (Figure 2.15) were obtained for the starting material and the partially-dried product. The major difference was seen at 2θ values of approximately 17.5° and 25° as broad shoulder peaks (Figure 2.15a and 2.15b). Figure 2.15c shows the diffractogram obtained from an air-dried specimen, which show a partial collapse of the (1$\bar{1}$0) and (110) peaks, a slight shift in the position of the (200) peak, but no change to the (004) peak. This difference between the never-dried and partly dried specimens was attributed to the loss of liquid-like water from the wood cells, presumably mostly from the cell lumens. This can be seen when the diffractogram for wood at 58% MC was subtracted from that of never-dried wood at 126% (Figure 2.15d).

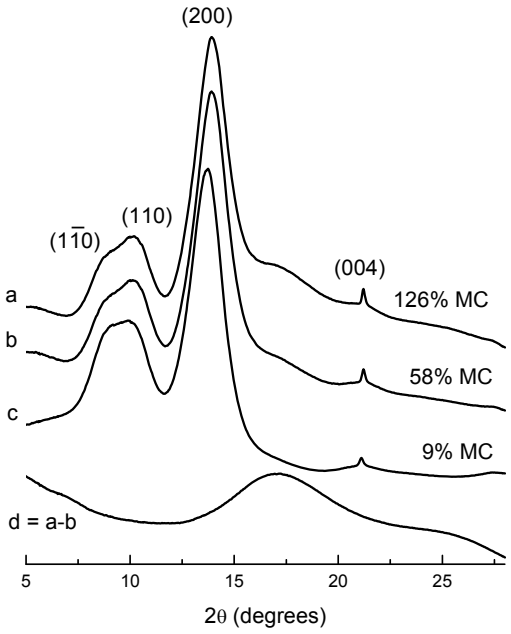

Figure 2.15 *WAXS diffractograms (90° to grain cake slice) of Pinus radiata latewood (a) never-dried (specimen **1a**), (b) after being partly air-dried (specimen **1b**), (c) air-dried (specimen **3**) and (d) never-dried minus partly-dried (a-b).*

The loss of diffraction from liquid water as the only observable change in the diffractogram can be demonstrated by comparing Figure 2.15d to the diffractogram of water alone encapsulated in Kapton® (Figure 2.6). The broad peak seen in the diffractogram of wood has been interpreted due to diffraction from the non-crystalline components (e.g. hemicellulose and liquid water) (Sugino et al. 2007). However, from work presented in this thesis the broad band can be attributed to water alone.

Previous investigations have also showed that wood that had been exhaustively dried and then rewetted showed no water peak at moisture contents less than fibre saturation point (Nishimura et al. 1981). However, in never-dried wood or wood not dried to less than the fibre saturation point, the presence of an underlying water peak can make comparisons with diffractograms of fully dried wood difficult due to distortion of the (200) peak.

Subtraction of diffractograms 60° to the grain from those 90° to the grain effectively removes the diffractogram "halo" of non-ordered components, including those from Kapton®, hemicelluloses and water, thereby leaving a diffractogram of only the cellulose independent of moisture content (Figure 2.16a and 2.16b). Even at well below fibre saturation point (specimen dried to 9% moisture content, specimen **3**) there still appeared to be a contribution to the diffractogram from liquid-like water (Figure 2.16a and 2.16c).

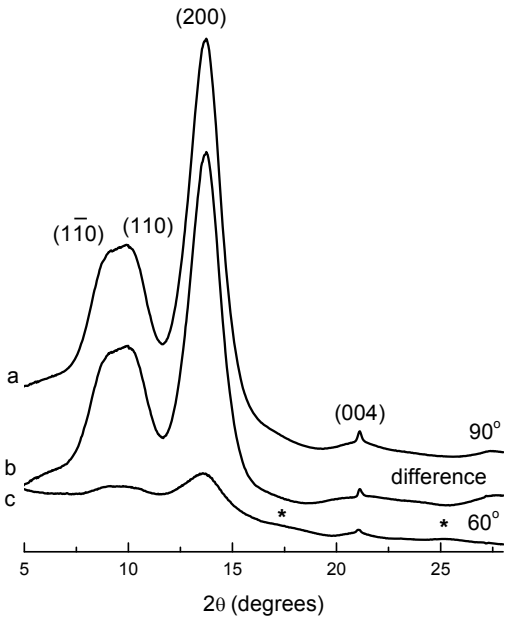

Figure 2.16 *WAXS diffractograms of air-dried (specimen **3**) Pinus radiata latewood (a) 90° to grain, (b) 90° minus 60° to grain (a-c) and (c) 60° to grain showing non-ordered components [Asterisks indicate contributions from liquid-like water].*

The process of drying wood species to below fibre saturation point had no significant effect on the peak shape of the (200) peak, implying that there was little change in the cellulose crystal order/disorder. However, a shift in the (200) peak position can be seen as a result of completely drying a specimen in an oven at 105°C (specimen **4**), and then allowing the specimen to passively take up atmospheric moisture to reach an equilibrium moisture content (EMC) of 9% (Figure 2.17). This indicated that the inter-plane crystal dimension (200) increases on drying. This peak shift to lower values of 2θ has been previously observed in wood drying (Abe and Yamamoto 2005; Sugino et al. 2007). The degree of change to the position of the (200) peak was interpreted to be related to the amount of hemicellulose-lignin matrix present with microcrystalline cellulose having a (200) peak position independent of the moisture content (Abe and Yamamoto 2005). These results suggest that as the moisture content at wood cell walls diminishes below the fibre saturation point, the hemicellulose-lignin matrix imposes some degree of physical force directly on the cellulose crystallites, and that the magnitude of this force is related to the moisture content of the matrix.

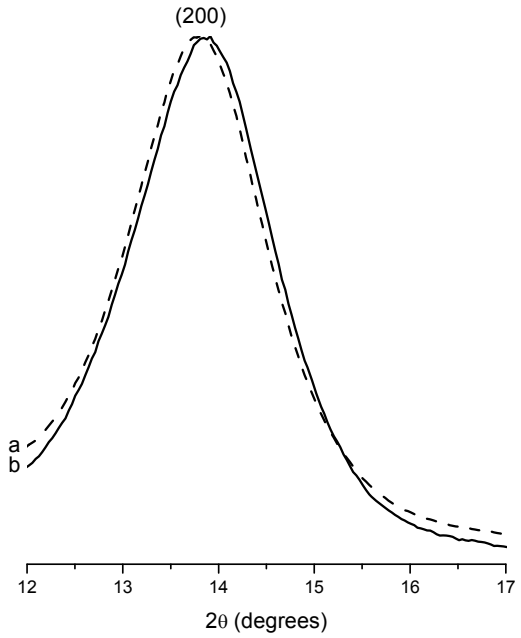

Figure 2.17 *WAXS diffractogram of wood 90° minus 60° to the grain cake slice of the 200 peak for (a) oven-dried (specimen **4**) and (b) never-dried (specimen **1a**) Pinus radiata latewood.*

The diffraction data peaks for air-dried specimens (specimens **1c** and **3**) showed that the reflections for the $(1\bar{1}0)$ and (110) planes had coalesced as the moisture content of the specimen decreased (Figure 2.18a and 2.18b). This effect is observed most prominently in specimens that had been oven-dried (specimen **4**, Figure 2.19a and 2.19b).

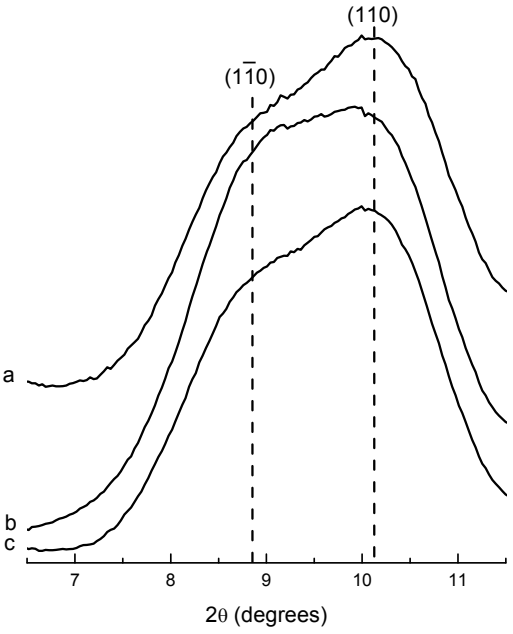

Figure 2.18 *WAXS diffractogram cake slice of 90° minus 60° to grain of (a) never-dried (specimen **1a**), (b) air-dried (specimen **3**) and (c) air-dried and rewetted (specimen **3a**) Pinus radiata latewood.*

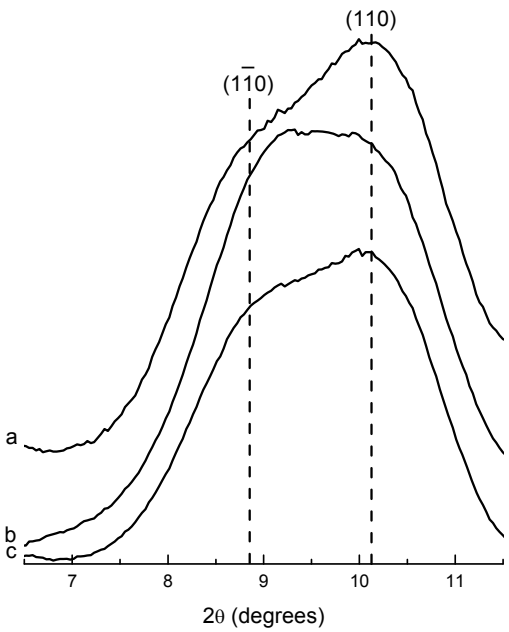

Figure 2.19 *WAXS diffractogram cake slice of 90° minus 60° to grain of (a) never-dried (specimen **1a**), (b) 1x oven-dried (specimen **4**) and (c) 1x oven-dried rewet (specimen **4a**) Pinus radiata latewood.*

The magnitude of the peak position shifts was dependant on the relative degree of harshness of drying.

In light of the observed changes to diffraction from the (1$\bar{1}$ 0) and (110) planes with moisture content changes the interpretation of the diffraction data reported by others in relation to cellulose crystal polymorphism is questioned. A discussion (Appendix D) is presented relating to interpretation of diffraction data of the purported cellulose IV_I crystal polymorph identified in red meranti wood.

Effects of drying and rewetting cycles on Pinus radiata wood

Dry-wet cycling was used to compound irreversible changes associated with oven drying, in order to increase the chances of observing effects on wood nanostructure.

The specimen dried over three oven-dry, three rewet cycles, and a final oven-dry step (specimen **5**) showed the most pronounced collapse of the (1$\bar{1}$ 0) and (110) peaks (Figure 2.20a and 2.20b). Wood material submitted to this extreme treatment was shown to have the shortest inter-chain hydrogen bonding distance (*b*) and the smallest unit cell angle *γ*.

The air-dried (specimen **3**), oven-dried (specimen **4**), and 4x oven-dried (specimen **5**) specimens were then rehydrated and their diffractograms were re-measured and

showed that the process of drying and re-wetting cell walls resulted in a sequence of nano-structural changes which were partially reversible (Figures 2.18c, 2.19c, and 2.20c).

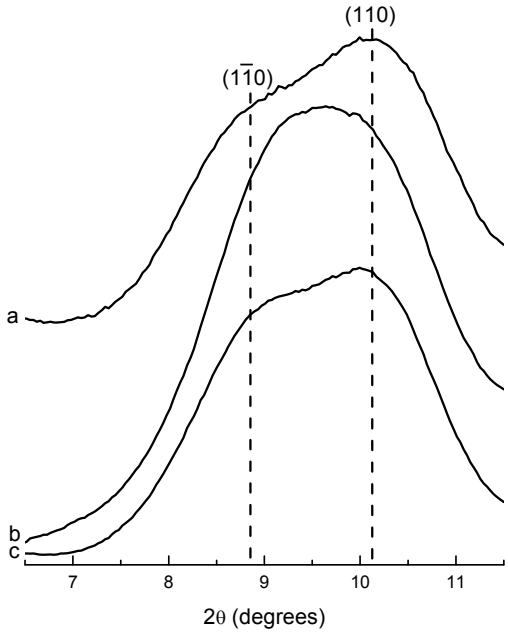

Figure 2.20 *WAXS diffractogram cake slice of 90° minus 60° to grain of (a) never-dried (specimen **1a**), (b) 4x oven-dried (specimen **5**) and (c) 4x oven-dried rewet (specimen **5a**) Pinus radiata latewood.*

By applying the Scherrer equation (Equation 2.2) the dimensions of the crystal can be determined (Table 2.2).

Table 2.2 *Calculated cubic crystal lengths using the Scherrer equation.*

Specimen	*$L_{(1\bar{1}0)}$ (nm)*	*FWHH (1$\bar{1}$0) (degrees)*	*$L_{(110)}$ (nm)*	*FWHH (110) (degrees)*	*$L_{(200)}$ (nm)*	*FWHH (200) (degrees)*	*RMS of total curve fit*
1a	2.28	2.24	2.32	2.20	2.84	1.80	0.003
3	2.43	2.10	2.32	2.20	2.84	1.80	0.003
3a	2.28	2.24	2.36	2.16	2.84	1.80	0.002
4	2.32	2.20	2.22	2.30	2.84	1.80	0.003
4a	2.28	2.24	2.48	2.06	3.01	1.70	0.003
5	2.50	2.04	2.28	2.24	2.84	1.80	0.003
5a	2.28	2.24	2.55	2.00	3.20	1.60	0.002
Average	2.33		2.36		2.92		
Coefficient of Variance	0.04		0.05		0.05		

FWHH = full width at half peak height.

Although the moisture content and moisture history of the specimens differ there is no significant change in the average cellulose crystal domain size. The lack of significant change to the crystal size indicates that during drying cellulose crystal aggregation was not occurring.

If the cross-sectional shape is approximated by a circle then the diameter is equal to the average of the ($1\bar{1}0$), (110) and (200) cross-sectional dimensions i.e. (1/3) x (2.33 + 2.36 + 2.92) = 2.54 nm. A model consistent with this will be discussed below.

Calculation of unit cell parameters for cellulose Iβ

From the observed *d*-spacings and the relationship that the *c* unit cell dimension can be obtained from twice the *d*(002) dimension in the cellulose monoclinic crystal, the apparent unit cell parameters were then calculated. The term 'apparent unit cell parameters' was used, as all parameters were calculated as if the entire crystal structure was in the monoclinic form (i.e. cellulose Iβ only). This was done by solving for *a*, *b*, and *γ* in Equations 2.5a, 2.5b, and 2.5c using the Newton-Raphson method. The equations were rearranged to all be equal to zero, and *d*-spacing parameters were then input into the software package Maxima (v5.19.2, http://maxima.sourceforge.net/) and the unit cell parameters determined. Initial estimates were based on reported unit cell values for cellulose Iβ; *a* = 0.778, *b* = 0.820, and *γ* = 96.5° (Nishiyama et al. 2002).

$$d(1\bar{1}0)^2 = [a^2 * b^2 * \sin(\gamma)] / [a^2 + b^2 + (2ab * \cos(\gamma))] \quad 2.5a$$

$$d(110)^2 = [a^2 * b^2 * \sin(\gamma)] / [a^2 + b^2 - (2ab * \cos(\gamma))] \quad 2.5b$$

$$d(200)^2 = a^2 * \sin^2(\gamma) / 4 \quad 2.5c$$

The resulting calculated cellulose Iβ monoclinic unit cell parameters are presented in Table 2.3. The unit cell is shown in Figure 2.9.

Table 2.3 *Apparent unit cell parameters based on the cellulose Iβ monoclinic crystal*.*

Specimen	*d(1$\bar{1}$0) (nm)***	*d(110) (nm)***	*d(200) (nm)***	*d(002) (nm)***	*a (nm)*	*b (nm)*	*c (nm)*	*γ (°)*
1a	0.625	0.532	0.393	0.517	0.795	0.847	1.034	99.2
1b	0.622	0.531	0.393	0.517	0.795	0.843	1.034	99.1
1c	0.617	0.530	0.394	0.517	0.798	0.831	1.034	98.7
2	0.625	0.534	0.395	0.518	0.799	0.846	1.036	99.0
3	0.621	0.535	0.399	0.518	0.806	0.834	1.036	98.5
3a	0.629	0.536	0.396	0.520	0.802	0.853	1.040	99.2
4	0.609	0.531	0.396	0.517	0.799	0.817	1.034	97.8
4a	0.620	0.534	0.394	0.518	0.796	0.842	1.036	98.6
5	0.603	0.535	0.399	0.518	0.804	0.807	1.036	96.8

5a	0.616	0.535	0.396	0.520	0.800	0.833	1.040	98.0

* = refer to Figure 2.9 for dimension definitions. ** = ±0.002 nm (see Appendix C)

From the average values obtained from the Scherrer equation and the *d*-spacings it then is possible to construct a model cellulose crystal. By dividing the *L* dimension by its respective *d*-spacing we can obtain an estimate of the number of crystal planes in each direction. Figure 2.21 is a representation of a hexagonal shaped 18-chain cellulose crystal based on the *L* and *d*-spacing data obtained in this work.

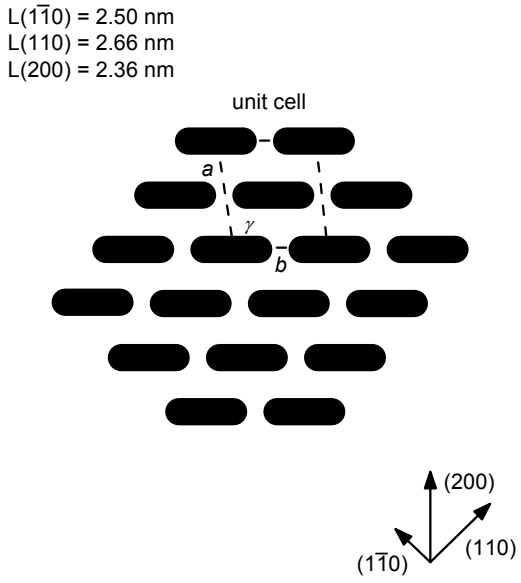

Figure 2.21 *Model "18-chain" cellulose crystallite based on data obtained (refer to Figure 2.9 for details on unit cell and crystal planes).*

An 18-chain model was chosen due to the observation that the protein complex that synthesises the cellulose in woody plants consists of a rosette of six subunits (Saxena and Brown 2005; Somerville 2006). It therefore seems reasonable to assume that the number of cellulose chains in a cellulose microfibril would be a multiple of six. If the multiplicative factor is set at three, and a hexagonal model is constructed as in Figure 2.21 then this shape can be approximated by a circle with a diameter of (1/3) x (0.62 x 4 + 0.53 x 5 + 0.40 x 6) = 2.51 nm. This is consistent with the experiment estimate of 2.54 nm discussed above.

Hydration effect on the unit cell parameters of cellulose Iβ

Changes have been observed in the cellulose unit cell parameters caused by changes in the moisture content of the wood cell wall. In particular, *b* and *γ* show significant variations, Figure 2.22 presents the relationship between the unit cell parameters *b* and

γ (R^2 0.87) according to moisture state. Values for pure cellulose Iα and Iβ (both treated as monoclinic) are given as reference.

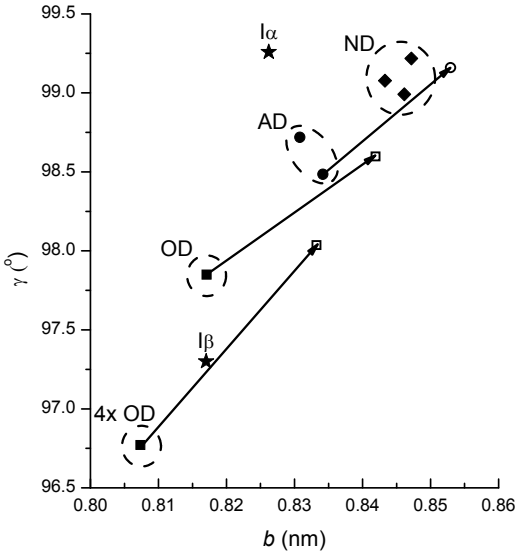

Figure 2.22 *Relationship of changes to the b unit cell dimension and the unit cell angle (γ) as a function of drying method. [ND = never dried, AD = air-dried, OD = oven-dried. Open symbols = rewetted specimens as indicated by the origin of the arrows. Star = cellulose Iα and Iβ (Sugiyama et al. 1991) using a monoclinic unit cell model.]*

Specimens that were never-dried have the longest *b* dimension and the highest angle *γ*. Air-drying of wood caused a reduction in both these values, and oven drying yet a further reduction. The air-dried specimen when rewet returned to dimensions similar to those of never-dried wood. Rewetting the singly oven-dried specimen resulted in only partial recovery to the never-dried parameters, and rewetting the 4x oven-dried specimen showed an even lesser degree of dimensional recovery. The specimen partially air-dried to a moisture content of 58% (i.e. above fibre saturation point) showed little difference from never-dried specimens, thereby indicating the changes to the cellulose crystal structure do not occur until moisture content is lower than the fibre saturation point, taken to be 30%.

The changes in wood during drying and rewetting are seen in both the *b* and *γ* unit cell parameters, whereas the differences between cellulose Iα and Iβ can be seen to be mainly as a change in the monoclinic angle, *γ*, with little change in the distance between the cellulose hydrogen bonded sheets (Figure 2.9). The changes to the unit cell may be a direct effect of the cellulose crystal surfaces becoming dehydrated during drying and on wood specimen rewetting, only becoming partially rehydrated due to

some irreversible association with the cell wall matrix hemicelluloses (Newman and Hemmingson 1998). Alternatively it has been suggested that these unit cell changes are due to the surrounding matrix being swollen when wet and consequently imposing a force on the cellulose crystal. As the matrix dries and shrinks, this force is lessened (Abe and Yamamoto 2005), thereby possibly allowing the cellulose crystals to change conformation. The matrix then swells again after rewetting, once again imposing a force upon the cellulose crystals. The effect of changes to the volume of the matrix may cause an differential response from the cellulose crystal microfibril due to its mechanical anisotropy, since the moduli of elasticity parallel and perpendicular to *c* differ by an order of magnitude (Diddens et al. 2008), and thus may contribute to the observed changes to *b*. However, how this isotropic change to the matrix volume would result in a change the cellulose crystal unit cell angle *γ* is not obvious. A small part of the observed effects of the apparent change to the unit cell could also be due to conversion of cellulose Iα to the more stable cellulose Iβ by annealing during high temperature (oven) drying (Sugiyama et al. 1990). However the conversion from cellulose Iα to Iβ would appear to have a larger effect on the angle γ than on the unit cell dimension *b*. This was not observed with unit cell changes almost equally seen in *γ* and *b* parameters making it unlikely that any conversion from cellulose Iα to Iβ plays an important role even under high temperature drying.

It is known that the cellulose crystals in wood have a high surface area to volume ratio, indicating a small number of cellulose chains per crystal (Newman 1998). Water molecules on the crystal surface may play an important role in determining the conformation of the cellulose crystal. This would imply that changes to the unit cell parameters reflect differing hydration states of the cellulose crystal surfaces.

In the direction of the cellulose chains (*c*-axis) there was little change observed for the diffraction data of all specimens where an average unit cell dimension of 1.036 ± 0.001 nm was found. Changes in the fibre repeat have been observed when wood has been put under tension and is expressed as a Poisson ratio (Peura et al. 2007). The Poisson ratio (*v*) for cellulose can be described as the negative ratio of the changes in the *d*(200) (perpendicular to fibre repeat direction) and *d*(002) (fibre repeat direction) reflections. In cellulose crystals, the Poisson ratio has been found to have a small positive value (Abe and Yamamoto 2005), so any shrinkage in the transverse direction as observed in this study should be accompanied by an extension in the fibre repeat direction. Using values of v of 0.1 to 0.38 (Nakamura et al. 2004; Abe and Yamamoto 2005) we would except that a contraction in the transverse direction (hk0) should equate to an extension in the lateral direction (00l) of 0.06% to 0.24%. An increase in

the fibre repeat distance of *ca.* 0.6% was observed in this study. This is greater than can be accounted for if the effect was Poisson in nature for the decrease seen in the transverse *b* direction on drying of wood specimens.

The conformational and crystal inter/intra-relational changes to the apparent unit cell that occur in wood material during drying exist only perpendicular to the direction of the cellulose crystals. Therefore the observed changes to the unit cell are not a response to drying stresses as is currently understood.

Evidence from this study has highlighted that it is critically important to account for the history of specimens in terms of moisture content from the time the specimen is initially collected until analysis. A green wood specimen conditioned by allowing it to adopt particular moisture content by drying would yield differing diffraction results for the cellulose unit cell from those of a specimen that had been oven dried and then allowed to equilibrate to particular moisture content by water re-sorption.

From the results presented, it has been interpreted that drying stress does not cause the changes in cellulose unit cell dimensions, and that hydration and dehydration of cellulose are likely mechanisms for the changes seen in bulk wood material MOR with change in moisture content. Hydration of both the cellulose surface and the lignin – hemicellulose matrix may allow for applied load sharing thereby reducing internal strain. Hydrogen-bonded water molecules would act as a stress-transfer medium. As the moisture content decreases, there is also decrease in the EMC indicating a reduction in the hydrophilicity of the cellulosic crystal surfaces. This would have the effect of reducing the ability of the cellulose crystal surface to hydrogen bond to water and the matrix with the consequence of having a lesser ability to accommodate a load within the supra-molecular assembly. In cotton fibres, water mediated load sharing has been observed, but in this case the changes occurring on drying are direct cellulose – cellulose hydrogen bonding interactions (Nakamura et al. 1983). During drying, there has been shown to be a reduction in the unit cell *b* dimension, the source of this distortion may be cellulose intra-chain hydrogen bonds formed in surface chains. The resulting conformational changes to the surface of the cellulose crystal would explain the decrease in hydrophilic character and the reversible behaviour on rehydration (Newman and Davidson 2004) and changes in conformation cause changes in inter-chain hydrogen bonding (*i.e.* a change to the dimension of the unit cell parameter *b*).

2.7 Conclusions

This study has quantified the cellulose crystal lattice dimensions change as a result of moisture content change. This is observed as a change in the unit cell parameter *b* and the unique monoclinic angle *γ*. The causes of the change seem likely be a direct effect of the hydration state of the cellulose crystal surfaces.

Drying wood cell walls causes a reduction in the cellulose crystal monoclinic unit cell dimension *b* and the unit cell angle *γ* when compared to those unit cell dimensions of never dried-wood. During drying, there are changes to the crystal lattice $d(1\bar{1}0)$ and $d(110)$ inter-planar spacings, changes to $d(200)$ to a lesser degree, and no significant effect on the $d(002)$ dimension showing that changes are not driven by lateral expansion (Poisson's effect). The effects on the cellulose unit cell dimensions are partially reversible and are dependent on the degree and severity of drying. The degree of conversion of cellulose Iα to Iβ during high temperature drying does not explain the observed changes to the unit cell. It has been shown that it is critically important to account for the moisture content history of a wood specimen if meaningful comparisons between specimens are to be made.

It has now concluded that the changes that occur to the cellulose crystals dimensions are driven by the crystal surface hydration status. To examine the location and distribution of the water within the cell wall, the use of NMR spin diffusion techniques were employed. The following chapter (Chapter 3) examines the type of NMR experiments that could be applied and methods of data analysis by using a model system. Chapter 4 then applies NMR theory developed in Chapter 3, utilising an idealised cellulose crystal with a cross-sectional diameter of 2.54 nm as obtained in this chapter, to construct a model for the water distribution in never-dried wood cell walls (Model 3, Figure 4.5a and Model 4, Figure 4.5b in Chapter 4).

2.8 References

Abe, K., Yamamoto, H. (2005) Mechanical interaction between cellulose microfibril and matrix substance in wood cell wall determination by x-ray diffration. Journal of Wood Science. 51:334-338

Australian_Synchrotron. (2009) http://www.synchrotron.org.au/index.php/about-us/operations/syn-light-source

Bilderback, D.H., Elleaume, P., Weckert, E. (2005) Review of third and next generation synchrotron light sources. Journal of physics B: Atomic, molecular, and optical physics. 38:S773-S797

CCDC. (2010) http://www.ccdc.cam.ac.uk/products/mercury/

Clair, B., Almeras, T., Yamamoto, H., Okuyama, T., Sugiyama, J. (2006) Mechanical behavior of cellulose microfibrils in tension wood, in relation with maturation stress generation. Biophysical Journal. 91:1128-1135

Davidson, T.C., Newman, R.H., Ryan, M.J. (2004) Variations in the fibre repeat between samples of cellulose I from different sources. Carbohydrate Research. 339:2889-2893

Diddens, I., Murphy, B., Krisch, M., Muller, M. (2008) Anisotropic elastic properties of cellulose measured using inelastic X-ray scattering. Macromolecules. 41:9755-9759

Gjonnes, J., Norman, N., Viervoll, H. (1958) The state of order in cellulose as revealed from x-ray diffractograms. Acta Chemica Scandinavica. 12:489-494

Hubbard, C.R., Swanson, H.E., Mauer, F.A. (1975) A silicon powder diffraction standard reference material. Journal of Applied Crystallography. 8:45-48

Hura, G., Russo, D., Glaeser, R., Head-Gordon, T., Krack, M., Parrinello, M. (2003) Water structure as a function of temperature from x-ray scattering experiments and *ab initio* molecular dynamics. Physical Chemistry Chemical Physics. 5:1981-1991

Jakob, H.F., Tschegg, S.E., Fratzl, P. (1996) Hydration dependence of the wood-cell wall structure in *Picea abies*. A small-angle x-ray scattering study. Macromolecules. 29:8435-8440

Leppanen, K., Andersson, S., Torkkeli, M., Knaapila, M., Kotelnikova, N., Serimaa, R. (2009) Structure of cellulose and microcrystalline cellulose from various wood species, cotton and flax studied by X-ray scattering. Cellulose. 16:999-1015

Murdock, C. (1930) The form of the x-ray diffraction bands for regular crystals of colloidal size. Physical Review. 35:8-23

Nakamura, K., Hatakeyama, T., Hatakeyama, H. (1983) Effect of bound water on tensile properties of native cellulose. Textile Research Journal. 53:682-688
Nakamura, K., Wada, M., Kuga, S., Okano, T. (2004) Poisson's ratio of cellulose I_b and cellulose II. Journal of Polymer Science: Part B: Polymer Physics. 42:1206-1211

Newman, R.H. (1998) Evidence for assignment of ^{13}C NMR signals to cellulose crystallite surfaces in wood, pulp and isolated celluloses. Holzforschung. 52:157-159

Newman, R.H., Davidson, T.C. (2004) Molecular conformations at the cellulose-water interface. Cellulose. 11:23-32

Newman, R.H., Hemmingson, J.A. (1998) Interactions between locust bean gum and cellulose characterized by ^{13}C n.m.r. spectroscopy. Carbohydrate Polymers. 36:167-172

Nishimura, H., Okano, T., Asano, I. (1981) Fine structure of wood cell walls I. Structural features of noncrystalline substances in wood cell walls. Mokuzai Gakkaishi. 27:611-617

Nishiyama, Y., Langan, P., Chanzy, H. (2002) Crystal structure and hydrogen-bonding system in cellulose Ib from synchrotron x-ray and neutron fiber diffraction. Journal of the Amercian Chemical Society. 127:9074-9082

Peura, M., Kolln, K., Grotkopp, I., Saranpaa, P., Muller, M., Serimaa, R. (2007) The effect of axial strain on crystalline cellulose in norway spruce. Wood Science and Technology. 41:565-583
Saxena, I.M., Brown, R.M.J. (2005) Cellulose biosynthesis: Current views and evolving concepts. Annuals of Botany. 96:9-21

Somerville, C. (2006) Cellulose synthesis in higher plants. Annual Review of Cell and Developmental Biology. 22:53-78

Sugino, H., Sugimoto, H., Miki, T., Kanayama, K. (2007) Fine structure changes of wood during moisture adsorption and desorption process analyzed by x-ray diffraction measurement. Mokuzai Gakkaishi. 53:82-89

Sugiyama, J., Okano, T., Yamamoto, H., Horii, F. (1990) Transformation of Valonia cellulose crystals by an alkaline hydrothermal treatment. Macromolecules. 23:3196-3198

Sugiyama, J., Vuong, R., Chanzy, H. (1991) Electron diffraction study on the two crystalline phases occurring in native cellulose from an algal cell wall. Macromolecules. 24:4168-4175

Suzuki, H., Kamiyama, T. (2004) Structure of cellulose microfibrils and the hydration effect in *Crytomeria japonica*: a small-angle x-ray scattering study. Journal of Wood Science. 50:351-357

Suzuki, Y., Momose, A., Sugiyama, H. (1998) Characterization of windows and filters for coherent X-ray beamlines. Journal of Synchrotron Radiation. 5:596-599

Tesa_SE. (2010) http://www.tesa.com/industry/products/tesa(r)_51408.html

3 NMR pulse sequences for the study of solid materials

3.1 Introduction to NMR experiments for the investigation of polymeric materials

There are a range of NMR experiments and tools available for the study of solid materials. Those useful for study of natural and synthetic polymers will be discussed in this chapter, with special reference to spin diffusion techniques. Spin diffusion experiments allow the spatial arrangement of polymer components to be investigated. Wood is a natural composite of polymers, and much of what has been developed in the field of NMR and applied in the areas of plastics and synthetic polymers can be applied also to the study of wood.

In this thesis, NMR was used to address a fundamental question concerning the structural arrangement relating to "molecular Velcro®". In particular, it is shown in Chapter 4 that spin diffusion effects can reveal structural proximity and the presence of interfacial water. In this chapter, the basic NMR methods to be employed in this thesis are described.

To illustrate the methods and pulse sequences that were utilised to study wood cell walls, a model system was first employed to validate NMR pulse sequences. Selection of appropriate pulse sequences and validity of these to apply to study of wood/water structures was important in order to achieve good signal to noise responses in sufficiently short timeframes that mitigated against the specimen undergoing moisture content and therefore structural change. The NMR data acquisition time presents therefore different challenges from that at the synchrotron, where diffraction data were obtained virtually instantaneously.

Polyethylene was chosen as a test system due its excellent NMR response, and that it had been previously well characterised using solid state NMR (Cheung et al. 1980; Cheung 1982; Kitamaru et al. 1986; VanderHart and Perez 1986; Newman 1991; Mowery et al. 2006). Polyethylene is the common name of the polymer polyethene (or poly(methylene)). It is manufactured from ethylene by either radical, anionic, cationic, or ion coordination polymerisation methods (Solomons 1988). Each of these methods results in different isomers of polyethylene. High-density polyethylene (PE) as used in this study is defined

as having a density of equal to or greater than 0.941 g/cm^3 (Jubb 1975). This is usually produced using ion coordination type polymerisation to create a low branching, high molecular weight linear polymer. As the polymer solidifies it forms a lamellar structure in which alternating lamellae of crystalline and non-crystalline polymers have thicknesses of the order of tens of nanometres (Popescu-Pogrion and Tirnovan 1998). Knowledge of polymer domain dimensions is required to calibrate and evaluate NMR methods that are based on proton spin diffusion rates.

3.2 Molecular motion detected by NMR spectroscopy of spin-1/2 nuclei

Relaxation of magnetisation in an NMR experiment is dependent on the molecular motions of the system and the distance between adjacent nuclei. The two mechanisms of relaxations are; T_1 or spin-lattice relaxation, and T_2 or spin-spin relaxation.

The relaxation mechanisms for spin-1/2 nuclei are *via*; dipole-dipole coupling, chemical shift anisotropy, and spin rotation (Levitt 2002). Of these mechanisms, homonuclear dipole-dipole coupling is prevalent in proton rich systems such as wood, and will be discussed further.

T_1 relaxation

T_1 relaxation is the redistribution of spin populations back to thermal equilibrium, meaning a Boltzmann distribution, after being perturbed by an NMR pulse. The perturbation from the thermal equilibrium by an NMR pulse is a result of absorbed radiation causing a transition from “spin-up” (aligned with the external magnetic field) to the higher energy “spin-down” state (aligned against the external magnetic field). When the populations of the higher and lower energy states are equal, the system is saturated, and no NMR signal is detected. Under T_1 relaxation, thermal equilibrium is re-established (Figure 3.1).

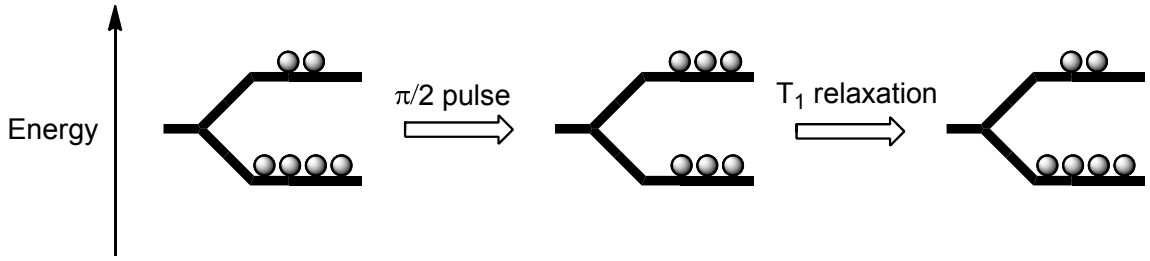

Figure 3.1 *Example of energy absorbed by a spin-1/2 system promoting spins to a higher energy state (in this case to saturation) and then over time relaxing back to ground state under T_1 relaxation.*

$T_{1\rho}$ relaxation

$T_{1\rho}$ relaxation is similar to T_1 relaxation in mechanism, but rather than equilibrating in the Z-axis (B_o) the relaxation is in the X/Y-axis, which rotates about the Z-axis at the NMR precession frequency. This X,Y,Z frame is known as the rotating frame and will be used henceforth to describe magnetisation behaviour. Spin locking in this rotating frame is achieved by applying a strong magnetic field (B_1) that is perpendicular to the main B_0 magnetic field, and likewise rotates about the Z-axis at the NMR precession frequency.

T_2 relaxation

T_2 relaxation is the rate at which magnetic coherences decay in the X/Y plane. The magnetic coherences are created by an NMR pulse, usually by the application of a π/2 pulse. Assuming an instantaneous π/2 pulse, all spins start in phase (coherent), but random fluctuations of the local magnetic field cause the precession frequencies of spins to differ over time, and this brings about ultimately a complete de-phasing with the result being a loss on NMR signal (Figure 3.2).

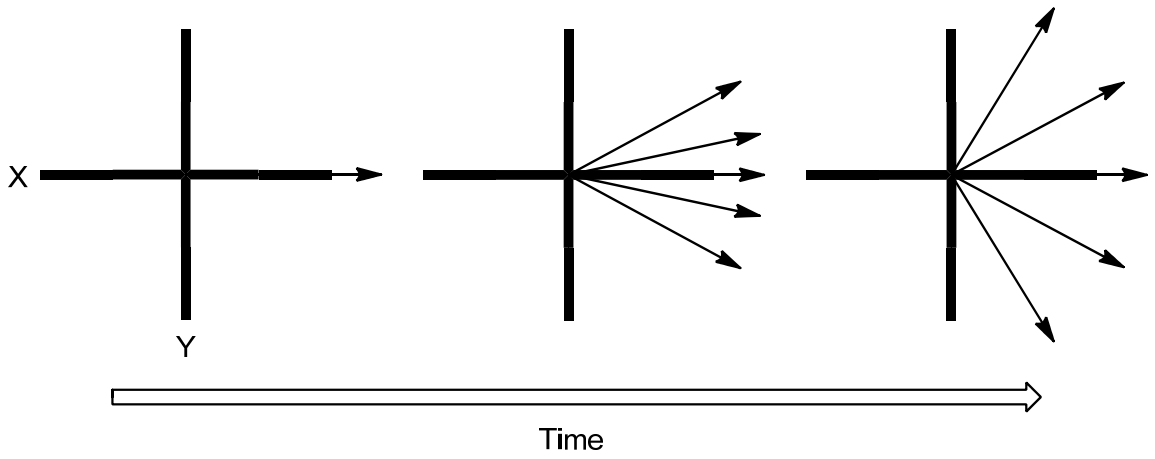

Figure 3.2 *T_2 relaxation of the loss of magnetisation coherence with time.*

Dipole-dipole interactions as a source of NMR relaxation

As mentioned above, fluctuations in the local magnetic field as felt by a spin cause relaxation, the most prevalent source of these fluctuations in spin-1/2 systems being due to dipole-dipole coupling. Dipole-dipole coupling is the interaction of nuclear spins through space and is dependant not only on the distance between the spins but also on their relative orientation to each other with respect to the main magnetic field (B_o) (Figure 3.3).

Molecular motion causes the relative angle (θ) between spins to change with time and is the source of the magnetic fluctuations.

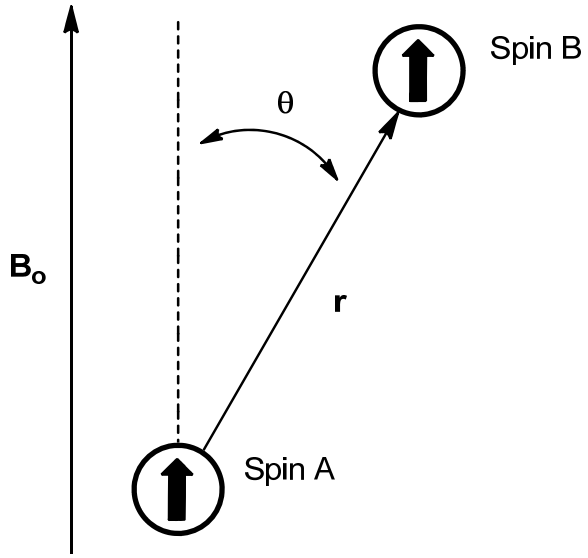

Figure 3.3 *Fluctuations in the local magnetic field caused by dipole-dipole interactions.*

Estimating relaxation parameters from molecular distance and motion

Assuming the main homonuclear dipole-dipole coupling present is due to proton interactions, then the following Equations (3.1a, 3.1b, and 3.1c) can be used to estimate relaxation times (Abragam 1970; Bruker 2009);

$$T_1 = K \times \{(3/2)\,[J_1(\omega) + J_2(2\omega)]\} \qquad 3.1a$$

$$T_{1\rho} = K \times [(3/8)\,J_0(\omega) + (15/4)\,J_1(\omega) + (3/8)\,J_2(2\omega)] \qquad 3.1b$$

$$T_2 = K \times [(3/8)\,J_0(0) + (15/4)\,J_1(\omega) + (3/8)\,J_2(2\omega)] \qquad 3.1c$$

Here, $1/K = [(\mu_0 \times 10^{-7} / 4\pi)^2\ \gamma^4_H\ \hbar^2\ I(I+1)] / r^6_{HH}$ which is the square of dipole-dipole coupling constant and,

$J_q(\omega) = C_q[\tau_c / (1 + \omega^2\ \tau_c^2)]$ which are the spectral density functions and;

$q = 0, 1, 2$ and $C_0 = 24/15,\ C_1 = 4/15,\ C_2 = 16/15$,

and ω is the rotational frequency of the B_0 magnetic field and τ_c is the rotational correlation time constant. γ is the nuclear magnetogyric ratio (not to be confused with the symbol used to define the crystal cell unit monoclinic angle in the previous chapter).

From these relationships, it can be seen that the relaxation times of a system are dependent on fluctuations in molecular orientation. T_1 relaxation is most efficient when

frequencies of the main magnetic field and the molecular motion (τ_c^{-1}) are proportional to each other. There are three cases (Equations 3.2a, 3.2b, and 3.2c);

$$\tau_c >> 1 / \omega \qquad 3.2a$$

$$\tau_c \approx 1 / \omega \qquad 3.2b$$

$$\tau_c << 1 / \omega \qquad 3.2c$$

In the cases of Equation 3.2a and 3.2c, the molecular motions are either too slow or too fast, respectively, to interact with the main magnetic field to give the most efficient T_1 relaxation. In the case of Equation 3.2b, the frequency of molecular motion and the main magnetic field are matched so energy transfer (T_1 relaxation) is at maximum efficiency, meaning short T_1 values. The plot of Equations 3.1a and 3.1b assuming a B_0 of 200.13 MHz (proton frequency in a Bruker 4.7T magnet, Figure 3.4) show minima in T_1 and $T_{1\rho}$ relaxation time constants at a rotational correlation time of *ca.* 0.8 ns (Figure 3.4). T_2 on the other hand has a field independent term (Equation 3.1c, $J_0(0)$), making it dependent in part only on the correlation time (τ_c), and, as such, T_2 relaxation times unlike T_1 relaxation times do not show a minimum (Figure 3.4).

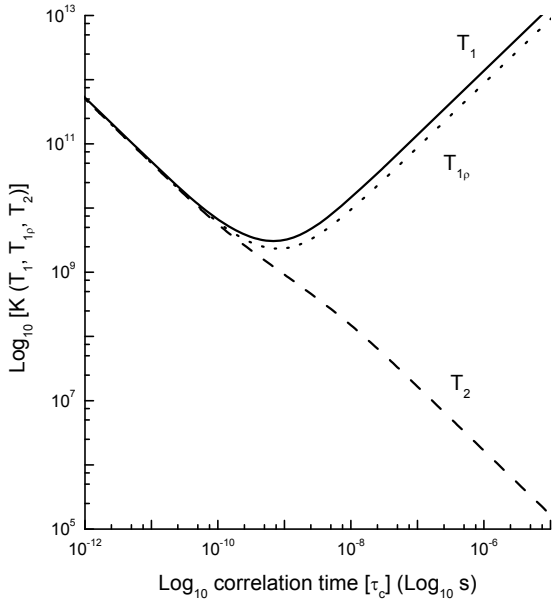

Figure 3.4 *T_1, $T_{1\rho}$, and T_2 relaxation as a function of rotational correlation time for ^{1}H NMR at 200.13 MHz. Curves calculated from Equations 3.1a, 3.1b, and 3.1c.*

3.3 NMR pulse sequences and their application to polymer systems

Carbon-13 Cross Polarisation Magic Angle Spinning NMR (^{13}C CP-MAS NMR)

The relaxation and spin diffusion effects to be examined in this thesis concern the proton and its abundance in all biopolymers and of course in water. However, because proton linewidths are very broad in the solid state and the chemical shift range is small, the proton is not the ideal vehicle for detection. Instead, by using natural abundance ^{13}C (*ca.* 1%) and taking advantage of the broad chemical shift spread and narrow spectral lines, proton relaxation and spin diffusion can be detected indirectly since protons are intimately coupled to ^{13}C and capable of magnetisation transfer. This device, which enables such indirect measurements, is ^{13}C cross-polarisation magic-angle spinning (CP-MAS) NMR.

The standard CP-MAS pulse sequence consists of a proton preparation pulse followed by a contact pulse on both the proton and carbon channels such that Equation 3.3 is satisfied allowing magnetisation to transfer from ^{1}H to ^{13}C nuclei. This is followed by detection on the carbon channel while simultaneously decoupling on the proton channel (Figure 3.5). This technique has the advantage of increasing signal to noise by a theoretical factor of *ca.* 4 (γ_H/γ_C) and allowing the fast relaxation rate of the protons to determine the minimum recycle delay between pulses.

$$\gamma_{1H}B_{1H} = \gamma_{13C}B_{13C} \qquad 3.3$$

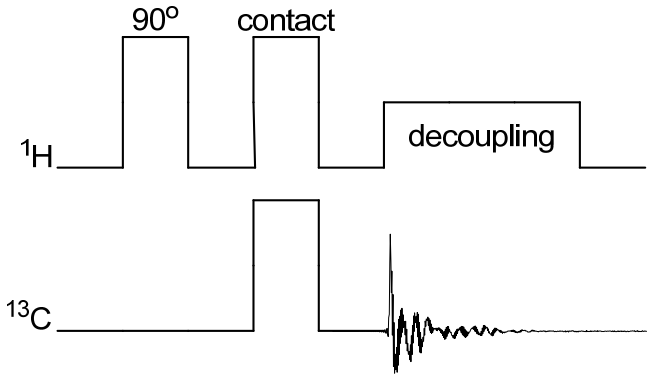

Figure 3.5 *Standard ^{13}C CP-MASNMR pulse sequence (rectangles = RF pulses, damped oscillation = NMR signal.*

For clarity, all other pulse sequences presented in this chapter will have the ^{13}C channel omitted as it consists only of a single “contact pulse” and “data acquisition”.

A sample of high-density polyethylene (PE) was obtained from a local source, and was used in all of the following experiments. Samples for the NMR study were cut into approximately 0.5 mm squares. The sample fragments were placed in a 7 mm zirconia rotor and spun at 5 kHz in a Bruker SB-BL7 doubly-tuned $^{1}H/^{13}C$ MAS probe on a Bruker Avance 200 MHz spectrometer operating at 200.13 MHz ^{1}H, and 50.33 MHz ^{13}C. A 5 µs 90^{o} carbon (50 kHz) and 5.6 µs proton (*ca.* 45 kHz) pulse was used. The Hartmann-Hahn cross-polarisation matching condition was optimised by adjusting the proton pulse power. Proton decoupling was achieved during acquisition of the ^{13}C FID by using a proton continuous wave field of strength of *ca.* 179 kHz. The proton decoupling resonance frequency was adjusted to maximise the signal intensity. The ^{13}C CP-MAS NMR spectrum of PE showed the characteristic crystalline (32.6 ppm) and amorphous (30.7 ppm) molecular domains (Kitamaru et al. 1986), shown in Figure 3.6. Chemical shifts were referenced to the carbonyl peak of glycine at 176 ppm with respect to TMS at 0 ppm (Tang et al. 1999).

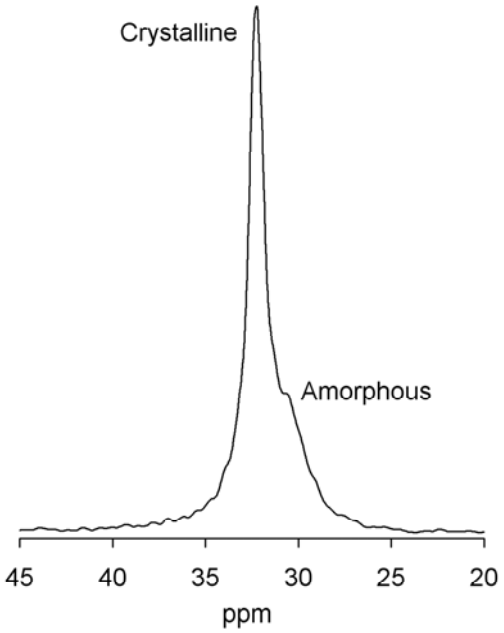

Figure 3.6 *^{13}C CP-MAS NMR spectrum of polyethylene showing crystalline (32.6 ppm) and amorphous (30.7 ppm) CH_2 resonances.*

The crystalline peak was fitted using a Lorentzian function and a degree of crystallinity of 73.4% was found for this sample of PE (Figure 3.7). This compares well with the crystallinity of 74% reported previously (Newman 1991).

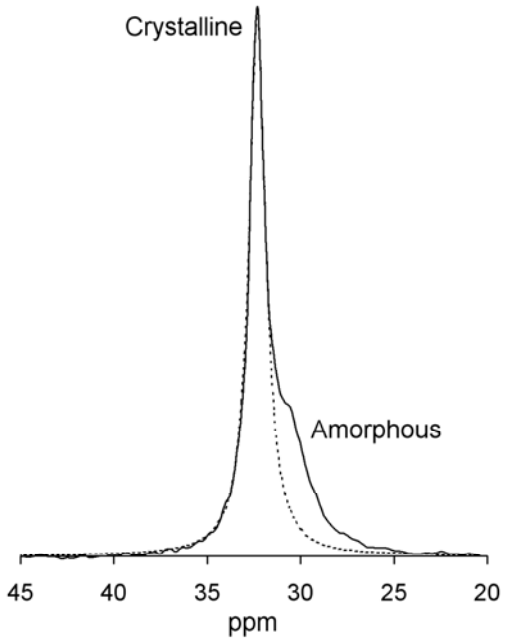

Figure 3.7 *Peak line fitting of the crystalline PE.*

Modelling of relaxation experiments

The determination of NMR relaxation constants is achieved by fitting functions to changes in NMR signal intensity with time. The usual functions applied are an exponential function (Levitt 2002), a Gaussian function (Newman 1987), and a Weibull function (Uehara et al. 2002; Uehara et al. 2007) (Equations 3.4a, 3.4b, and 3.4c respectively).

$$I = a \exp\{-t / T_x\} \qquad 3.4a$$

$$I = a \exp\{-t^2 / (2T_x^2)\} \qquad 3.4b$$

$$I = a \exp\{-t^{\mu} / (\mu T_x^{\mu})\} \qquad 3.4c$$

In these equations, I is the signal intensity, a is a constant, t is the time allowed for the relaxation to occur, T_x is the relaxation constant (i.e. T_1, $T_{1\rho}$, or T_2), and μ is an exponential factor for the Weibull function. It can be seen that an exponential function and a Gaussian

function are extremes of the more generalised Weibull function where μ = 1 is an exponential function and μ = 2 is a Gaussian function.

Spin-lattice relaxation (T_1)

This describes the exponential decay of the Z-component of the bulk magnetisation vector after the application of an NMR pulse (i.e. an applied B_1 field). The typical values of T_1 are ms to s and are dependent on the nuclei in question. To measure the T_{1H} of solids, a modified CP-MAS sequence is used that includes an inversion-recovery proton pulse sequence prior to the contact pulse (Figure 3.8). As employed in solution state NMR spectroscopy, the ^1H magnetisation is flipped into the –Z-axis where it is allowed to relax under T_{1H} in the absence of T_{2H} (see later) interferences. After a time the ^1H magnetisation is then flipped into the X/Y plane followed by a contact pulse to transfer the magnetisation to ^{13}C. The signal intensity of the ^{13}C is then related to the T_{1H} exponential decay of the ^1H magnetisation.

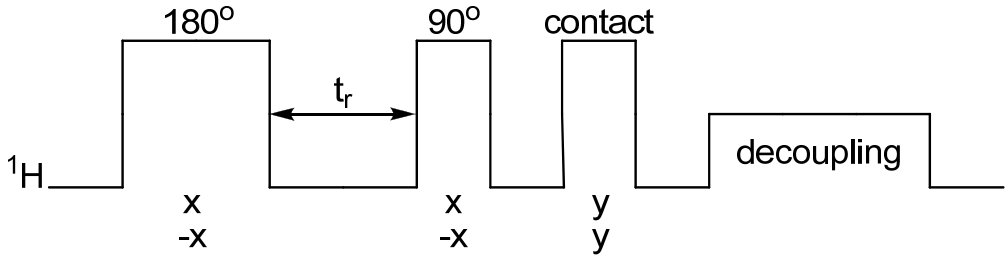

Figure 3.8 *Inversion recovery CP pulse sequence (t_r = recovery delay).*

An inversion-recovery plot shows an exponential signal recovery, (1 - exp{-t / T_{1H}}), for the crystalline and amorphous phases of PE (Figure 3.9).

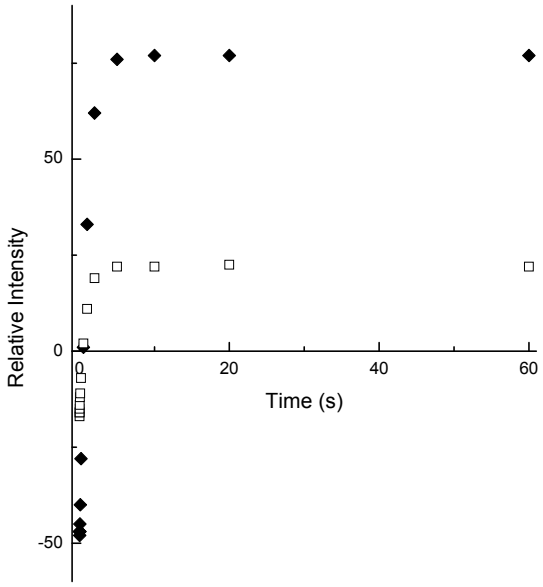

Figure 3.9 *T_{1H} inversion recovery experiment of PE (closed symbol = crystalline, open symbol = amorphous).*

By subtracting the long recovery time intensities (effective t_∞) from each recovery time and taking the natural logarithm of the resulting intensities, a linear plot can be constructed (Figure 3.10). From a linear fit of the data the T_{1H} values have been calculated by taking -1/slope for each component of the specimen under study. A T_{1H} of 0.94 s (curve fit RMS 0.01) was found for the crystalline PE phase, and T_{1H} of 0.80 s (curve fit RMS 0.02) for the amorphous phase.

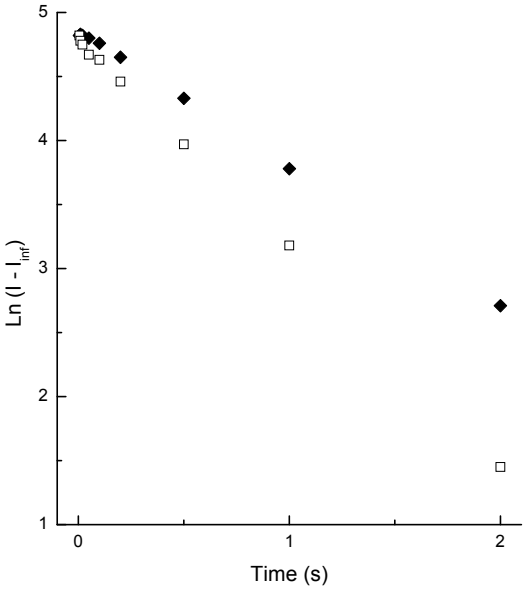

Figure 3.10 *T_{1H} inversion recovery experiment with high-density PE (closed symbol = crystalline phase, open symbol = amorphous phase).*

The greater T_{1H} value for the crystalline phase suggests that the sample was a mixture of high and low crystalline fragments, alternatively and more likely, the difference may arise from the difficulty of separating the crystalline and amorphous signals introducing experimental error.

Spin-spin relaxation (T_2)

This mode of relaxation is a loss of magnetisation coherence in the X/Y-plane. T_{2H} can be measured by placing the ^1H magnetisation in the X/Y plane and allowing a time to pass, and then reading the resulting FID. A modified CP sequence method devised by Alla and Lippmaa (Alla and Lippmaa 1976) uses a {90° – delay} on the proton channel coupled with a CP sequence (Figure 3.11).

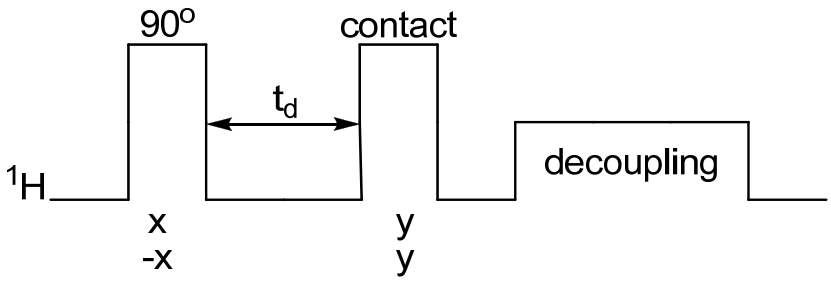

Figure 3.11 *Pulse sequence for determining T_{2H} relaxation.*

When either an exponential or a Gaussian function is applied to the T_{2H} decay of PE, it can be seen that neither function can be used to describe a linear fit for the crystalline and amorphous phase magnetisation decay (Figure 3.12 & 3.13 respectively).

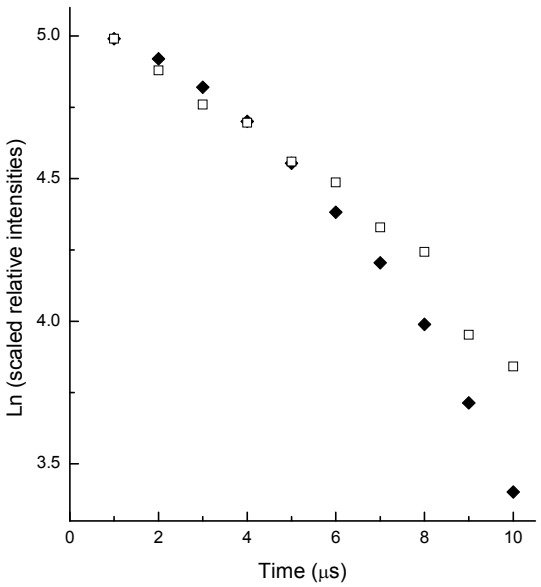

Figure 3.12 *PE T_{2H} by {90° - delay} technique fitted with an exponential function (closed symbol = crystalline phase, open symbol = amorphous phase).*

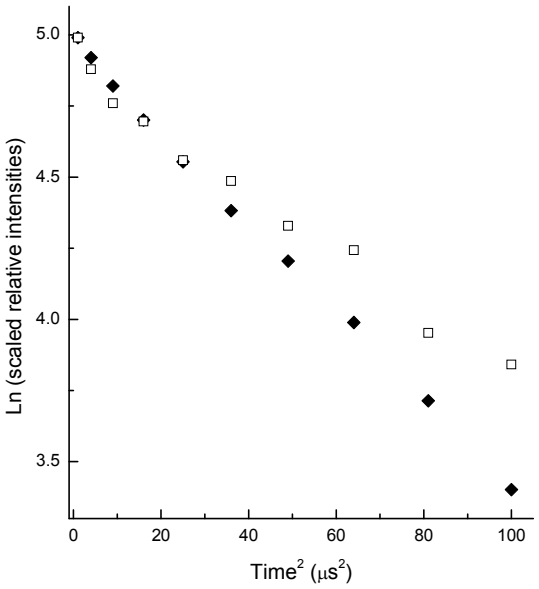

Figure 3.13 *PE T_{2H} by {90° - delay} technique fitted with a Gaussian function (closed symbol = crystalline phase, open symbol = amorphous phase).*

The resulting calculated T_{2H} decay time constants are 5.8 µs (curve fit RMS 0.10) for the crystalline phase and 12.0 µs (curve fit RMS 0.04) for the amorphous phase when fitting an exponential function. When fitted with a Gaussian function, values of 8.0 µs (curve fit RMS 0.02) and 11.6 µs (curve fit RMS 0.03), respectively, were found.

This demonstrates the dilemma of a applying a simple fit to polymer phases consisting of differing molecular mobility and/or composition.

A further approach exploits the fact that loss of magnetisation coherence begins immediately at the onset of a pulse. This can be seen from the equations that describe macroscopic magnetisation components after an initial pulse (Equation 3.5), where *M* is the magnetisation along either the X or Y-axis, on this case the X-axis (M_x) was used, ω_o is the Larmor frequency of the nucleus, *t* is the time from when the magnetisation was taken out of thermal equilibrium, and T_{2H} is the proton transverse relaxation time constant (Levitt 2002).

$$M_x = M_x^\circ \exp\{-t / T_{2H}\} \qquad 3.5$$

During a proton pulse, T_{2H} relaxation is occurring, and over the short time required for a single 90° pulse (a few µs) this relaxation can be ignored in most cases. As the proton magnetisation tip angle increases, the effect of the T_{2H} relaxation can become significant. It has been reported that this phenomenon could be employed to measure T_{2H} relaxation rates (Newman 1987). The damping of the signals can be described by a modified Weibull function with a time scale stretched by an exponential factor of 2 (Equation 3.6) (Barnaal and Lowe 1963; Goldburg and Lee 1963).

$$I = I_o + A \exp\{-(t^\mu) / (\mu 2^\mu T_{2H}^\mu)\} \times \sin(\pi(t - t_s) / t_{180^\circ}) \qquad 3.6$$

Here *I* is the NMR signal intensity, I_o is an intensity offset, *A* is the amplitude, *t* is the time of the applied B_1 pulse, t_s a the time for phase shift, t_{180} is the time to invert the magnetisation, and μ is an exponential that describes the shape of the damping oscillation with µ = 1 being a exponential function and µ = 2 being a Gaussian function. The transverse relaxation constant T_2 is multiplied by a factor of 2 due to the perturbation occurring on average approximately only half the time during a full 360° rotation with a maximum relaxation occurring in the X/Y plane and zero relaxation in the ±Z direction

(Newman 1987). In this study, a pulse sequence was used with a range of tip angles from 10's of degrees to 100's of degrees with the signal resulting from the magnetisation component in the X/Y-plane at the time of the contact pulse (Figure 3.14).

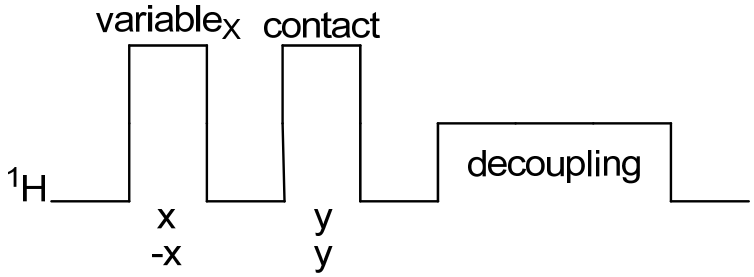

Figure 3.14 *Nutation CP-MAS pulse sequence for determining T_{2H} (Variable$_X$ = a variable pulse in the X-axis resulting in a variable magnetisation tip angle).*

Changes in the ^{13}C signal intensity were measured as the proton magnetisation tip angle was varied. The normalised plot of the ^{13}C signals attenuation with increasing proton preparation pulse magnetisation tip angle can be described by a dampened sinusoid (Figure 3.15). As can be seen, initially the signal intensities for each phase track each other, but as the nutation time increases the difference in T_{2H} values between the crystalline and amorphous phases cause divergence in the relative signal intensities.

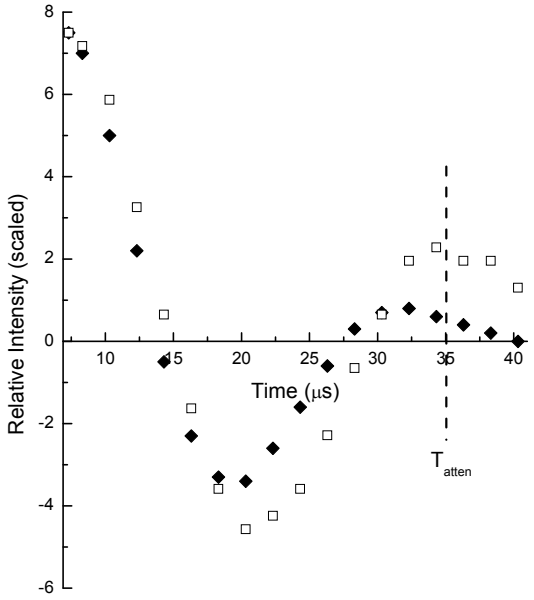

Figure 3.15 *Attenuation of crystalline and amorphous phases of PE due to nutation (closed symbol = crystalline phase, open symbol = amorphous phase).*

Neither an exponential nor a Gaussian function was able to fit the nutation decay data. To calculate the value of T_{2H} the data were fitted using Equation 3.6.

The nutation decay plots of the crystalline and amorphous phases of PE were fitted with a Weibull function (Equation 3.6). A T_{2H} value of 7.4 μs (curve fit RMS 0.04) where μ = 1.76 was found for the crystalline phase, and a T_{2H} value of 11.2 μs (curve fit RMS 0.12) where μ = 1.79, for the amorphous phase (Figure 3.16).

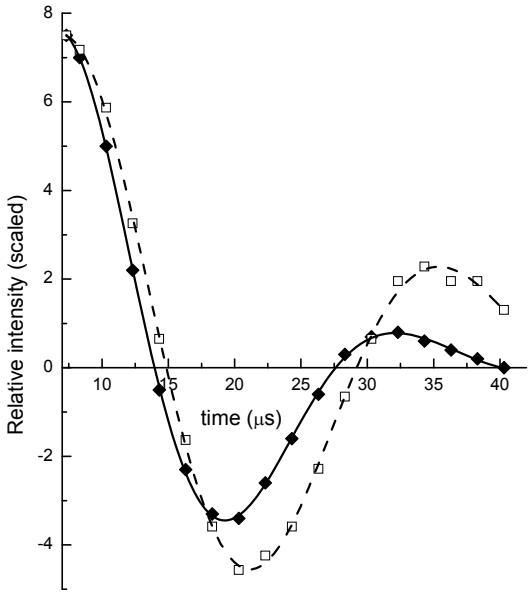

Figure 3.16 *PE T_{2H} by nutation using a Weibull function fit (closed symbol = crystalline phase, open symbol = amorphous phase).*

Ultimately, all methods of determining PE T_{2H} gave similar results, and showed that the crystalline phase has faster T_{2H} relaxation and the amorphous phase has slower T_{2H} relaxation. This would be expected given the more rigid state of the crystalline phase and its resulting stronger dipole-dipole couplings.

A summary of T_{2H} values obtained by the various fitting methods is summarised as Table 3.1.

Table 3.1 *Tabulated T_{2H} values for PE using the presented curve fitting methods for nutation data (number in brackets presents the fitting error (RMS)).*

Fitting type	*T_{2H} (μs) Crystalline phase*	*T_{2H} (μs) Amorphous phase*
Exponential	5.8 (0.1)	12.0 (0.04)
Gaussian	8.0 (0.02)	11.6 (0.03)
Weibull	7.4 (0.04)	11.2 (0.1)
Average (CoV)	7.1 (0.2)	11.6 (0.03)

RMS of curve fit given in brackets

Rotating frame relaxation ($T_{1\rho}$)

Two approaches can be taken for the measurement of $T_{1\rho H}$. The first is to vary the contact time. The carbon signal intensity from a cross polarisation experiment can be described by Equation 3.7, where I is the NMR signal intensity, I_o is the maximum possible intensity (where $T_{CH} << T_{1\rho}(H)$), T_{CH} is time constant for magnetisation build up on ^{13}C from ^{1}H, $T_{1\rho H}$ is the longitudinal proton relaxation constant (in the rotating frame), and t_{cp} is the contact pulse time (≤ 10 ms for Bruker instruments).

$$I = (I_o / (1 - (T_{CH} / T_{1\rho H}))) (exp\{-t_{cp} / T_{1\rho H}\} - exp\{-t_{cp} / T_{CH}\}) \qquad 3.7$$

A value for $T_{1\rho H}$ can then be obtained from the slope of a plot of the contact time versus natural log of the signal intensity taken after the magnetisation build-up time (T_{CH}) (Figure 3.17). However this approach suffers from the fact that an assumption must be made that after a certain time the exponential magnetisation build-up T_{CH} contribution can be ignored (i.e. only signal decay is occurring at long contact times). The single exponential T_{CH} also is a simplification in that proton spin diffusion contributes to the magnetisation build up rate (i.e. use of a single value of T_{CH} assumes that spin diffusion is much faster process than cross polarisation). In a single-phase system this may be appropriate, but in complex multi-phase systems, the ensemble of $T_{1\rho H}$ values may make the determination of what is purely a mono-exponential decay difficult.

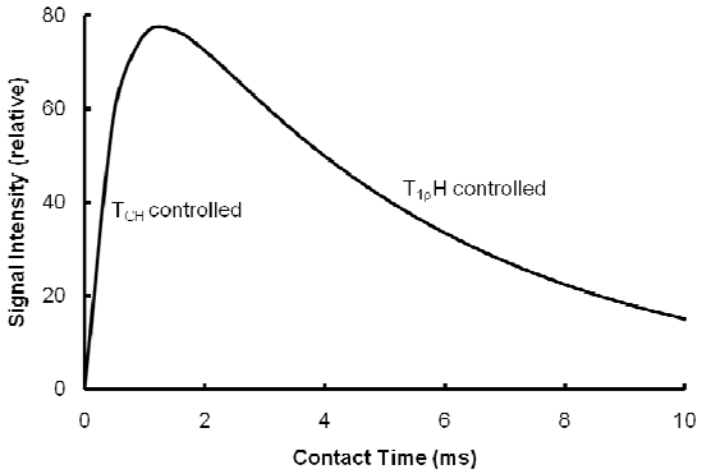

Figure 3.17 *Simulated CP magnetisation build-up and decay curve.*

The pulse sequence used in a variable contact experiment is presented as Figure 3.18.

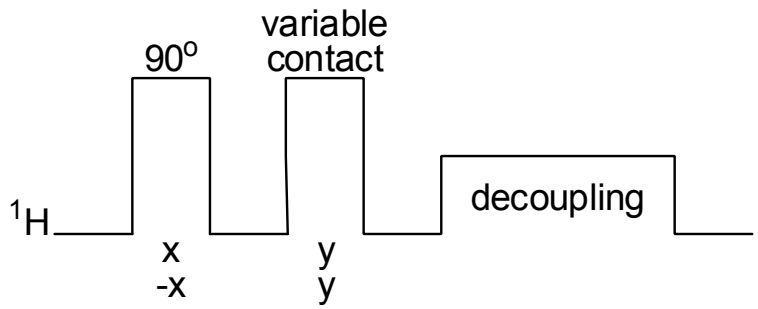

Figure 3.18 *Variable contact CP-MAS sequence for determination of magnetisation build-up and decay curves.*

The magnetisation build-up and decay curve for PE observed during a variable contact time experiment showed fast polarisation followed by slower decay (Figure 3.19). The fast polarisation is expected due to the molecular structure of PE being proton rich and a rigid solid, at least if the temperature is below the glass transition temperature (T_g). The T_g of PE has been estimated to be no higher than approximately -100 °C (Gaur and Wunderlich 1980).

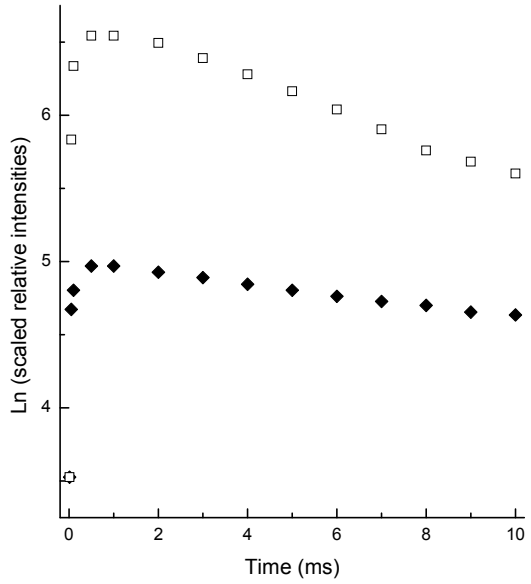

Figure 3.19 *Variable Contact Time experiment on Polyethylene (closed symbol = crystalline phase, open symbol = amorphous phase).*

Given as Figure 3.20 is the natural logarithm of the ^{13}C NMR signal versus the contact time at times ≥1 ms (i.e. the predominantly decay segment of the plot). This gives a $T_{1\rho H}$ value of 26.3 ms (curve fit RMS 0.01) for the crystalline phase of PE, and 16.1 ms (curve fit RMS 0.02) for the amorphous phase.

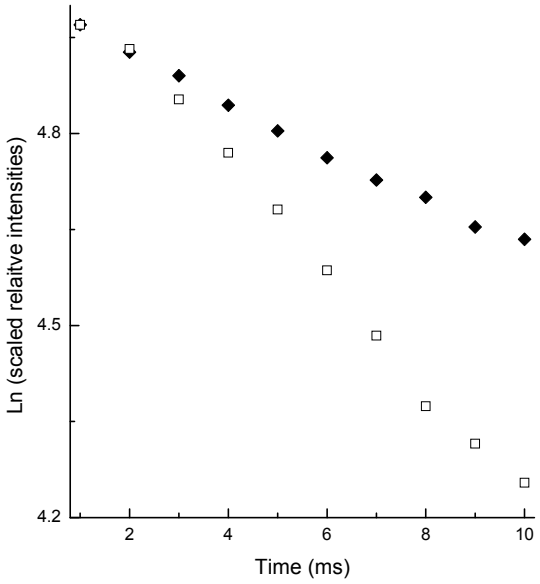

Figure 3.20 *Variable Contact Time experiment with PE, showing the natural log decay of the later part (≥1 ms) of the plot (closed symbol = crystalline phase, open symbol = amorphous phase).*

A further method for determining $T_{1\rho H}$ is the use of a variable spin-locking pulse prior to the contact pulse (Figure 3.21). This means that the protons relax under $T_{1\rho H}$ without cross polarising to the carbon nuclei. This has the advantage of disentangling the kinetics of T_{CH} and $T_{1\rho H}$, thereby providing a better estimate of $T_{1\rho H}$.

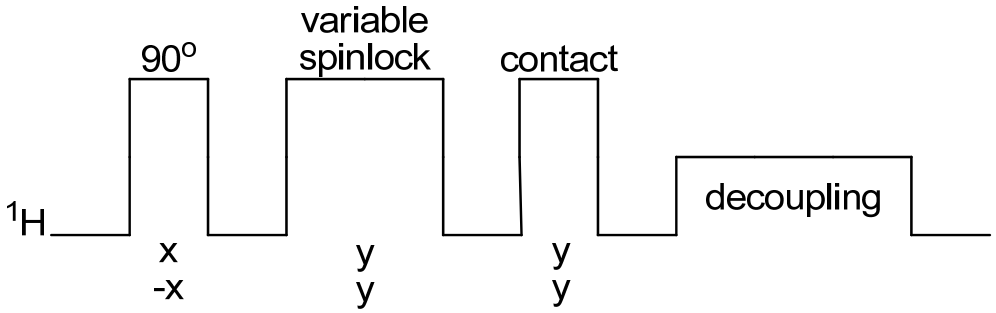

Figure 3.21 *Variable spinlock CP-MAS sequence for determining $T_{1\rho H}$.*

Using a variable spin locking pulse prior to the contact pulse, the $T_{1\rho H}$ PE was determined. By taking the natural log of the ^{13}C signal intensity as it related to the spin-locking time, $T_{1\rho H}$ was then calculated from the slope (Figure 3.22). Using this method, a value of $T_{1\rho H}$ for the PE crystalline phase of 25.7 ms (curve fit RMS 0.01) and the amorphous phase of 11.2 ms (curve fit RMS 0.32) were obtained.

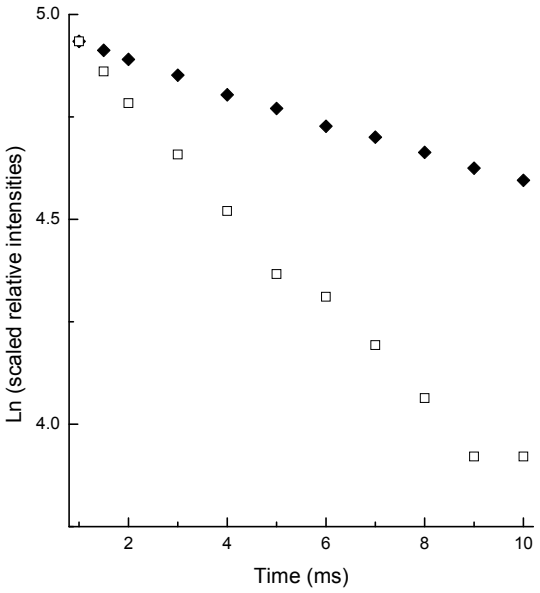

Figure 3.22 *Variable Spin Lock determination of $T_{1\rho H}$ (closed symbol = crystalline phase, open symbol = amorphous phase).*

Comparisons of the two methods showed the crystalline phase of PE has $T_{1\rho H}$ values of 26.3 ms for the variable contact time (VCT) method and 25.7 ms for the variable spin lock (VSL) method. For the PE amorphous phase, values of 16.1 ms for VCT and 11.2 ms for VSL were obtained. In the case of the PE crystalline phase, the faster proton spin diffusion meant that the apparent T_{CH} was expected to be shorter than that of the amorphous phase. At longer contact times, the effect of the cross polarisation on the final ^{13}C signal intensity was negligible, and as such, the VCT and VSL showed a similar $T_{1\rho H}$ value. In the case of the amorphous phase, due to greater molecular motion, there was a slower proton spin diffusion rate, resulting in a longer apparent T_{CH} (Duer 2004). This has the effect of making the $T_{1\rho H}$ value for the VCT experiment appeared longer due to continued contribution from cross polarisation at longer contact times influencing the shape of the curve. For this reason, VSL experiments are the preferred method of obtaining $T_{1\rho H}$.

3.4 NMR proton spin diffusion

The use of NMR to investigate the nanostructure of polymers by proton spin diffusion is well-established (Schmidt-Rohr et al. 1990). The principle is to create a perturbation in the magnetisation in differing domains of a polymer under study, and then observe the effects

of spin diffusion. These domains may be either molecularly different components of a heteropolymer or different phases of a homopolymer.
Spin diffusion is a process in which spin information is transferred from nucleus to nucleus by a process of spin flip-flops (Figure 3.23).

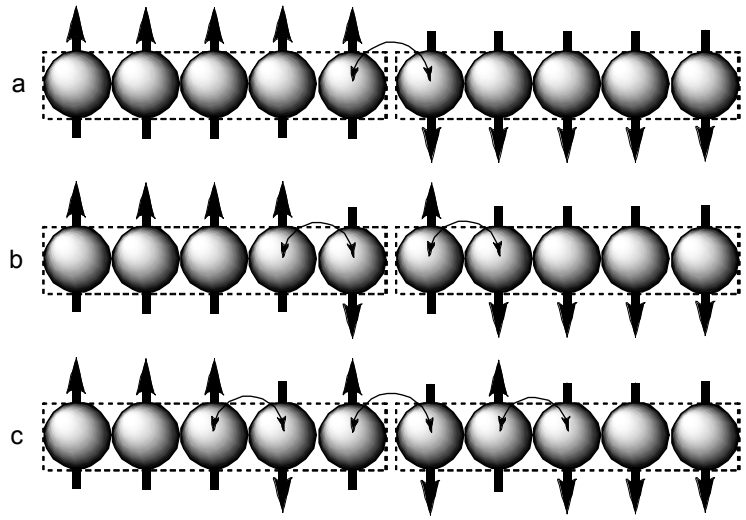

Figure 3.23 *A representation of spin diffusion both within a domain (dotted lines) and between domains. The double-headed arrows indicate nuclei pairs that will exchange spins shown as the sequence from 1a to 1b to 1c (The solid arrows do not imply an actual spin system, but are for illustrative purposes.*

The rate at which these spin flip-flops occur is expressed as the proton spin diffusion rate (*D*). Over time, the perturbation of the magnetisation is corrected *via* spin diffusion. The time in which it takes for this correction to take place is termed the mixing time (T_m).

This process of spin diffusion for simplicity is usually analysed assuming a two phase system and using Fick's second law of diffusion and assuming a heat flow type model (Equation 3.8) (Clauss et al. 1993).

$$\partial M(r,t) / \partial t = \nabla [D(r) \nabla M(r,t)] \qquad 3.8$$

In this equation, *M* is the magnetisation along the Z-axis, *D* is the spin diffusion coefficient, *r* is the distance vector, and *t* is the time for diffusion.

Various methods have been devised to investigate this phenomenon but in general, all consist of a perturbation of the magnetisation of one component relative to the other. This is followed by the bulk magnetisation being stored in the Z-axis to allow spin diffusion to

occur *via* zero and double quantum transitions (Demco et al. 1995). During this time, the mixing of the spin information *via* spin diffusion corrects the magnetisation perturbation. This is then followed by a reading step in which the resulting magnetisation is transferred back in the transverse plane for reading (Goldman and Shen 1965) (Figure 3.24). The mixing time is then related to the distance between the components, discriminated by the spin diffusion coefficient(s) of the materials.

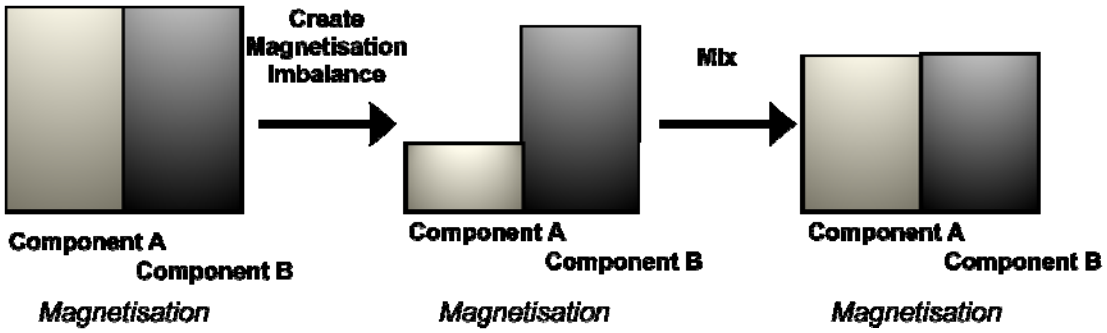

Figure 3.24 *Magnetisation perturbation of Component A relative to Component B causes a magnetisation imbalance between components, and then during the Mixing time spin diffusion corrects this perturbation.*

Various methods have been proposed to measure the proton spin diffusion in solids. Initially Zumbulyadis (Zumbulyadis 1983) suggested coupling the Goldman-Shen sequence (Goldman and Shen 1965) with a standard cross-polarisation sequence. This allowed the proton spin diffusion to be studied using ^{13}C CP-MAS NMR. This method has all the advantages of CP-MAS NMR spectroscopy such as the wider frequency range of carbon resonances compared with that of proton resonances (i.e. larger chemical shift range). This allows for better signal separation to visualise discrete peaks arising from differing types of structural domains (Newman 1991).

The requirement for CP-MAS ^{13}C NMR to be used for monitoring proton spin diffusion is that the spin diffusion mixing time (T_m) be much longer than the magnetisation build up time (T_{CH}) of the CP experiment. Furthermore, although not unique to the CP-MAS technique, T_m must be shorter than T_1 so that the overall sample Z-axis magnetisation isn't restored to thermal equilibrium before spin diffusion can act on the magnetisation perturbation (McBrierty and Douglass 1980). This means that, in general, $T_{1H} >> T_m > T_{contact} >> T_{CH}$, for CP-MAS ^{13}C NMR monitoring of proton spin diffusion to be utilised. If these conditions are not met, then in the case of $T_m \approx T_{CH}$, spin diffusion during the contact time will result in no magnetisation perturbation between domains, and in the case of $T_m \approx T_{1H}$, separation of the recovery of signal due to non-spin diffusion effects will make

analysis virtually impossible. Newman (Newman 1991) described an approach to minimise the effect of T_{1H} relaxation on proton spin diffusion by use of a subtraction/addition method. In this method, the effects of spin diffusion are additive and effects of T_{1H} relaxation tend to cancel each other by the use of two separate experiments with differing phase cycles. However, this modification only offsets the effect of T_{1H} and does not negate the influence of the T_{1H} relaxation entirely. A correction may be applied based on the T_{1H} of the sample (if known) by multiplying the intensities obtained by a factor of $\exp\{t_{mixing} / T_{1H}\}$ (Clauss et al. 1993).

The initial perturbation of magnetisation between differing polymer domains is setup by the use of a delay that allows magnetisation of one domain under the influence of some form of relaxation to deplete faster than the other. The relaxation parameter used depends upon the sample under investigation. Three methods of perturbation are discussed, one based on $T_{1\rho H}$ relaxation and the other two based on T_{2H} relaxation. The T_{2H} methods employ either a $\{90^{o}$ – delay$\}$ sequence or T_{2H} relaxation during magnetisation nutation to achieve differential domain magnetisation.

From spin diffusion measurements, it is possible to get an estimate of the size of the smallest domain (*i.e.* the limiting component). The smallest-sized domain representing the longest distance over which magnetisation has to diffuse to counteract the perturbation assumes that the spin diffusion rate is a constant over all domains. The domain size can be then be calculated from Equations 3.9a and 3.9b (Cheung and Gerstein 1981; Newman 1991), in which the mean dimension of the smaller domain (b) is determined from the spin diffusion coefficient (D), the mixing time to ameliorate the magnetisation perturbation (T_m) and a parameter that defines the geometry of the domains (n = 1 {lamellar}, 2 {rod-like}, or 3 {cubic or spherical}).

$$b = 2n\,(DT_m / \pi)^{1/2} \qquad 3.9a$$

This can be rearranged to,

$$T_m = \pi b^2 / 4n^2 D \qquad 3.9b$$

so that T_m can be calculated if b is already known.

Another more generalised method to estimate the length scale over which diffusion has occurred is to apply Equation 3.10a (Chen and Schmidt-Rohr 2006).

$$\langle x^2 \rangle = n2Dt \qquad 3.10a$$

Here, $\langle x^2 \rangle$ is the mean-square displacement at time (t) for a given diffusion coefficient (D). The parameter, n, is a dimensionality parameter defined as per Equation 3.9. In this case, the size of a domain can be determined when $t = T_m$, then Equation 3.10a can be rearranged to give Equation 3.10b.

$$T_m = \langle x^2 \rangle / 2nD \qquad 3.10b$$

Four methods for experimentally determining the proton spin diffusion mixing times are presented below. A proton spin diffusion efficient of 0.83 nm^2ms^{-1} for PE was used for all domain size calculations (Cheung and Gerstein 1981; Newman 1991).

$T_{1\rho H}$ Perturbation (millisecond time-scale, $T_{1\rho H}$ based selection)

$T_{1\rho H}$ selection suppresses the amorphous phase relative to the crystalline phase. This phase signal suppression is achieved by applying a proton X/Y-axis spin-lock pulse that allows $T_{1\rho H}$ relaxation to differentiate the magnetisation in the two phases. This is followed by magnetisation being transferred to the Z-axis for spin diffusion to occur. Finally a standard ^{13}C CP-MAS proton preparation pulse and contact pulse is applied and the resulting magnetisation is read on the carbon channel (Figure 3.25).

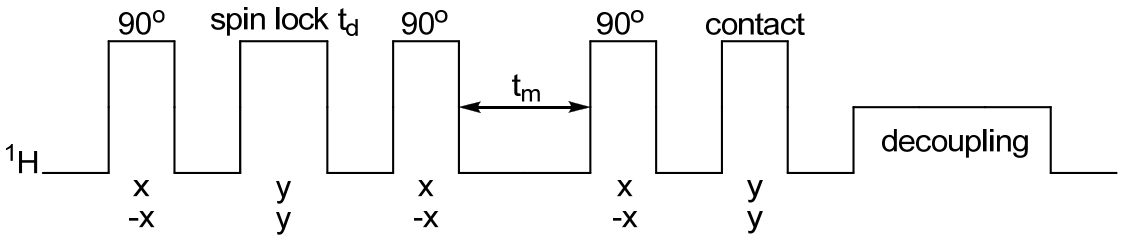

Figure 3.25 *Variable spin-lock pulse program for the perturbation of amorphous region and spin diffusion measurement.*

Because the time scale of $T_{1\rho H}$ relaxation is three orders of magnitude (i.e. milliseconds versus microseconds), longer than the T_{2H} relaxation, in general this method is only applicable where the domain sizes are sufficiently large so that magnetisation isn't averaged out by $T_{1\rho H}$ relaxation or spin diffusion (VanderHart and McFadden 1996). $T_{1\rho H}$

relaxation selects for the crystalline phase rather than the amorphous, recalling that the crystalline phase has approximately twice the time constant as the amorphous phase. In this case during spin diffusion, the magnetisation will transfer from the crystalline phase to the amorphous phase. After 20 ms of spin-locking the amorphous phase appears as only an indistinct shoulder on the crystalline peak, and then with the introduction of a mixing time, the amorphous peak reappears (Figure 3.26). At the longest mixing times, the spectrum resembles that of a standard CP-MAS spectrum of PE.

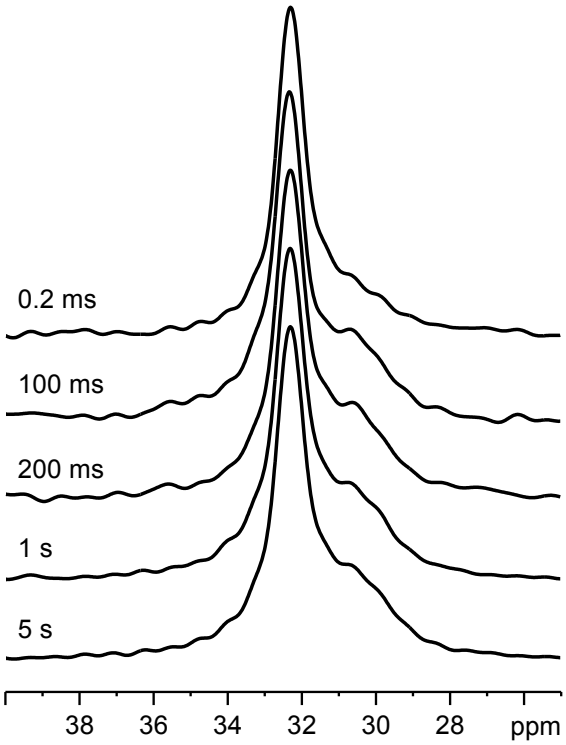

Figure 3.26 Spin diffusion after $T_{1\rho H}$ selection diminishes the magnetisation perturbation with increasing mixing time (normalised, left peak = crystalline phase, right peak = amorphous phase).

By taking the intercept of the relative signal intensity of the crystalline phase where this initially decreases, due to magnetisation transfer to the amorphous phase, and then increases, due to $T_1(H)$ relaxation, and plotting this against the square root of time gives the time at which the spin diffusion has mixed the spins of the two components (Figure 3.27). The crystalline peak was chosen as it was better defined compared to the amorphous peak at all mixing times. This occurred at $t^{1/2}$ = 5.25 $ms^{1/2}$, *i.e.* t = 0.028 s, and by applying Equation 3.9a, the crystalline domain size was calculated to be *ca.* 5.4 nm.

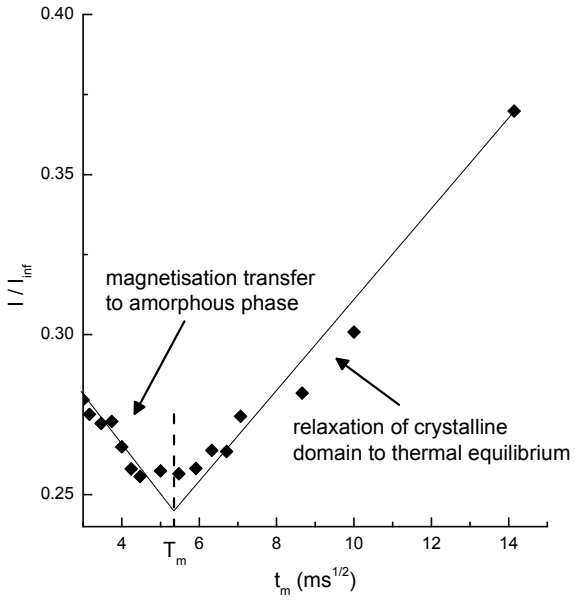

Figure 3.27 Crystalline PE peak intensity during spin diffusion experiment *(closed symbol = crystalline).*

Goldman-Shen (microsecond time-scale, T_{2H} based selection)

T_{2H} selection suppresses the crystalline phase relative to the amorphous phase due to the faster T_{2H} relaxation of the crystalline phase.

The first method to study spin diffusion was proposed by Goldman and Shen (Goldman and Shen 1965), and this involved a series of three 90° pulses with delays between the first and second pulses (Figure 3.28).

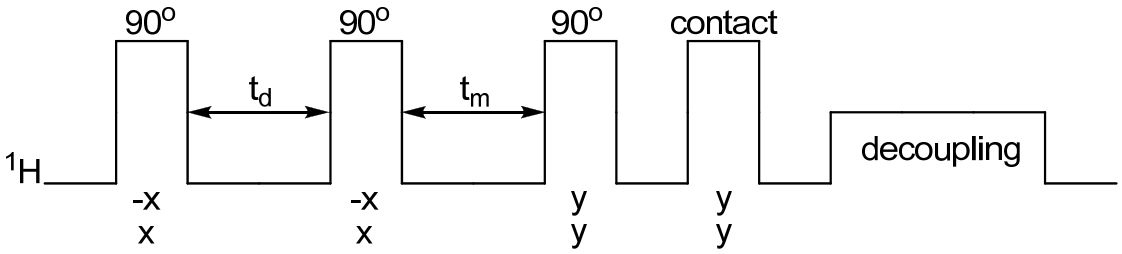

Figure 3.28 *Goldman-Shen ^{1}H channel pulse sequence modified for CP-MAS ^{13}C NMR.*

The first delay (t_d = dephase delay) preferentially dephases (i.e. cause a loss of magnetisation coherence) the molecularly rigid (i.e. crystalline) components under T_{2H} relaxation. This preferential dephasing of the more rigid component is due to stronger static dipolar couplings. The second 90° pulse transfers the magnetisation back into the Z-axis. During a second delay (t_m = mixing time) the exchange of spin information (spin

diffusion) occurs. This is followed by a third 90^{o} pulse that transfers the magnetisation into the transverse plane for reading. For use with a solid state ^{13}C CP-MAS pulse sequence, this is modified to include a contact time (to transfer proton magnetisation to adjacent carbons) and then decoupling on the proton channel as unlike the original Goldman-Shen pulse sequence the effect of proton spin diffusion is observed by changes to carbon signal intensities.

When applied to PE, the change in ^{13}C signal intensity of the crystalline and amorphous phases as a function of the square root of the mixing time (t_m) is plotted (Cheung and Gerstein 1981). The signal intensity of the amorphous resonance initially decreases due to magnetisation transfer (via spin diffusion) to the crystalline phase and consequently the crystalline signal intensity increases until the perturbation in magnetisation has been counteracted (Figure 3.29). The observed continued increase in signal is due to T_{1H} relaxation.

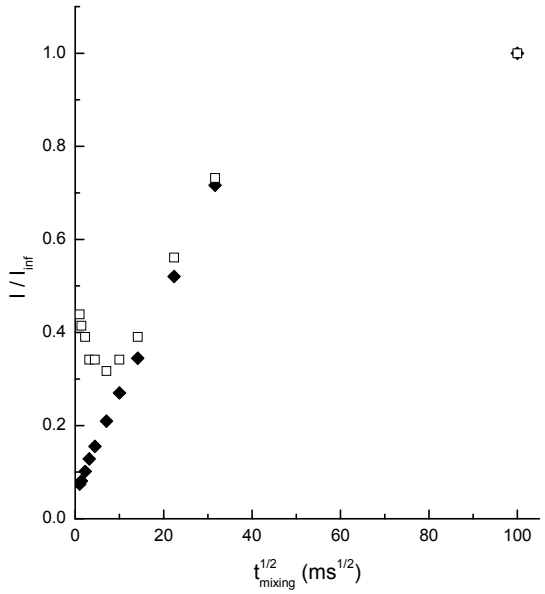

Figure 3.29 *Goldman-Shen pulse sequence using T_{2H} selection of magnetisation of amorphous and crystalline PE (closed symbol = crystalline phase, open symbol = amorphous phase).*

The point at which this magnetisation perturbation is counteracted (intercept of decay and increase in amorphous signal) is used to estimate the domain size of the amorphous phase (Figure 3.30).

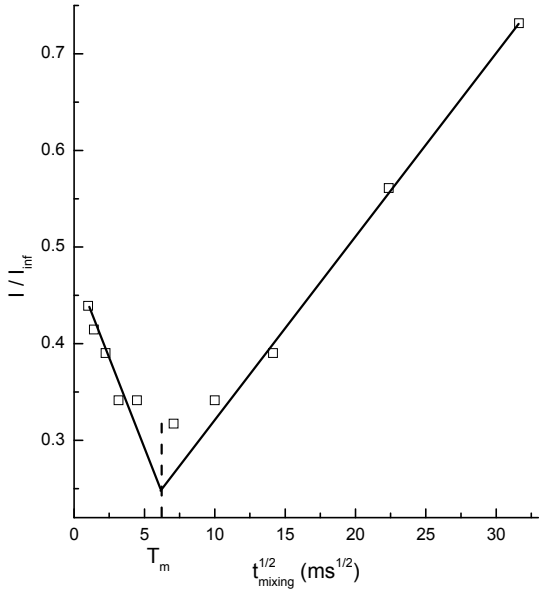

Figure 3.30 *Goldman-Shen experiment showing the spin diffusion mixing time of amorphous PE.*

The mixing of spin information due to spin diffusion (T_m) occurs at 6.2 $ms^{1/2}$, or 38 ms. From Equation 3.9a, a mean amorphous domain size of 6.4 nm was calculated.

The mixing time can also be deduced by taking the ratio of magnetisation source/sink intensities (Clauss et al. 1993). In this case, the intensity of the PE amorphous phase (magnetisation source) is divided by the intensity of the PE crystalline phase (magnetisation sink) for each mixing time (Figure 3.31).

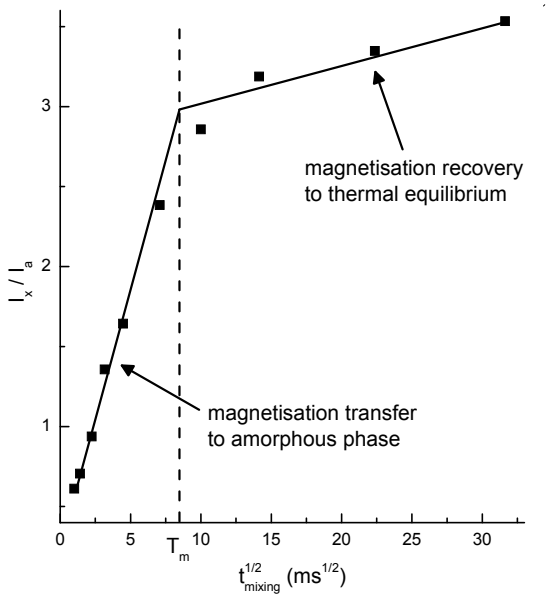

Figure 3.31 *Goldman-Shen experiment showing the spin diffusion mixing time obtained for PE.*

The mixing of spin information due to spin diffusion (T_m) occurs at 8.5 $ms^{1/2}$, or 72 ms. Using Equation 3.9a a mean amorphous domain size of 8.7 nm was calculated.

Another approach to minimise the influence of T_{1H} on the diffusion plot at long magnetisation mixing times is to apply Equation 3.11, where I_a and I_x are the intensity of the amorphous and crystalline signals respectively, and I^{inf} is the signal at a very long mixing time assuming complete mixing (Figure 3.32).

$$I_{a/x} = (I_a^{inf} - I_a) / (I_x^{inf} - I_x)\ (I_x^{inf} / I_a^{inf}) \qquad 3.11$$

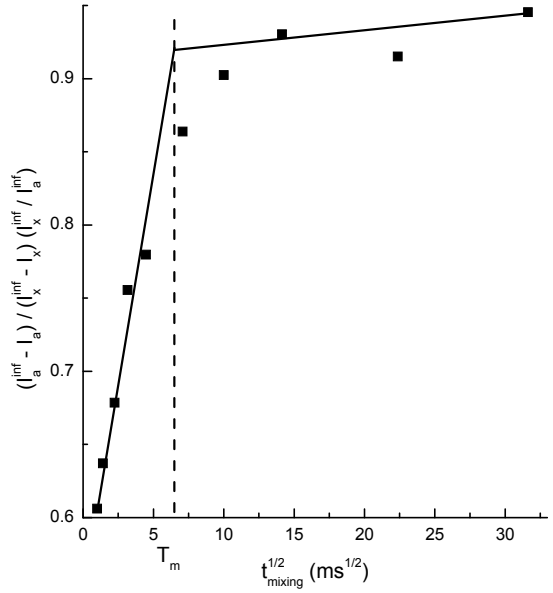

Figure 3.32 *Goldman-Shen experiment showing the spin diffusion mixing time of PE after applying Equation 3.11.*

The mixing of spin information due to spin diffusion (T_m) occurs at 6.3 $ms^{1/2}$, or 40 ms, giving mean amorphous domain size of 6.5 nm (Equation 3.9a).

Modified Goldman-Shen (microsecond time-scale, T_{2H} based selection)

If there is significant T_{1H} relaxation during the mixing time (t_m) then an apparent increase in signal intensity due to non-spin diffusion magnetisation recovery into the Z-axis is observed.

This lack of discrimination of non-spin diffusion signal recovery can be partially overcome by the use of a modified Goldman-Shen sequence (Packer et al. 1984; Zhang and Mehring 1989) and the data processing method developed by Newman (Newman 1991). This modification has an inverted pulse on the second 90^o pulse relative to the first (Figure 3.33).

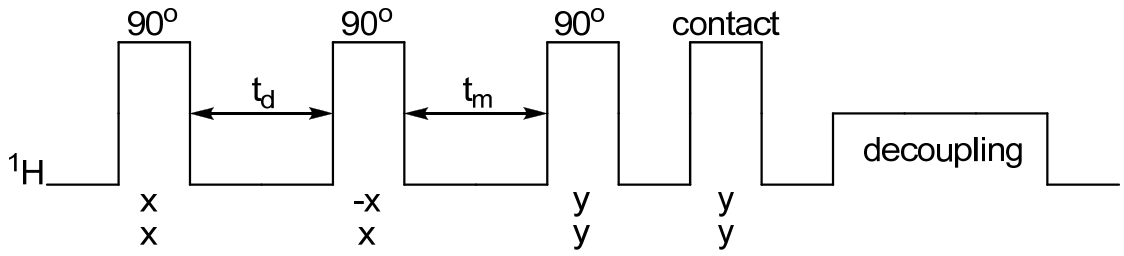

Figure 3.33 *Modified Goldman-Shen pulse sequence modified for CP-MAS ^{13}C NMR.*

Newman suggested using two separate experiments where the peak intensities, I (x & -x phase) and I' (x & x phase), are recorded for each polymer component. When the difference I-I' is plotted then the effects of T_{1H} relaxation partially cancel whereas the spin diffusion effects act additively. Again the value of T_m occurs at the inflexion point of in this case the plot $[I(t_m)-I'(t_m)] / [I(\infty)+I'(\infty)]$ versus $t^{½}$.

Using this approach and applying it to the PE experiments, a plot is derived which is shown in Figure 3.34.

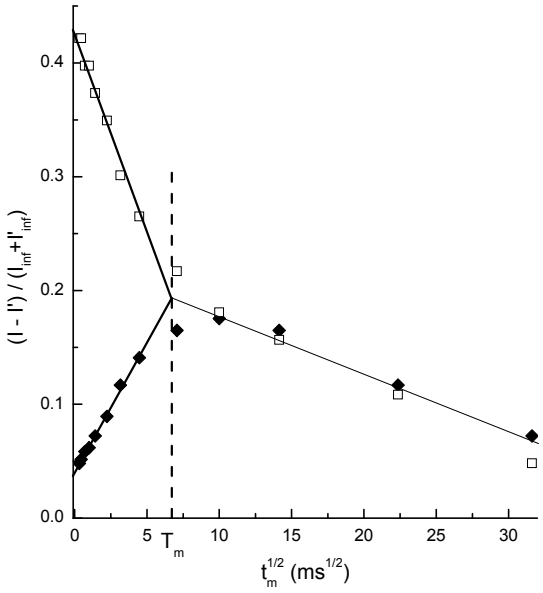

Figure 3.34 *Newman-modified Goldman-Shen spin diffusion experiment on PE (closed symbol = crystalline phase, open symbol = amorphous phase).*

The intercept of the initial signal decay of the amorphous PE with the rise in signal from the crystalline PE, this occurs at 6.4 $ms^{1/2}$ or 41 ms. By applying Equation 3.9a, a value for the amorphous domain size of 6.6 nm was obtained.

Nutation Perturbation (microsecond time-scale, T_{2H} based selection)

At longer proton pulse lengths T_{2H} relaxation during nutation can be used as a selection tool to differentiate phases. The optimal proton pulse length is determined by a nutation experiment to ascertain the best possible T_{2H} based discrimination while maintaining a reasonable signal to noise ratio. In this case however the pulse is such that the magnetisation ends in the Z-axis after nutation and this is followed by a mixing time (t_m) to allow spin diffusion, followed by the usual standard cross polarisation sequence (Figure 3.35).

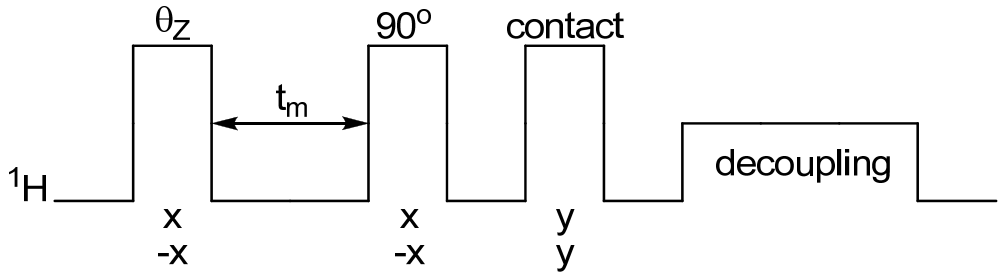

Figure 3.35 *Nutation T_{2H} perturbation and spin diffusion measurement pulse sequence.*

This pulse sequence is very simple, and has the advantage of not being sensitive to pulse imperfections as the exact proton tip angle required is determined experimentally. The Goldman-Shen method, in which multiple 90° pulses are required, is more prone to pulse imperfections caused by difficulties with setting exact pulse times or hardware limitations in length of delays between pulses.

It can be seen, that for PE at shorter times (< 15 µs), the scaled relative peak ratios remain synchronous. However, as the proton tip angle increases, the crystalline and amorphous peak ratios diverge (refer to Figure 3.15).

In the nutation perturbation experiment a proton preparation time of *ca.* 35 µs (T_{atten}) (refer to Figure 3.15) is equivalent to approximately a 450° rotation as experienced by the amorphous phase. This 450° pulse decreases the signal intensity approximately 3.75 fold for the amorphous peak and approximately 18.75 fold for the crystalline peak relative to standard ^{13}C CP-MAS experiment. The consequence of this was about a 5-fold discrimination between the amorphous and crystalline phases compared with a proton preparation pulse of *ca.* 7 µs. In this case, the first pulse was set to achieve a 360° pulse as experienced by the amorphous phase, followed by a mixing time delay and then a 90° read pulse for a total of an effective 450° pulse. Spin diffusion during the mixing time then

diminishes the magnetic perturbation. At 0 ms mixing time, the perturbation could be seen as the amorphous peak dominates the NMR spectrum. As the mixing time increased, the crystalline PE peak emerged, and after approximately 100 ms the spectrum appeared similar to that of a standard CP-MAS spectrum of PE (Figure 3.36).

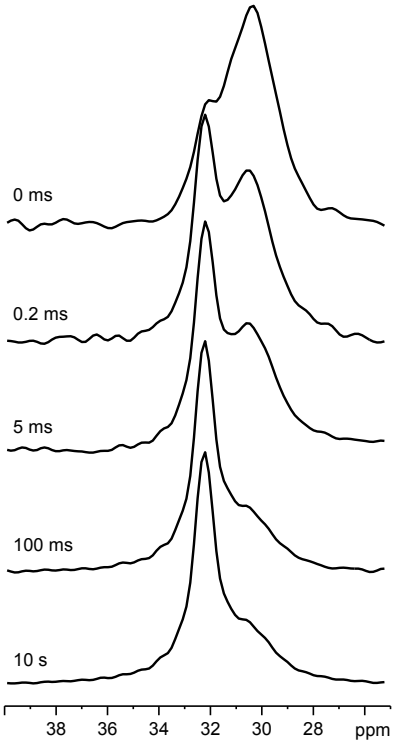

Figure 3.36 *PE* spin diffusion experiment after T_{2H} selection diminished the magnetic perturbation with increasing mixing time (normalised, left peak = crystalline phase, right peak = amorphous phase).

The time obtained for complete mixing was 5.6 $ms^{1/2}$ or 31 ms, giving a domain size of around 5.7 nm (refer to Equation 3.9a) when using a plot of I / I_{inf} versus the square root of time (Figure 3.37).

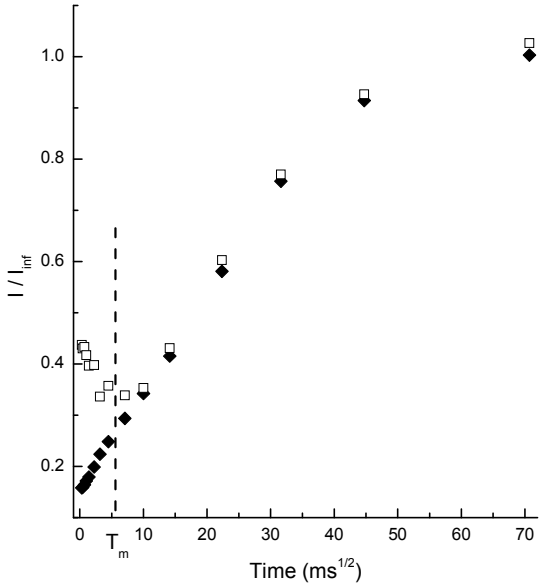

Figure 3.37 *Nutation based T_{2H} perturbation and proton spin diffusion of PE (closed symbol = crystalline phase, open symbol = amorphous phase).*

Alternatively, plotting the intensity of the crystalline phase signal (I_x) versus the intensity of amorphous signal (I_a) gives a mixing time of 52 ms or a domain size of 7.4 nm (Figure 3.38).

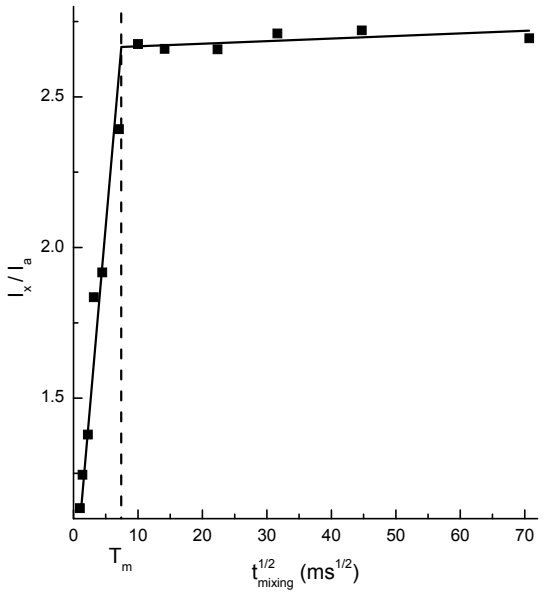

Figure 3.38 *Nutation-diffusion based T_{2H} perturbation and proton spin diffusion of PE.*

The methods presented above for the determination of the mixing times are very dependent on the scatter of the data and the difficulty in determining the intercept point. To address this issue, an alternative method that would involve the minimum of data handling and provide a less-subjective value for the mixing time was investigated. The method of data handling was to adopt the simple I / I_{inf}, reflecting the efficiency of the attenuation of one phase over the other. Rather than focusing on the depleted phase (i.e. the amorphous phase) and its replenishment from the crystalline phase, a two-phase diffusion model taking into account T_{1H} effects was developed. As part of this work, each signal intensity data point in time was modelled iteratively with the effects of T_{1H} relaxation and either the replenishment (PE crystalline phase, Equation 3.12a) or the depletion (PE amorphous phase, Equation 3.12b) of magnetisation due to spin diffusion with respect to the previous signal intensity for a succession of time steps labelled Δt.

$$I_n^x / I_{inf}^x = (I_{n-1}^x (1 - \Delta t / T_{1H}^x) + \Delta t (I_{n-1}^a - I_{n-1}^x) / T_m) + 1 \qquad 3.12a$$

$$I_n^a / I_{inf}^a = (I_{n-1}^a (1 - \Delta t / T_{1H}^a) + \Delta t (I_{n-1}^x - I_{n-1}^a) / T_m) + 1 \qquad 3.12b$$

Here I_n and I_{n-1} are the signal intensity at the current and previous time interval (Δt) respectively, where n is the n^{th} time increment. x and a are the crystalline and amorphous phase respectively, and T_m is the time to counteract the magnetisation imbalance.

By the use of Equations 3.12a and 3.12b the mixing time could be derived by using either experimentally determined T_{1H} values (as used in this case) or estimates at T_{1H} values followed by the adjustment of the T_m parameter to produce a fit with experimental spin-diffusion data (Figure 3.39).

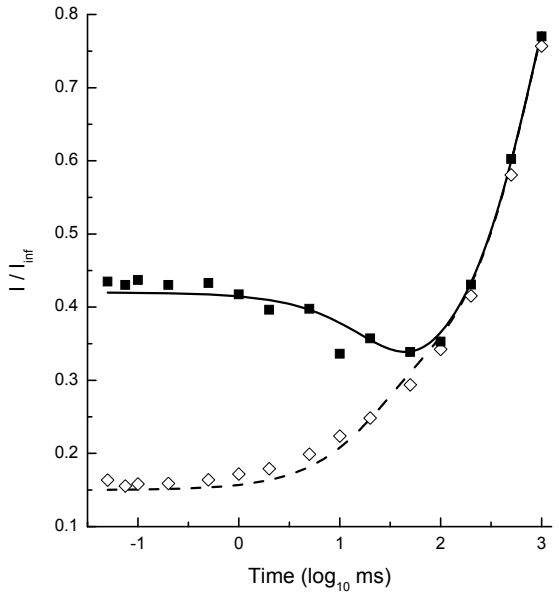

Figure 3.39 *Modelling of spin diffusion data to obtain a mixing time for PE (closed symbol = crystalline phase, open symbol = amorphous phase, solid line = crystalline phase model, dashed line = amorphous phase model). The curves are generated by simulation using the iterative relationship shown in Equations 3.11a & 3.11b.*

A reasonable fit was found at a T_m time of 45 ms, giving a domain size of 6.9 nm (refer to Equation 3.9a). This value is in good agreement with values obtained using earlier presented methods (Table 3.2).

A common method for the perturbation of magnetisation based on T_2(H) relaxation, prior to a spin diffusion experiment, is the ^{1}H dipolar filter (Clauss et al. 1993). However, due to hardware limitations not allowing appropriate pulse spacings/times that were required, this method failed to produce satisfactory spectra.

Table 3.2 *Summary mixing times and domain sizes for PE obtained using different pulse sequences and plots.*

Pulse Sequence	*Selection method*	*Y axis (X axis = $t^{1/2}$)*	*Mixing time, T_m (ms)*	*Domain size (nm)*
Spinlocking	$T_{1\rho H}$	I / I_{inf}	28	5.4
Goldman-Shen	T_{2H}	I / I_{inf}	38	6.4
Goldman-Shen	T_{2H}	I_x / I_a	72	8.7
Goldman-Shen	T_{2H}	$(I_{inf} - I_a) / (I_x^{inf} - I_x) (I_x^{inf} / I_a^{inf})$	40	6.5
Modified GS	T_{2H}	$(I - I') / (I_{inf} + I'_{inf})$	41	6.6
Nutation-diffusion	T_{2H}	I / I_{inf}	31	5.7
Nutation-diffusion	T_{2H}	I_x / I_a	52	7.4
Nutation-diffusion	T_{2H}	modelling	45	6.9
		Average (CoV)	43 (0.3)	6.7 (0.2)

GS = Goldman-Shen, I = signal intensity, x = crystalline phase, a = amorphous phase, inf = intensity at 'infinite' time, CoV = coefficient of variation ($T_{1\rho H}$ = domain size based on initial dephasing of the PE amorphous phase, T_{2H} = domain size based on initial dephasing of the PE crystalline phase).

3.5 Conclusions

Polyethylene proved a good model solid material system with which to investigate the various methods of determining NMR relaxation parameters and methods of measuring spin-diffusion mixing times.

All the methods that were investigated for creating a magnetisation imbalance between the crystalline and amorphous phases in PE, and then measuring spin-diffusion between the phases gave reasonable domain size with respect to each other and with literature values. However, it was found that methods involving the fitting of multiple lines to data where the linear regions were not lucid made reproducibility problematic. A less-subjective method involving the modelling of the spin-diffusion process was developed from which mixing times overcame some of the fitting problems of other methods.

The nutation method of creating a magnetisation imbalance for spin-diffusion showed particular promise, since the pulse sequence was simple (and therefore not sensitive to spectrometer performance) and the time required for establishing perturbation was << T_m. This method was carried forward to the NMR studies of wood (next Chapter).

3.6 References

Abragam, A. The principles of nuclear magnetism. Oxford University Press, London, 1970

Alla, M., Lippmaa, E. (1976) High resolution broad line ^{13}C and relaxation in solid norbornadiene. Chemical Physics Letters. 37(2):260-264

Barnaal, D., Lowe, I.J. (1963) Effects of rotating magnetic fields on free-induction decay shapes. Physical Review Letters. 11:258-260

Bruker. (2009) Almanac 2009:38

Chen, Q., Schmidt-Rohr, K. (2006) Measurement of the local ^{1}H spin-diffusion coefficient in polymers. Solid State Nuclear Magnetic Resonance. 29:142-152

Cheung, T.T.P. (1982) Modulation of proton NMR free induction decay by spin diffusion. Journal of Chemical Physics. 76(3):1248-1254

Cheung, T.T.P., Gerstein, B.C. (1981) ^{1}H nuclear magnetic resonance studies of domain structures in polymers. Journal of Applied Physics. 52(9):5517-5528

Cheung, T.T.P., Gerstein, B.C., Ryan, L.M., Taylor, R.E., Dybowski, D.R. (1980) High resolution ^{1}H solid state NMR studies of polyethyleneterephthalate. Journal of Chemical Physics. 73(12):6059-6067

Clauss, J., Schmidt-Rohr, K., Spiess, H.W. (1993) Determination of domain sizes in heterogeneous polymers by solid-state NMR. Acta Polymerica. 44:1-17

Demco, D.E., Johansson, A., Tegenfeldt, J. (1995) Proton spin diffusion for spatial heterogeneity and morphology investigations of polymers. Solid State Magnetic Resoance. 4:13-38

Duer, M.J. Introduction to solid-state NMR spectroscopy. Blackwell Publishing Ltd, Cornwall, Great Britain, 349, 2004

Gaur, U., Wunderlich, B. (1980) The glass transition temperature of polyethylene. Macromolecules. 13:445-446

Goldburg, W.I., Lee, M. (1963) Nuclear magnetic resonance line narrowing by rotating rf field. Physical Review Letters. 11:255-258

Goldman, M., Shen, L. (1965) Spin-spin relaxation in LaF_3. Physical Review. 144:321-331

Jubb, A.H. (1975) Primary Petrochemicals, I: Alkanes, Alkenes and Alkynes. In: Basic Organic Chemistry: Part 5, Industrial Products. John Wiley & Sons, London, New York, Syndey, Toronto.

Kitamaru, R., Horii, F., Murayama, K. (1986) Phase structure of lamellar crystalline polyethylene by solid-state high-resolution carbon-13 NMR detection of the crystalline-amorphous interphase. Macromolecules. 19:636-643

Levitt, M.H. Spin dynamics: Basics of nuclear magnetic resonance. John Wiley & Sons, Ltd, West Sussex, England, 2002

McBrierty, V.J., Douglass, D.C. (1980) Nuclear magnetic resonance of solid polymers. Physics Reports. 63(2):61-147

Mowery, D.M., Harris, D.J., Schmidt-Rohr, K. (2006) Characterization of a major fraction of disordered all-trans chains in cold drawn high-density polyethylene by solid-state NMR. Macromolecules. 39:2856-2865

Newman, R.H. (1987) Effects of finite preparation-pulse power on the carbon-13 cross-polarization NMR spectra of heterogenous samples. Journal of Magnetic Resonance. 72:337-340

Newman, R.H. (1991) Proton spin diffusion monitered by ^{13}C NMR. Chemical Physics Letters. 180(4):301-304

Packer, K.J., Pope, J.M., Yeung, R.R., Cudby, M.E.A. (1984) The effects of morphology on ^{1}H NMR spectra and relaxation in semicrystalline polyolefins. Journal of Polymer Science: Polymer Physics Edition. 22(4):589-616

Popescu-Pogrion, N., Tirnovan, M. (1998) Study by transmission electron microscopy and electron diffraction of
thin polyethylene films. Thin Solid Films. 317:232-234

Schmidt-Rohr, K., Clauss, J., Blumich, B., Spiess, H.W. (1990) Miscibility of polymer blends investigated by ^{1}H spin diffusion and ^{13}C NMR detection. Magnetic Resonance in Chemistry. 28:S3-S9

Solomons, T.W.G. Organic chemistry. John Wiley & Sons, Canada, 1186, 1988

Tang, H., Belton, P.S., Ng, A., Ryden, P. (1999) ^{13}C MAS NMR studies of the effects of hydration on the cell walls of potatoes and Chinese water chestnuts. Journal of Agricultural and Food Chemistry. 47:510-517

Uehara, H., Aoike, T., Yamanobe, T., Komoto, T. (2002) Solid-state ^{1}H NMR relaxation analysis of ultrahigh molecular weight polyethylene reactor powder. Macromolecules. 35:2640-2647

Uehara, H., Uehara, A., Kakiage, M., Takahashi, H., Murakami, S., Yamanobe, T., Komoto, T. (2007) Solid-state characterization of polyethylene reactor powers and their structural changes upon annealing. Polymer. 48:4547-4557

VanderHart, D.L., McFadden, G.B. (1996) Some perspectives on the interpretation of proton NMR spin diffusion data in terms of polymer morphologies. Solid State Nuclear Magnetic Resonance. 7:45-66

VanderHart, D.L., Perez, E. (1986) A ^{13}C method for determining the partitioning of end groups and side branches between crystalline and noncrystalline regions in polyethylene. Macromolecules. 19:1902-1909

Zhang, S., Mehring, M. (1989) A modified Goldman-Shen NMR pulse sequence. Chemical Physics Letters. 160:644-646

Zumbulyadis, N. (1983) Selective carbon excitation and the detection of spatial heterogeneity in cross-polarization magic-angle-spinning NMR. Journal of Magnetic Resonance. 53:486-494

4 Modelling proton spin diffusion in the secondary cell wall

4.1 Introduction

The previous chapter presented data and discussed the use of spin diffusion to estimate the spatial arrangement between two components in the model PE system. Choosing an appropriate spin diffusion coefficient is critically important to enable understanding of the nanostructure of the material under study. In cases where the material can be easily analysed by methods such as transmission electron microscopy (TEM) or small angle X-ray scattering (SAXS), the value of the spin diffusion coefficient can be calibrated. The structure of the wood cell wall chemically-heterogeneous components are not so easily examined and quantified as in the PE case, leading to a situation where any value of the spin diffusion coefficient estimated must be obtained by comparison with known values of materials that have similar properties. This chapter will discuss the assumptions made and the method used to arrive at a value of the spin diffusion coefficient for wood cell wall components. This spin diffusion coefficient and dimensions of the cellulose microfibril (Chapter 2) will then be used to investigate the hypothesis of the structural nature of water in the green wood cell wall, and its location at the cellulose microfibril surface in juxtaposition with the hemicellulose/lignin matrix surrounding it.

The "trick" used in this work to reveal the presence of interfacial water was to exchange all the molecular water with deuterated water (Appendix E). D_2O provides a natural barrier to spin diffusion because the magnetogyric ratio of ^2H is 1/7 of ^1H. H_2O can potentially permit magnetisation transfer across an interfacial water layer because of rapid molecular self-diffusion, hence the use of D_2O in this case.

4.2 Estimation of spin diffusion coefficients

The major problem with the application of NMR to measurement of domain sizes is the uncertainty in the determination of the spin diffusion coefficients. The spin diffusion coefficient, D, is related to the T_{2H} of materials (Cheung 1981), so it follows that two different materials that have differing T_{2H} values would also have differing spin diffusion coefficients. One approach taken in this situation is to use Equation 4.1, where $(r_{HH})^2$ is the square of the shortest distance between protons in the crystalline phase and T_{2H}^f is the fastest T_{2H} relaxing component (Cheung 1981).

$$D \approx 0.13(r_{HH})^2 / T_{2H}^{f} \qquad 4.1$$

An assumption is made that that the spin diffusion coefficient of the two phases can be approximated as being equal. However, this does highlight the uncertainty inherent in values obtained from spin diffusion experiments for determining supra-molecular dimensions. The determination of spin diffusion coefficients for diverse materials has been an on-going area of research, and unfortunately is not as straightforward as Equation 4.1 would indicate. Recently, it has been shown that the value of *D* obtained is influenced by factors such things as MAS spinning speed. At spinning speeds of >30 kHz, a reduction in *D* of as much as 90% was observed and even at *ca.* 10 kHz, errors in domain size may be as high as 50% with respect to *D* determined using static experiments (Jia et al. 2008). Cognisant of these inherent difficulties, the NMR experiments carried out in this thesis were carried out at spinning speeds of 5 kHz (i.e. much less than 30 kHz).

Further complications arise from the observation that spin diffusion coefficients are also dependant on the length scale of the diffusion (Chen and Schmidt-Rohr 2006). Spin diffusion coefficients calculated using a local short-range spin diffusion (0.4 - 0.8 nm) were found to be lower than those derived from more traditional methods (Chen and Schmidt-Rohr 2006). For example, *D* for polyethylene has reported values of 0.83 nm^2ms^{-1} (Cheung 1981) versus 0.3 - 0.5 nm^2ms^{-1} (Chen and Schmidt-Rohr 2006), for polystyrene 0.53 nm^2ms^{-1} (VanderHart and McFadden 1996) versus 0.2 - 0.3 nm^2ms^{-1} (Chen and Schmidt-Rohr 2006), and for polypropylene 0.68 nm^2ms^{-1} (Cheung 1981) versus 0.3 - 0.5 nm^2ms^{-1} (Chen and Schmidt-Rohr 2006). It was observed that as the length scale of the spin diffusion was increased, the spin diffusion rate also increased approaching a value of *ca.* 0.8 nm^2ms^{-1} for polyethylene on the 10 nm scale (Clauss et al. 1993). This indicates that the size of the polymer phase influences the apparent diffusion rate with morphologies of less than 10 nm resulting in lower calculated spin diffusion rates, again highlighting the difficulty of assigning a specific value of *D* to any homopolymer system, let alone to a molecularly-heterogeneous, anisotropic supramolecular assembly such as a wood cell wall.

Studies of copolymers, such as poly(styrene) – poly(methyl methacrylate) (PS-PMMA) systems using NMR spin diffusion, TEM and SAXS have yielded some of the best estimates of a spin diffusion coefficient of a polymer to date by cross-calibration across the instrumental methods (Clauss et al. 1993). Using the relationship given in Equations 4.2a and 4.2b, the proton spin diffusion rate for the rigid (D_R) and mobile (D_M) phases can be estimated for a polymer using wideline ^{1}H NMR.

$$D_R = 0.13\ \Delta\nu_{1/2}\ (r_{HH})^2 \qquad 4.2a$$

$$D_M = 0.17\ (\alpha\Delta\nu_{1/2})^{1/2}\ (r_{HH})^2 \qquad 4.2b$$

In these equations, $\Delta\nu_{1/2}$ is the full width at half height of the proton line, $(r_{HH})^2$ is the square of the shortest distance between protons and α is the cut-off parameter for the Lorentzian line (Clauss et al. 1993; Voda et al. 2006).

It is also fundamentally important that studies of spin diffusion between polymer systems be conducted under identical strictly-controlled temperature regimes for the coefficients to be meaningful and applicable for deriving information on polymer nanostructure, since an increase molecular motions (e.g. as a result of increase in temperature) cause spin diffusion coefficients to decrease. This has been observed in polybutadiene with the calculated *D* decreasing from 0.6 nm^2ms^{-1} at 10 °C to 0.2 nm^2ms^{-1} at 70 °C (Spiegel et al. 1993). .

For the purposes of this work, a value for *D* of 0.8 ± 0.2 nm^2ms^{-1} for a rigid organic polymer (PS-PMMA), as calibrated against the results from TEM and SAXS (Clauss et al. 1993), was used for determining an initial estimate of spin diffusion coefficients in wood cell wall components.

Using the calibrated value of *D* of *ca.* 0.8 nm^2ms^{-1} for PS-PMMA, it was possible to estimate the spin diffusion coefficient of other rigid materials by using a ratio of the cube root of proton densities for each polymer (Equation 4.3) (VanderHart and McFadden 1996). This is derived from the understanding that spin diffusion is a function of dipolar couplings and that dipolar coupling strength is inversely proportional to the cube of the distance between atoms and with proton density (ρ^H) assumed to have a uniform distribution.

$$(D_{unk} / D_{ref}) = (\rho_{unk}^{H} / \rho_{ref}^{H})^{1/3} \qquad 4.3$$

A value of 0.62 nm^2ms^{-1} for alkanes (Douglas and Jones 1966) has also been used a reference value (Havens and Vanderhart 1985; Kimura et al. 1992). However, the alkane which was used for this determination was not clearly defined, and it would appear that using this parameter as a reference value resulted in an underestimation of values of *D* for other polymers when measured under identical conditions (VanderHart and McFadden 1996).

For a two-phase system, the effective spin diffusion coefficient can be estimated using the geometric mean of the individual spin diffusion coefficients (Equation 4.4) (Mellinger et al. 1999; Mellinger et al. 1999; Sun et al. 2005).

$$D_{eff}^{1/2} = (D_A D_B)^{1/2} / (D_A^{1/2} + D_B^{1/2}) \qquad 4.4$$

In this equation, D_A and D_B are the spin diffusion coefficients of the magnetisation source and sink respectively.

A theoretical value of *D* for cellulose (the cellulose source and specimen moisture content were not disclosed) using Equation 4.3 and based on a value of D calculated for alkanes of 0.62 nm^2ms^{-1} resulted in a value of 0.55 nm^2ms^{-1} (Vanderhart et al. 1994). As such, this value of *D* for cellulose can be regarded as a lower limit. More specifically for wood cell walls, the value of *D* for the cellulose component was calculated to be 0.97 nm^2ms^{-1} using Equation 4.1 where T_{2H} was calculated to be 8.9 μs based on pure cellulose and the average ^1H-^1H distance was taken to be 0.26 nm based on a cubic lattice (Newman 1992).

Much lower values of *D* have been calculated for lignin (0.06 nm^2ms^{-1}) and interior cellulose (0.1 nm^2ms^{-1}) of wood cell walls compared with that of pure cellulose (Altaner et al. 2006). The explanation given for these low values was that spin diffusion was more rapid in the direction of the cellulose polymer than that perpendicular to the cellulose chain due to spin flip-flops having to cross hydrogen-bonded interfaces for spin diffusion perpendicular to chains to occur (Altaner et al. 2006). These spin diffusion values presented by Altaner for wood cell wall components are considered unusual when compared to literature *D* values for many rigid polymers.

Given the complex heterogeneous nature of wood cell walls, Equations 4.3 and 4.4 will be used to estimate a value of the spin diffusion rate (*D*).

4.3 Summary of reported spin diffusion coefficients for selected polymers

Wood cell wall polymers are all in a glassy state at room temperature (< T_g for cellulose, hemicellulose, and lignin) (Irvine 1984) so the presence of a true mobile phase needs not to be considered when determining spin diffusion coefficients for the magnetisation source and sink (Mellinger et al. 1999).

To estimate the spin diffusion coefficient a reference value is required, presented as Table 4.1 are values of *D* calibrated against SAXS and/or TEM from literature sources.

Table 4.1 *Values of D calibrated against SAXS or TEM.*

Polymer	*D (nm^2ms^{-1})*	*Domain size (NMR, nm)*	*Domain size (SAXS/TEM, nm)*	*Reference*
PEO	0.1 ± 0.02	–	17 (S)	(Wilhelm et al. 1994)
PEO-PPO-PEO	0.14	14.4	14.7 (S)	(Sun et al. 2005)
CELL/P2VPy	0.52	7.7-10.4	13.6 (S)	(Vanderhart et al. 1994)
CELL/PAN	0.52	15.9-20.5	18.7 (S)	
PS-PMMA*	0.8 ± 0.2	7-13	11 (S)	(Clauss et al. 1993)
	0.8 ± 0.2	16-32	33 (S)	
	0.8 ± 0.2	52-82	40-60 (T)	
	0.8 ± 0.2	50-110	75-125 (T)	

*Increasing domain sizes are for increasing molecular weights of the components.

PEO = poly(ethylene oxide)

PEO-PPO-PEO = poly(ethylene oxide)-*block*-poly(propylene oxide)-*block*-poly(ethylene oxide)

CELL/P2VPy = blend of cellulose and poly(4-vinylpyridine)

CELL/PAN = blend of cellulose and poly(acrylonitrile)

PS-PMMA = poly(styrene)-poly(methyl methacrylate)

Cellulose, hemicellulose, and lignin are all above their respective T_g values at room temperature, so of the calibrated values from Table 4.1, only those of CELL/P2VPy, CELL/PAN, and PS-PMMA, also above their respective T_g values at room temperature, are appropriate to consider for use as a reference (D_{ref}) value. Of these, the spin diffusion coefficient of PS-PMMA gave consistent values over a large range of domain sizes, and therefore this value, 0.8 nm^2ms^{-1}, was adopted as a reference value for D_{ref}.

4.4 Estimation of the cellulose proton spin diffusion mixing time for Pinus radiata never-dried latewood

An estimation of a spin diffusion coefficient can be derived by rearranging Equation 4.3 in terms of D_{unk} (= D_{wood}) (Equation 4.5) and using data from Table 4.2.

$$D_{unk} = D_{ref} (\rho_{unk}^{H} / \rho_{ref}^{H})^{1/3} \qquad 4.5$$

Table 4.2 *Average physical constants for wood chemical components.*

Component	*Density (g cm^{-3})*	*Molecular Weight (g mol^{-1})*	*Proton Mass Fraction*	*Proton Density (g cm^{-3})*
Cellulose Iα[a]	1.582[d]	162.14	0.06	0.09
Cellulose Iβ[a]	1.599[d]	162.14	0.06	0.10
Hemicellulose[b]	1.666[e]	162.14	0.06	0.10
Lignin[c]	1.347[e]	196.39	0.06	0.08

a = $C_6H_{10}O_5$, b = mostly $C_6H_{10}O_5$, c = $C_9H_{9.0}O_{3.4}(OCH_3)_{0.8}$ (Ferraz and Duran 1995), d (Sugiyama et al. 1991), e (Passialis 1998).

An average proton density for cellulose (0.10 g cm^{-3}) and the matrix (hemicellulose + lignin, 0.09 g cm^{-3}) were used for calculating an estimate for D_{wood}. As the wood specimens used had their cell walls fully-hydrated with D_2O, the proton density in the matrix was multiplied by a factor of 0.5 to account for the increased inter-proton distance (i.e. equal mass of D_2O to matrix). The PS-PMMA value of 0.8 nm^2ms^{-1} (D_{ref}) (Clauss et al. 1993) was used as a reference value. D_{wood} was then estimated using Equation 4.5 to be 0.83 nm^2ms^{-1} for cellulose and 0.66 nm^2ms^{-1} for the matrix. The effective spin diffusion coefficient was then calculated using Equation 4.4 to give a geometric mean of 0.74 nm^2ms^{-1}.

4.5 Evidence for the presence of a water barrier between cellulose microfibril and the cell wall matrix in never-dried wood

Assuming a model where a cylinder of matrix (swollen with water at fibre saturation and above) surrounds a rod of a cellulose microfibril then the spin diffusion perpendicular to the cellulose polymer axis can be assumed to be rod-like (Figure 4.1). Using Equation 3.10a (Chapter 3), the maximum mean square distance required to destroy the magnetisation imbalance can be estimated.

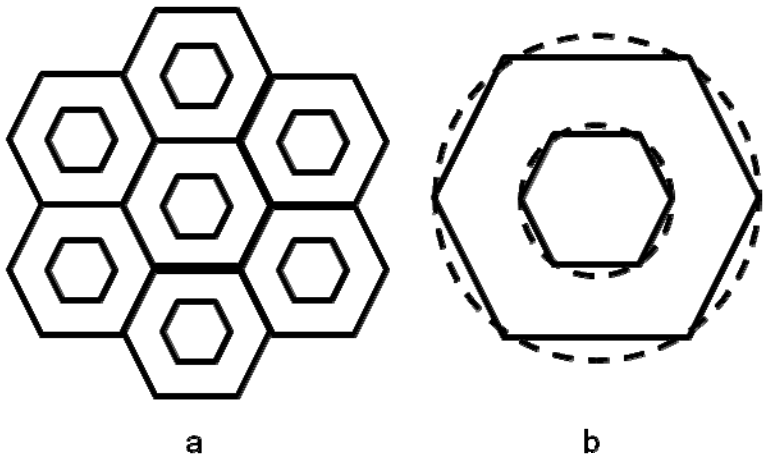

Figure 4.1 *(a) microfibril structure with cellulose (grey) in a matrix of hemicellulose and lignin (white) and (b) a single microfibril and surrounding swollen matrix approximated as concentric circles (rod of cellulose within a cylinder of matrix).*

Pinus woods have a reported typical cellulose microfibril diameter of 3 - 4 nm (Nomura and Yamada 1972; Takeda et al. 1981; Andersson et al. 2005). In Chapter 2, it was found the microfibril mean size in specimens of radiata pine latewood to be smaller, at 2.54 nm. This value will be used below. The total size of the cellulose and matrix is less well defined and must be estimated.

A model constructed (Figure 4.2) in which the length of the rod/cylinder L is a constant, the value of R_c is the radius of the cellulose microfibril (1.27 nm), and the radius R represent the total radius of cellulose plus the surrounding cell wall matrix.

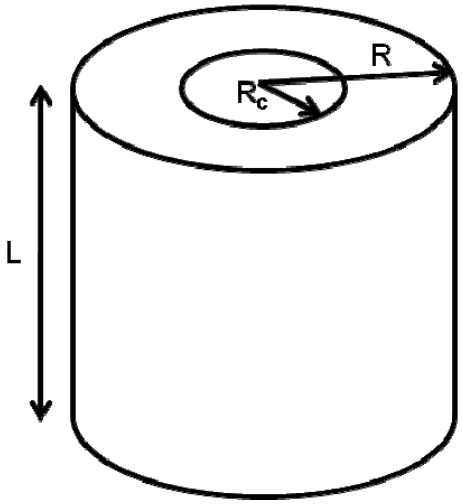

Figure 4.2 *Assumed model of a cellulose microfibril (rod) surrounded by matrix (cylinder).*

The total volume is then the sum of the volume of cellulose, hemicellulose, and any added D_2O (Equation 4.7a). This then can be expressed in terms of weight fractions by using the densities of the components (Equation 4.7b) allowing the volume ratio of cellulose to be calculated (Equation 4.7c). As the rod/cylinder is assumed to have a constant length, then the ratio of the radius of cellulose to the total radius can be found by taking the square root of the volume ratio (Equation 4.7d). Knowing the radius of the cellulose microfibril (established in Chapter 2) allows then an estimation of the total radius.

$$V_{total} = V_{cellulose} + V_{matrix} + V_{D2O} \qquad 4.7a$$

$$V_{total} = (w_{cellulose} / \rho_{cellulose}) + (w_{matrix} / \rho_{matrix}) + (w_{D2O} / \rho_{D2O}) \qquad 4.7b$$

$$(V_{cellulose} / V_{total}) = (w_{cellulose} / \rho_{cellulose}) / V_{total} \qquad 4.7c$$

$$(r_{cellulose} / r_{total}) = (V_{cellulose} / V_{total})^{1/2} \qquad 4.7d$$

The above relationships can be considered under two situations, first when the wood cell wall is fully saturated with H_2O (*i.e.* no D_2O is added), and the second when the wood cell walls are saturated with D_2O, having exchanged all the H_2O. An average density of 1.591 g cm^{-3} for cellulose, 1.517 g cm^{-3} for the matrix has been assumed, and a cellulose crystal radius of 1.27 nm.

In the case of dry wood cell walls where, $w_{cellulose}$ = 0.4 and w_{matrix} = 0.6 then $V_{cellulose}/V_{total}$ is 0.39, giving a total radius of 3.3 nm (1.27 nm / 0.39). In the case of

D_2O-saturated wood cells walls where, $w_{cellulose}$ = 0.26, w_{matrix} = 0.37, and w_{D2O} = 0.37 then $V_{cellulose}/V_{total}$ is 0.22 giving a total radius of 5.8 nm (1.27 nm / 0.22).

By rearranging Equation 3.10a (Chapter 3) in terms of total spin diffusion mixing time (*t)*, where $<x^2>$ is mean free distance squared, *n* the dimensionality coefficient, *D* is the spin diffusion coefficient (Equation 4.8), it can then predict that the time scale for proton spin diffusion mixing between a theoretical edge of the matrix (*i.e.* outer edge of the wood cell wall) and centre of a cellulose microfibril for dry cell walls to be $T_m \approx 3.7$ ms.

$$T_m = <x^2> / n2D \qquad 4.8$$

This assumed a spin diffusion coefficient of 0.74 $nm^2\ ms^{-1}$, and direct contact between the cellulose microfibril and the matrix.

An estimate of the expected mixing time can be derived by assuming first order spin diffusion kinetics as a reasonable approximation of the signal recovery of the cellulose signal intensity after perturbation. For a 2D dimensional system, (n = 2), Equation 4.9a can be used to calculate the expected signal recovery (*R*) after perturbation (Cheung and Gerstein 1981), where $<b^2>$ is the mean square width of a radiata pine latewood cellulose microfibril.

$$R(t) = (4 / \pi^{1/2}) (Dt / <b^2>)^{1/2} \text{ for } t << (<b^2> / D) \qquad 4.9a$$

For an exponential first order spin diffusion process, signal recovery is described in Equation 4.9b.

$$R'(t) = 1 - exp[-t / T_m] \qquad 4.9b$$

The spin diffusion mixing time ($t = T_m$) can be estimated by using Equation 4.9c.

$$R'(T_m) = 1 - e^{-1} = 0.63 \qquad 4.9c$$

If *R(t)* can be approximated by *R'(t)* then *R(t) = R'(t)*, and therefore at T_m the signal recovery is calculated using Equation 4.9d.

$$R(T_m) = (4 / \pi^{1/2}) (DT_m / <b^2>)^{1/2} = 0.63 \qquad 4.9d$$

The mixing time, T_m, was therefore related to the cellulose microfibril mean square width, and the spin diffusion coefficient described in Equation 4.9e.

$$T_m = (\langle b^2 \rangle / D)\ (0.63^2\ \pi / 16) \qquad 4.9e$$

Modelling signal recovery, *R(t)* and *R'(t)*, based on Equation 4.9a and Equation 4.9b against the dimensionless $Dt/\langle b^2 \rangle$ showed that an exponential function (Equation 4.9b) could be used to approximate spin diffusion based signal recovery (Equation 4.9a), depicted in Figure 4.3.

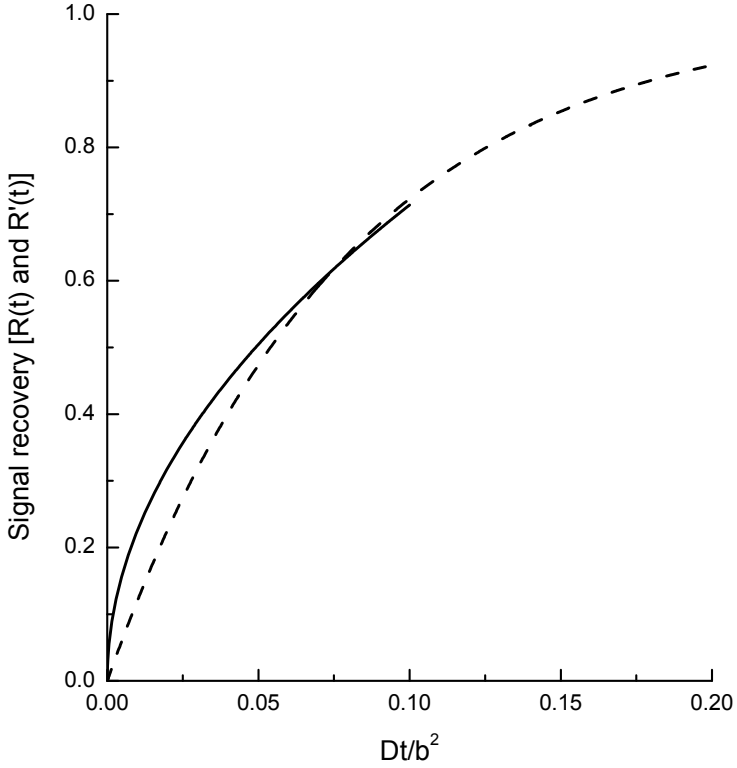

Figure 4.3 *Signal recovery of the magnetisation depleted phase as a function of Dt/b^2 (solid line = R(t), Equation 4.5a and dashed line = R'(t), Equation 4.5b).*

Accepting the approximation of an exponential function to model the spin diffusion in a 2D system, Equation 4.9e can be applied in order to estimate the mixing time required ($t = T_m$) for a cellulose crystallite with a domain size of 2.54 nm to be 0.7 ms.

The above argument assumes direct polymer to polymer contact between the cellulose microfibril and cell wall matrix (Figure 4.4a). If there is an intervening layer of H_2O molecules between the polymers, mixing will take even longer (Figure 4.4b). However, the presence of water introduces non-spin based diffusion, where a molecule of water physically moves by thermal motion and proton transfer, thereby transferring

magnetisation that may act to shorten the observed mixing time. Where the specimen was soaked in D_2O, substituting all the protons of water with deuterons, magnetisation mixing will take much longer. The presence of a D_2O barrier inhibits exchange of spin information through "flip-flop" interactions (Figure 4.4c).

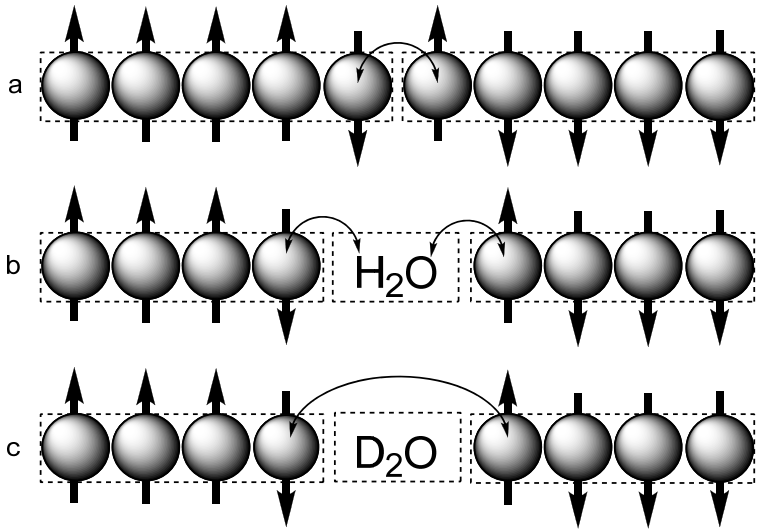

Figure 4.4 *Representations of spin systems showing spin diffusion, (a) direct contact, (b) with a water barrier, and (c) with a deuterium oxide barrier.*

The existence of a water barrier between the cellulose microfibril and the cell wall matrix polymers can therefore be tested by soaking wood in D_2O, exchanging H for D, and measuring the time constant for spin diffusion between cellulose and matrix components. A time constant T_m >> 0.7 ms would provide evidence for the existence of a water barrier.

Interpretation of the data as evidence for the presence of the water barrier separating the cellulose microfibril from the cell wall polymer matrix, the following assumptions were made:

1. Hemicellulose and lignin were considered intimately mixed together as the cell wall matrix (average density used).
2. The cellulose microfibril was considered as a rod (of 2.54 nm diameter) contained inside a cylinder of matrix.
3. At cell wall fibre saturation point, there were equal mass fractions of matrix and D_2O (ρ = 1.12 gcm^{-3}).
4. Hydration of the cell wall and its swelling (or shrinking) is only perpendicular to the direction of the long axis of the cellulose chain.
5. The mass ratio of cellulose to hemicellulose to lignin in the specimens used was 1.5:1.0:1.1 (Kininmonth and Whitehouse 1991)).
6. The spin diffusion coefficient was constant across all phases.

4.6 Models for the distribution of water in wood cell walls

Two models of the hydrated wood cell wall are now presented. In the first, the cellulose microfibril is intimately connected to the hemicellulose-lignin in the cell wall matrix, in which water molecules are distributed (Model 3, Figure 4.5a). The second model proposes the cellulose microfibril is separated from the hemicellulose-lignin matrix by a water barrier as a result of water molecules localised on the cellulose microfibril surfaces (Model 4, Figure 4.5b). Refer to pages 3 and 5 for details of Models 1 and 2 respectively.

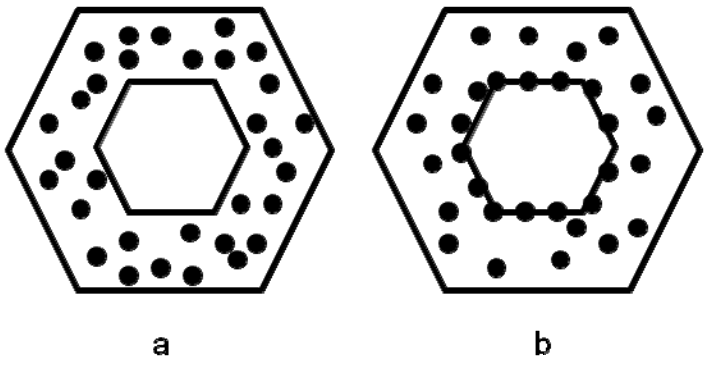

Figure 4.5 *(a) Model 3, cellulose microfibril surrounded by a water swollen hemicellulose-lignin matrix and (b) Model 4, cellulose microfibril separated by a barrier of water from the water swollen hemicellulose-lignin matrix (cellulose fibril = grey hexagon, hemicellulose-lignin matrix = white hexagon, and water molecules = black dots).*

Although the assumption was made that the average spin diffusion coefficient was a constant across the cellulose microfibril and cell wall matrix, this would not be the case when spin flip-flops need to jump a barrier created by a layer, or layers, of D_2O. In the case of a D_2O spin diffusion barrier, the incidence of flip-flop transitions will be less, owing to the increased distance between matrix protons and cellulose protons (*i.e.* weaker dipolar coupling). Because the spin diffusion rate across the D_2O barrier is unknown, it is preferred to consider the system only in terms of spin diffusion mixing times (i.e. experimentally measured results) rather than in intermolecular distances calculated from estimates of spin diffusion coefficients.

4.7 Conclusions

Two models were presented in this chapter for the distribution of water in wood cell walls. These models were tested in the following chapter by the exhaustive replacement of H_2O for D_2O and the application of NMR experiments to measure proton spin diffusion times developed in Chapter 3.

4.8 References

Altaner, C., Apperley, D.C., Jarvis, M.C. (2006) Spatial relationships between polymers in sitka spruce: Proton spin-diffusion studies. Holzforschung. 60:665-673

Andersson, S., Serimaa, R., Vaananen, T., Jamsa, S., Viitaniemi, P. (2005) X-ray scattering studies of thermally modified scots pine (*Pinus sylvestris* L.). Holzforschung. 59:422-427

Chen, Q., Schmidt-Rohr, K. (2006) Measurement of the local ^{1}H spin-diffusion coefficient in polymers. Solid State Nuclear Magnetic Resonance. 29:142-152

Cheung, T.T.P. (1981) Spin diffusion in NMR in solids. Physical Review B (Condensed Matter). 23(3):1404-1418

Cheung, T.T.P., Gerstein, B.C. (1981) ^{1}H nuclear magnetic resonance studies of domain structures in polymers. Journal of Applied Physics. 52(9):5517-5528

Clauss, J., Schmidt-Rohr, K., Spiess, H.W. (1993) Determination of domain sizes in heterogeneous polymers by solid-state NMR. Acta Polymerica. 44:1-17

Douglas, D.C., Jones, G.P. (1966) Nuclear magnetic relaxation of *n*-alkanes in the rotating frame. The Journal of Chemical Physics. 45:956-963

Ferraz, A., Duran, N. (1995) Lignin degradation during softwood decaying by ascomycete *Chrysonilia sitophila*. Biodegradation. 6:265-274

Havens, J.R., Vanderhart, D.L. (1985) Morphology of poly(ethylene terephthalate) fibers as studied by multiple-pulse ^{1}H NMR. Macromolecules. 18:1663-1676

Irvine, G.M. (1984) The glass transitions of lignin and hemicellulose and their measurement by differential thermal analysis. Tappi Journal. 67:118-121

Jia, Z., Zhang, L., Chen, Q., Hansen, E.W. (2008) Proton spin diffusion in polyethylene as a function of magic-angle spinning rate. A phenomenological approach. Journal of Physical Chemistry A. 112:1228-1233

Kimura, T., Neki, K., Tamura, N., Horii, F., Nakagawa, M., Odani, H. (1992) High-resolution solid-state ^{13}C nuclear magnetic resonance study of the combined process

of ^{1}H spin diffusion and ^{1}H spin-lattice relaxation in semicrystalline polymers. Polymer. 33:493-497

Kininmonth, J.A., Whitehouse, L.J. (1991) Properties and uses of New Zealand radiata pine. Forest Research Institute, Rotorua, New Zealand. Volume One - Wood Properties

Mellinger, F., Wilhelm, M., Spiess, H.W., Baumstark, R., Haunschild, A. (1999) Quantitative measurement of core coverage in core-shell particles by solid-state ^{1}H NMR spin-diffusion experiments. Macromolecular Chemistry and Physics. 200:719-730

Mellinger, F., Wilhelm, W., Spiess, H.W. (1999) Calibration of ^{1}H NMR spin diffusion coefficients for mobile polymers through transverse relaxation measurements. Macromolecules. 32:4686-4691

Newman, R.H. (1992) Nuclear magnetic resonance study of spatial relationships between chemical components in wood cell walls. Holzforschung. 46(3):205-210

Nomura, T., Yamada, T. (1972) Structural observation on wood and bamboo by X-ray. Wood Research. 52:1-12

Passialis, C.N. (1998) A comparison of two methods for determing the basic density of small irregular samples of old waterlogged wood. Holz als Roh und Werkstoff. 56:91-92

Spiegel, S., Schmidt-Rohr, K., Boeffel, C., Spiess, H.W. (1993) ^{1}H spin diffusion coefficients of highly mobile polymers. Polymer. 34(21):4566-4569

Sugiyama, J., Vuong, R., Chanzy, H. (1991) Electron diffraction study on the two crystalline phases occurring in native cellulose from an algal cell wall. Macromolecules. 24:4168-4175

Sun, P., Dang, Q., Li, B., Chen, T., Wang, Y., Lin, H., Jin, Q., Ding, D. (2005) Mobility, miscibility, and microdomain structure in nanostructured thermoset blends of epoxy resin and amphiphilic poly(ethylene oxide)-*block*-poly(propylene oxide)-*block*-poly(ethylene oxide) triblock copolymers characterized by solid-state NMR. Macromolecules. 38:5654-5667

Takeda, F., Koshijima, T., Okamura, K. (1981) Characterization of cellulose in compression and opposite woods of a *Pinus densiflora* tree grown under the influence of strong wind. Wood Science and Technology. 15:265-273

VanderHart, D.L., McFadden, G.B. (1996) Some perspectives on the interpretation of proton NMR spin diffusion data in terms of polymer morphologies. Solid State Nuclear Magnetic Resonance. 7:45-66

Vanderhart, D.L., St. John Manley, R., Barnes, J.D. (1994) Proton spin diffusion studies of polymer blends having modest monomer size. 2. Blends of cellulose with either poly(acrylonitrile) or poly(4-vinylpyridine). Macromolecules. 27:2826-2836

Voda, M.A., Demco, D.E., Voda, A., Schauber, T., Adler, M., Dabisch, T., Adams, A., Baias, M., Blumich, B. (2006) Morphology of thermoplastic polyurethanes by ^{1}H spin-diffusion NMR. Macromolecules. 39:4802-4810

Wilhelm, M., Lehmann, S., Jager, C., Spiess, H.W. (1994) Detection of dynamics and phase separation in polymers using 2D ^{1}H NMR in solids. Magnetic Resonance in Chemistry. 32:S3-S7

5 NMR studies of *Pinus radiata* wood nanostructure

5.1 Introduction

As shown in Chapter 3, proton spin diffusion can be detected through its influence on ^{13}C NMR signal strengths. Various methods for acquiring and processing spin diffusion data were discussed in Chapter 3. Of those, the approach of a nutation based phase selection and modelling was adopted for experiments with wood. Spin diffusion experiments on softwoods using ^{13}C NMR signals assigned to cellulose and lignin have been previously studied (Newman 1992; Altaner et al. 2006). In those experiments, proton spin diffusion took 20 ms to 25 ms to mix spin information between cellulose and the matrix components. A time constant of this magnitude is consistent with clustering of microfibrils in cellulose-rich macrofibrils, surrounded by lignin-rich domains (Salmen and Fahlen 2006; Donaldson 2007). In order to test the hypothesis of the structural role of water in cell walls, NMR equipment with greater sensitivity than that used initially by Newman (1992) was required, because the relevant glucomannan (hemicellulose) signal to use is weak. While Altaner et al. (2006) used suitable equipment for their experiments, they did not attempt to create a spin-diffusion barrier.

Chapter 4 presented models for the distribution of water in the wood cell wall along with an experimental strategy based on the use of D_2O to reveal spin diffusion barriers.

5.2 Wood specimen preparation

Specimens of *Pinus radiata* wood were collected by the method detailed in Appendix A.

Specimens for NMR spin diffusion studies were immersed in D_2O in order to exchange cell H_2O exhaustively with D_2O (refer to Appendix E). The specimens were stirred gently for 1 h, then moved to fresh D_2O and stirred for 4 h, and finally moved to fresh D_2O and stirred overnight (*ca.* 16 h). All D_2O-exchanged specimens were then cut into fragments of < 1 mm in size in a bath of D_2O followed by being immediately packed and sealed into a 4 mm solid state NMR rotor. Randomly selected samples of the fragments were examined by SEM to confirm the purity of the latewood selection (Figure 5.1 and Appendix A).

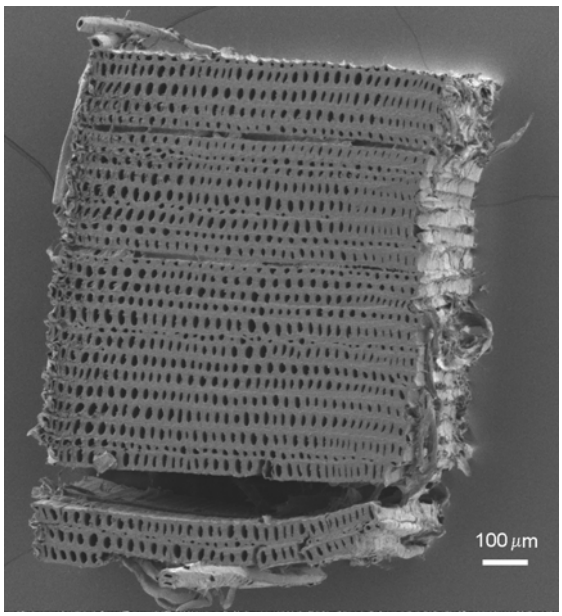

Figure 5.1 *Representative SEM picture of latewood sample used in NMR experiments (70x magnification).*

One of the specimens was subjected to four 105 °C oven-drying cycles with rewetting with D_2O between each drying cycle. After the last 105 °C drying cycle, the specimens were soaked in D_2O for 3 hours then packed and sealed in a 4 mm solid state NMR rotor.

Solid-state ^{13}C CP-MAS NMR experiments were carried out using a Bruker Avance DRX 200 operating at a ^{13}C frequency of 50.32 MHz and a ^{1}H frequency of 200.13 MHz fitted with a 4 mm MAS doubly-tuned X-H probe. Standard CP parameters used were either 200 μs or 1 ms contact time, a 5.56 μs ^{1}H preparation pulse, a recycle delay of 1.5 s (unless otherwise noted), and a ^{1}H decoupling field of *ca.* 179 kHz applied during an acquisition time of 30 ms. Specimens were immersed in H_2O or D_2O (as appropriate) before being packed in a 4 mm ZrO rotor with a Kel-F® cap. Any excess of H_2O/D_2O transferred with the sample was removed by squeezing the material in the rotor with the rotor-packing plunger.

Apodisation of the spectra was accomplished using a Gaussian function with broadening between 10 Hz and 25 Hz prior to Fourier transformation.

5.3 ^{13}C CP-MAS of *Pinus radiata*

The NMR (Figure 5.2) peaks chosen for the analysis of cellulose, hemicellulose, and lignin were the C1 of glucomannan (101.4 ppm), C4 interior of cellulose (89 ppm), and methoxyl (OCH_3) of lignin (56 ppm) (Gil and Neto 1999).

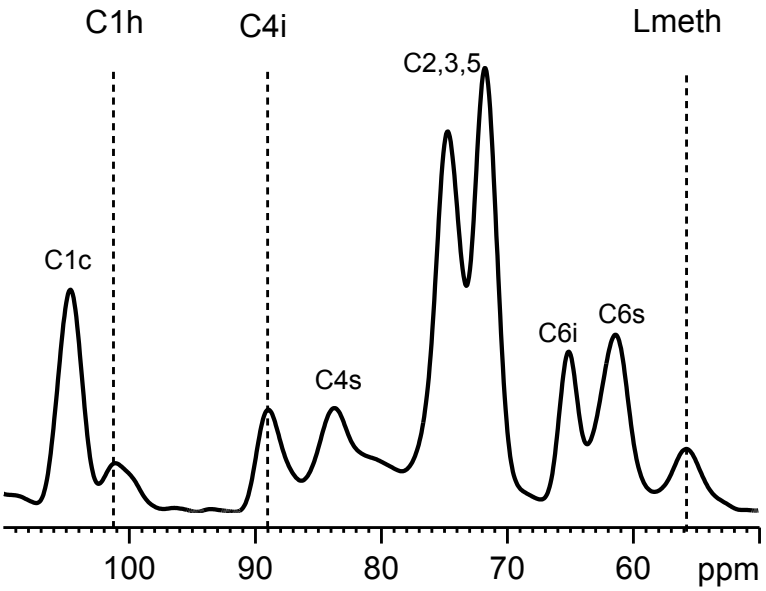

Figure 5.2 *^{13}C CP-MAS NMR spectrum of D_2O soaked never dried wood showing signals used for analysis (C1h = hemicellulose 101.4 ppm, C4i = cellulose 89 ppm, Lmeth = lignin 56 ppm).*

Intensities of the peaks were obtained by narrow range integration (± 0.5 ppm) from the centre of the peaks as defined by a reference spectrum, using a linear baseline defined by the data points at 95 ppm and 50 ppm. Each experimental set had its own reference spectrum to minimise any effects of day-to-day instrumental differences. Narrow integral ranges rather than using set peak positions were used to alleviate the problem of digitisation during Fourier transformation causing small shifts in the observed peaks maxima position, which introduced extra scatter in resulting values. The narrow integral range used also minimised the effects of nearby peaks on the intensity values of the peaks of interest.

5.4 NMR relaxation parameters

T_{1H} measurements

T_{1H} for never-dried latewood was measured using the previously described inversion-recovery CP sequence using a 6 s recycle delay based on reported T_{1H} values of wood (Newman 1992). Cellulose (89 ppm), hemicellulose (101.4 ppm), and lignin (56 ppm) T_{1H} values were found to be independent of the cell wall component chosen (Figure 5.3).

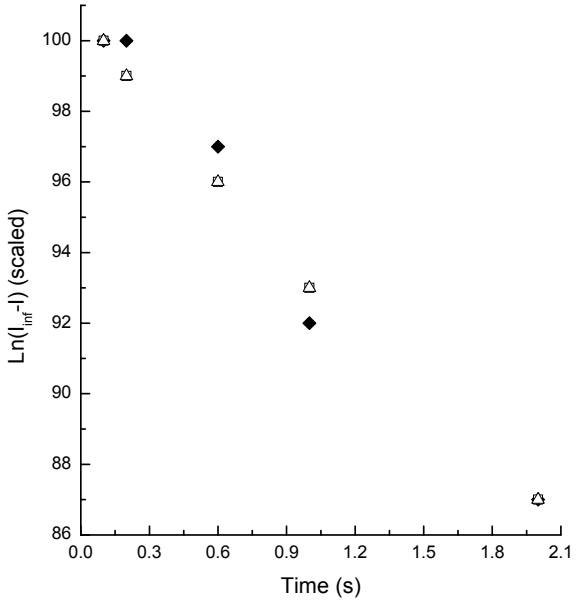

Figure 5.3 *Inversion-recovery natural log decay T_{1H} plot of cellulose (closed symbol), hemicellulose (open square), and lignin (open triangle) using a 6 s cycle delay.*

The resulting T_{1H} for cellulose, hemicellulose, and lignin was 1.01 s, 0.99 s, and 1.04 s respectively. Displaying that on the time scale of T_{1H} spin diffusion resulted in an average value, indicating that the components of the cell wall have domain sizes less than *ca.* 30 nm (Zumbulyadis 1983). Therefore, T_{1H} was unsuitable as a discriminator for spin diffusion experiments of wood cell wall components.

Although it is common practice to use a recycle delay of at least 5 times T_{1H} during an inversion-recovery T_{1H} experiment, the contact pulse resets the proton magnetisation with each transient allowing shorter recycle delays to be used. This can be seen by using a short recycle delay (1.5 s) for the inversion-recovery experiment (Figure 5.4).

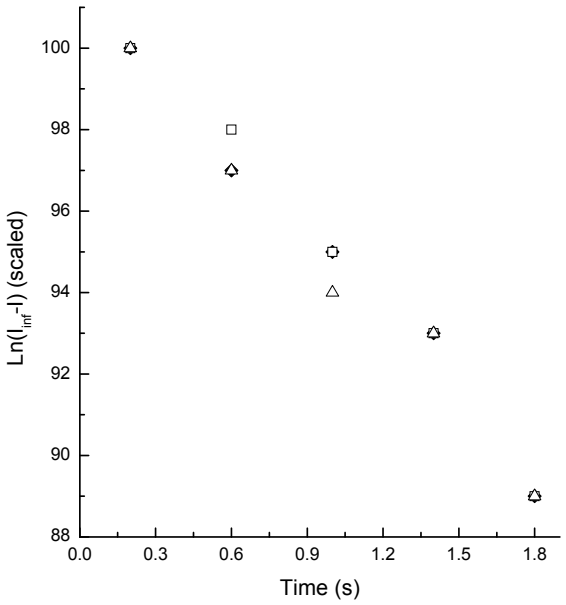

Figure 5.4 *Inversion recovery natural log decay T_1(H) plot of cellulose (closed symbol), hemicellulose (open square), and lignin (open triangle) using a 1.5 s cycle delay.*

The resulting T_{1H} for cellulose, hemicellulose, and lignin was 1.00 s, 0.98 s, and 1.02 s respectively.

By combining the two sets of results, a T_{1H} value for *Pinus radiata* latewood of 1.01 ± 0.02 s (95% C.I.) was obtained.

$T_{1\rho H}$ measurements

$T_{1\rho H}$ measurements were carried out using a variable spinlock CP sequence using the cellulose (89 ppm), hemicellulose (101.4 ppm), and lignin (56 ppm) resonances. Initially a spin-lock delay of between 1 ms and 10 ms was used resulting in $T_{1\rho H}$ values of 24.4 ms for cellulose, 14.5 ms for hemicellulose, and 9.9 ms for lignin.

Although $T_{1\rho H}$ provided some discrimination between the cellulose and the cell wall matrix components, it has been reported that a factor of 2 difference was preferred for successful spin diffusion experiments when using $T_{1\rho H}$ (Zumbulyadis 1983). To examine the influence of spin diffusion on the millisecond time scale, a variable spin-lock experiment was carried out with delay times ranging from 0.2 ms to 1.0 ms, much shorter than the $T_{1\rho H}$ values obtained from the previous spin-lock experiment.

It was found that the $T_{1\rho H}$ changed significantly to 44.6 ms for cellulose, 9.7 ms for hemicellulose, and 7.5 ms for lignin. By having a shorter spin-locking time, the effect of

spin diffusion was minimised giving a clearer value of the individual $T_{1\rho H}$ values of the components. Cellulose showed a clear increase in $T_{1\rho H}$, and both hemicellulose and lignin show a decrease at shorter spin-locking times when compared to the 1 ms to 10 ms variable spin-lock experiment. This indicates that spin diffusion was occurring over the time of the spin-locking pulse, resulting in the partial averaging of the $T_{1\rho H}$ values as the spin-locking time increased. This emphasised that $T_{1\rho H}$ values are dependent not only on the spin-locking field frequency, but also on the range of times used for determining them. As such, the use of $T_{1\rho H}$ as a discriminator for spin diffusion experiments was considered not the best option due to the added complication of spin diffusion that occurs during the spin-locking time which is in addition to the spin diffusion that occurs during the contact pulse used for cross polarisation.

T_{2H} measurements

T_{2H} was measured by the fitting of nutation plots using cellulose (89 ppm), hemicellulose (101.4 ppm), and lignin (56 ppm) peaks. These were fitted using a modified Weibull function as described previously (Chapter 3).

Figures 5.5, 5.6, and, 5.7 give the best Weibull fit to cellulose, hemicellulose, and lignin respectively. Results of the fits are summarised in Table 5.1.

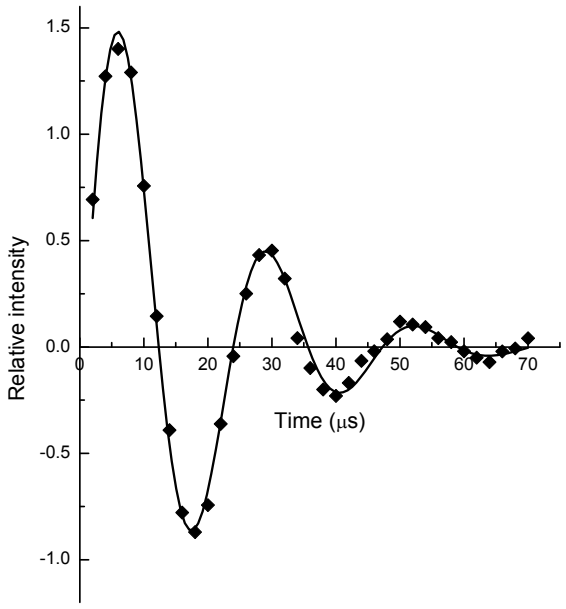

Figure 5.5 *Nutation plot fitted with a modified Weibull function of cellulose (89 ppm).*

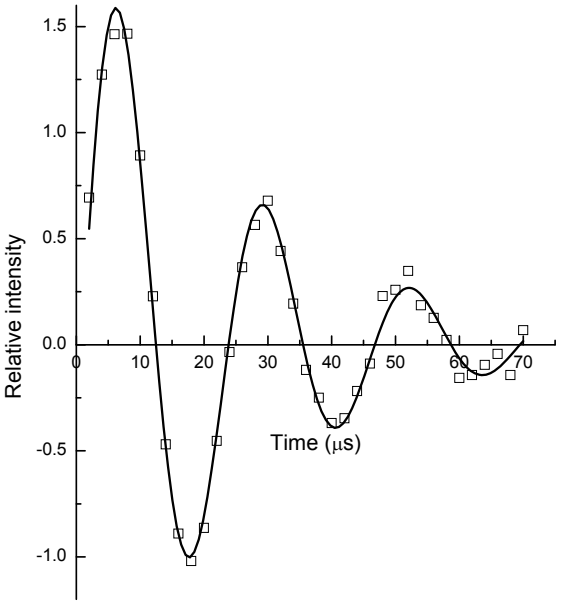

Figure 5.6 *Nutation plot fitted with a modified Weibull function of hemicellulose (102 ppm).*

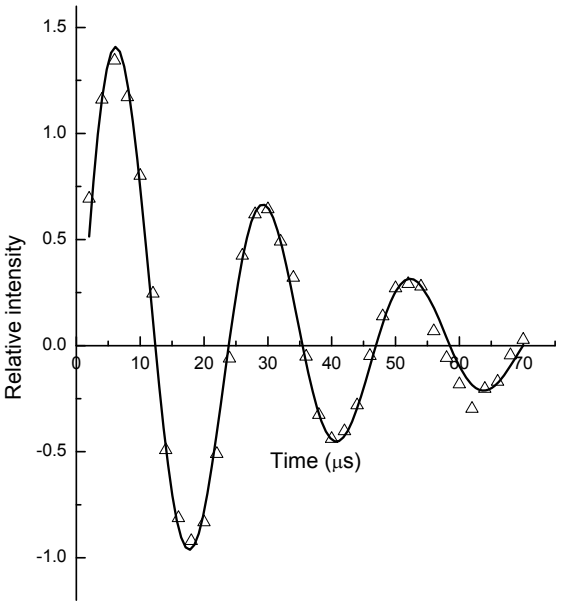

Figure 5.7 *Nutation plot fitted with a modified Weibull function of lignin (56 ppm).*

Table 5.1 *T_{2H} values based on Weibull function fits of nutation decay curves for never-dried wood.*

Component	*T_{2H} (μs)*	*Weibull "μ"*	*Curve fit RMS*
Cellulose	9.4	1.27	0.04
Hemicellulose	12.6	1.15	0.1
Lignin	15.4	1.00	0.1

T_{2H} discrimination had the advantages of short times (microseconds) allowing small domain sizes to be probed, and during its evolution, it was not greatly influenced by

spin diffusion, unlike T_{1H} and $T_{1\rho H}$, which, due to their time scales being long relative to spin diffusion, resulted in loss of information (Tanaka and Nishi 1986).

5.5 Perturbation of proton magnetisation

Discrimination between cellulose, hemicellulose, and lignin was accomplished using T_{2H} relaxation during nutation. Nutation plots were constructed for proton pulse times as long as 70 μs (Figure 5.8).

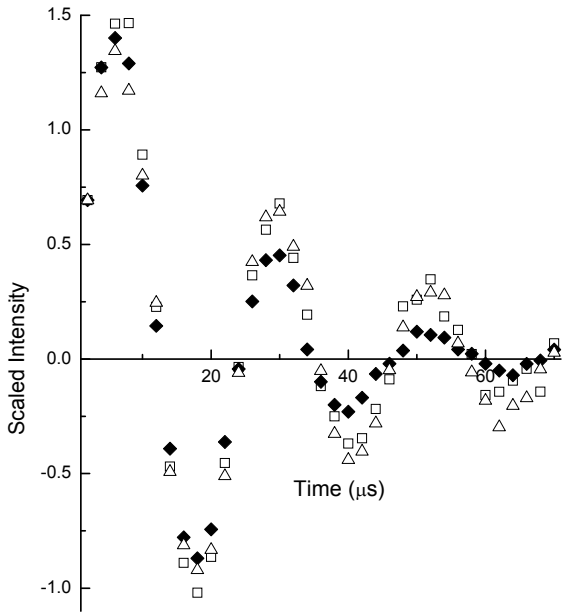

Figure 5.8 *Nutation plot of D_2O exchanged never-dried wood (solid symbol = cellulose C4 interior, open square = hemicellulose C1, open triangle = lignin OCH_3).*

At longer pulse times, the cellulose signal decayed faster than either of that of hemicellulose or lignin. Separation of the hemicellulose and lignin signals was not possible using T_{2H} discrimination. This indicated that either hemicellulose or lignin have the same intrinsic T_{2H} value, or that each polymer is in close proximity to the other such that over the time of the experiment spin diffusion averages out their T_{2H} values. From Figure 5.8 the pulse time was chosen to create a 540° proton tip angle allowing discrimination of cellulose from the matrix components and returning the magnetisation to the *Z*-axis (-Z) to allow spin diffusion.

5.6 Methods and results

^{13}C NMR signals were collected from D_2O soaked never-dried latewood (%MC 140%) using a 540° proton pulse to create the magnetisation perturbation followed a spin diffusion mixing time (from 1 ms to 169 ms) and then a CP sequence with a contact time of 1 ms, recycle delay of 1.5 s, acquisition time of 30 ms, and 12k transients. A

standard CP reference NMR spectrum was also collected. The intensities of cellulose (89 ppm), hemicellulose (101.4 ppm), and lignin (89 ppm) were extracted and divided by the intensities of the reference spectra values. These were then plotted against the Log_{10} of the mixing time (Figure 5.9).

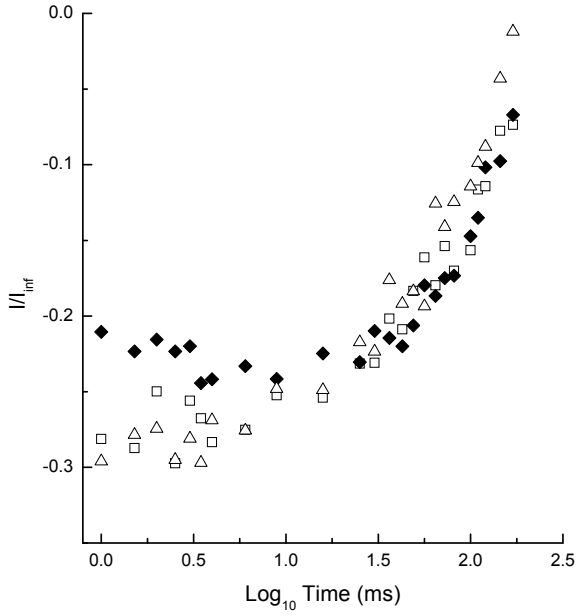

Figure 5.9 *Ratios of intensities of the cellulose 89 ppm peak (solid symbol), hemicellulose 101.4 ppm peak (open squares), and lignin 56 ppm peak (open triangles) against spin diffusion mixing time.*

The diffusion curves were modelled using Equations 5.6a and 5.6b, where $I_{cellulose}$ and I_{matrix} are the intensities of cellulose and matrix components respectively at time t, and T_m is the mixing time. T_{1H}, T_m and t are in ms and Δt = 1 ms. The first part of the equation accounts for exponential T_1 decay and the second for transference of magnetisation from the matrix components to the cellulose after perturbation (conservation of magnetisation is assumed). Repeating the iterative Equations 3.12a and 3.12b (Chapter 3) but explicitly labelling components.

$$I_{cellulose}^{t+\Delta t} = I_{cellulose}^{t}\left(1 - \frac{\Delta t}{T_{1\,cellulose(H)}}\right) + \frac{(I_{matrix}^{t} - I_{cellulose}^{t})\Delta t}{T_m} \qquad 5.6a$$

$$I_{matrix}^{t+\Delta t} = I_{matrix}^{t}\left(1 - \frac{\Delta t}{T_{1\,matrix(H)}}\right) - \frac{(I_{matrix}^{t} - I_{cellulose}^{t})\Delta t}{T_m} \qquad 5.6b$$

The value of $(1 - I)$ is then plotted against the Log_{10} of time (ms) adjusting the initial values of I, values of T_1(H), and T_m to obtain a best fit.

For cellulose and lignin, the best fit was found with a $T_{1H\ cellulose}$ of 5 s, a $T_{1H\ lignin}$ of 475 ms, and a T_m of 25 ms (Figure 5.10).

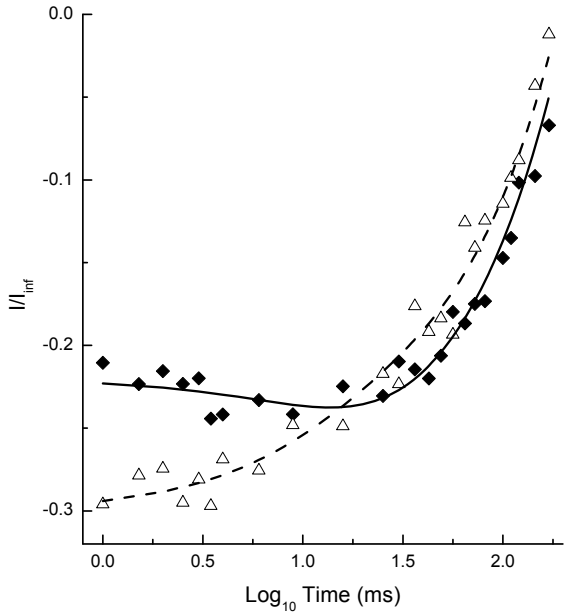

Figure 5.10 *Cellulose (closed symbol) and lignin (open symbol) fitted spin diffusion curves for never-dried D_2O-exchanged latewood (1 ms contact time).*

For cellulose and hemicellulose, the best fit was found with a $T_{1H\ cellulose}$ of 5 s, a $T_{1H\ hemicellulose}$ of 550 ms, and a T_m of 24 ms (Figure 5.11).

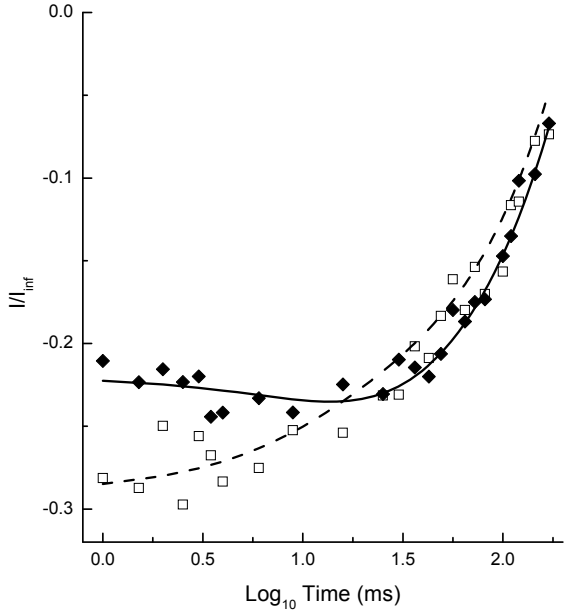

Figure 5.11 *Cellulose (closed symbol) and hemicellulose (open symbol) fitted spin diffusion curves for never-dried D_2O-exchanged latewood (1 ms contact time).*

To test the effect of spin diffusion during the contact time and experimental scatter, the spin diffusion experiment was repeated using a fresh specimen of D_2O exchanged never-dried latewood (%MC 148%) using the same conditions as the previous

experiment except as noted below. Proton spin diffusion data were collected using 11 spin diffusion times ranging from 0.1 s to 100 s, a contact time of 0.2 ms to minimise spin diffusion during the contact pulse, and 12k transients per spin diffusion time. Each spin diffusion experiment represented 58 hours of NMR time and 4 replicates were collected and the data averaged. Filled rotors were weighed before and after data collection to check for loss of moisture during the experiment. The weight of the never-dried wood sample, plus that of the rotor was 0.7525 g before and after analysis, which indicated differences observed in the NMR experiments were not due to changes of moisture content in the specimens. Data processing was carried out as described above.

An example of a ^{13}C CP-MAS spectrum of never-dried latewood using a contact time to 0.2 ms and 12k transients is shown in Figure 5.12. Despite the short contact time the signal to noise ratio was found to be adequate for proton spin diffusion analysis for the chosen cellulose, hemicellulose and lignin resonances.

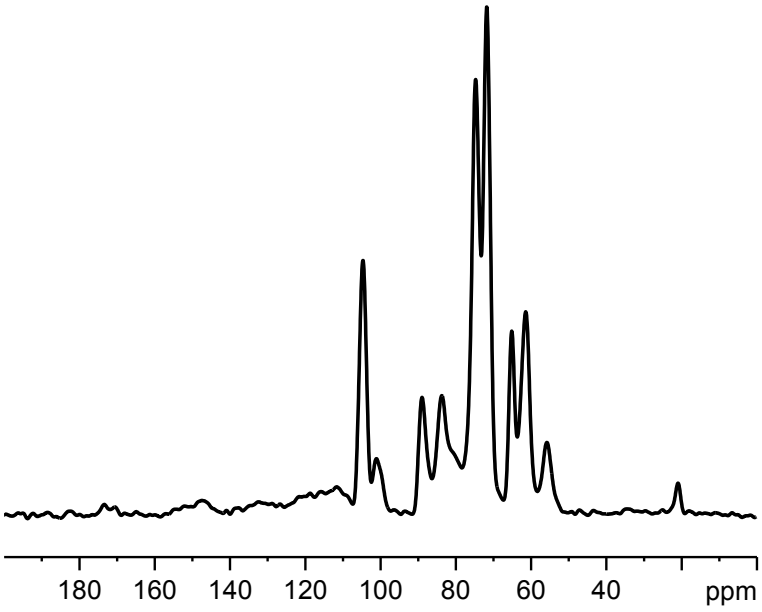

Figure 5.12 *Example of a ^{13}C CP-MAS spectrum of never-dried latewood using a contact time to 0.2 ms and 12k transients.*

For cellulose and lignin, the best fit was found with a $T_{1H\ cellulose}$ of 5 s, a $T_{1H\ lignin}$ of 300 ms, and a T_m of 23 ms (Figure 5.13).

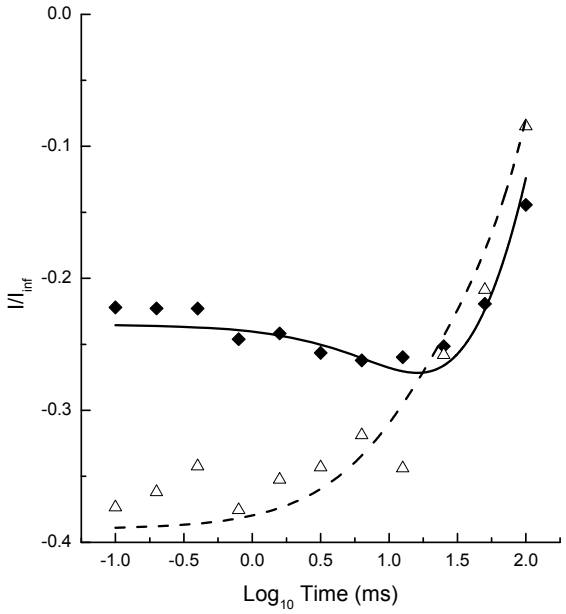

Figure 5.13 *Spin diffusion plot for cellulose (solid symbol) and lignin (open symbol) with modelled fitting (black lines) for never-dried D_2O-exchanged latewood (0.2 ms contact time).*

For cellulose and hemicellulose, the best fit was found with a $T_{1H\ cellulose}$ of 5 s, a $T_{1H\ hemicellulose}$ of 400 ms, and a T_m of 26 ms (Figure 5.14).

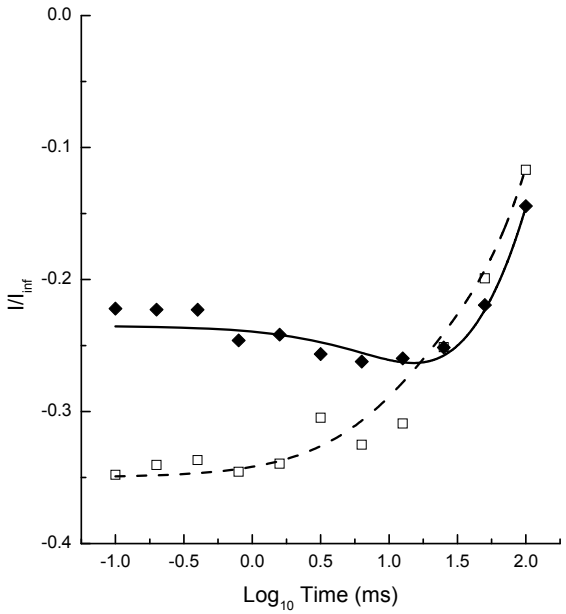

Figure 5.14 *Spin diffusion plot for cellulose (solid symbol) and hemicellulose (open symbol) with modelled fitting (black lines) for never-dried D_2O-exchanged latewood (0.2 ms contact time).*

The results showed no evidence for significant spin-diffusion mixing during the contact time, and an average spin diffusion mixing time of 24.5 ms for never-dried latewood,

similar that that obtained from the spin-diffusion experiment with a longer contact time (also average T_m = 24.5 ms).

Combining the T_m times from all proton spin-diffusion experiments an average T_m of 24.5 ± 1.2 ms (95% C.I.) is obtained for D_2O exchanged never-dried latewood.

Perturbation of wood cell wall-water structure and distribution by drying

A nutation experiment showed that T_{2H} values for cellulose and the matrix were changed by a dry-rewet cycle (rewet with D_2O, Figure 5.15, Table 5.2). Individual fits of the nutation plots for cellulose, hemicellulose, and lignin are given as Figures 5.16, 5.17, and 5.18 respectively.

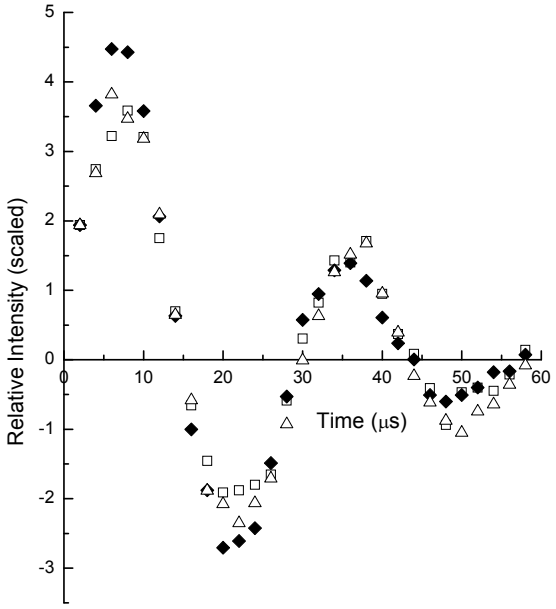

Figure 5.15 *Nutation plot of D_2O exchanged never-dried wood which had been oven-dried (solid symbol = cellulose C4 interior, open square = hemicellulose C1, open triangle = lignin OCH_3).*

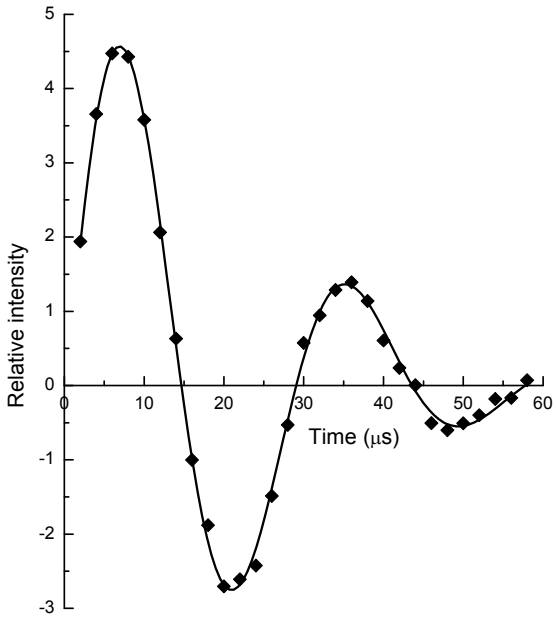

Figure 5.16 *Nutation plot fitted with a modified Weibull function of cellulose (89 ppm) of oven-dried and D_2O-rewet latewood.*

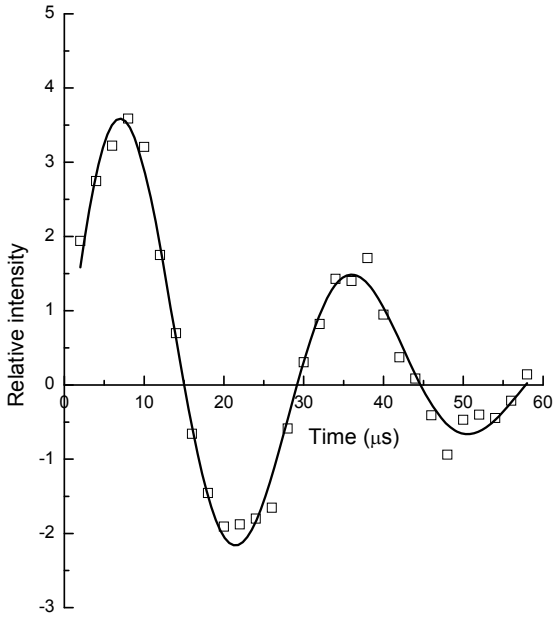

Figure 5.17 *Nutation plot fitted with a modified Weibull function of hemicellulose (102 ppm) of oven-dried and D_2O-rewet latewood.*

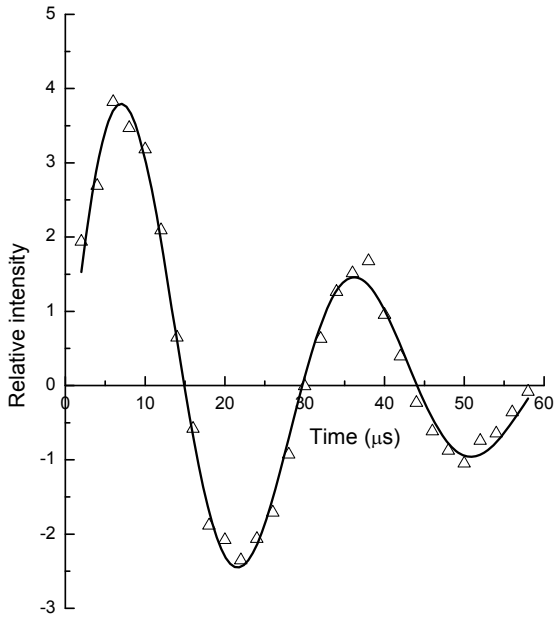

Figure 5.18 *Nutation plot fitted with a modified Weibull function of lignin (56 ppm) of oven-dried and D_2O-rewet latewood.*

Table 5.2 *T_{2H} values based on Weibull function fits of nutation decay curves for oven-dried and D_2O rewet wood.*

Component	*$T_2(H)$ (μs)*	*Weibull "μ"*	*Curve fit RMS*
Cellulose	11.2	1.50	0.1
Hemicellulose	10.4	1.53	0.2
Lignin	14.4	1.26	0.2

The results of these spin diffusion experiments have shown that the spin diffusion mixing time from matrix to cellulose in D_2O soaked, never-dried latewood is approximately 23 to 26 ms after perturbation by T_{2H}. If this mixing was due solely to the components of cellulose and matrix, then it would be expected to persist no matter what the hydration state or hydration history of the wood cell wall. To test this hypothesis, and to probe the models presented in Chapter 4 (Model 3, Figure 4.5a and Model 4, Figure 4.5b), never dried wood that had been soaked in D_2O was dried to constant weight at 105°C, and then rewet to saturation with D_2O. The final D_2O moisture content for NMR analysis was 128% (rotor plus sample weight 0.7476 g before and 0.7476 g after analysis).

The best-fit T_m for this sample was found to be 13 ms and 11 ms for lignin and hemicellulose respectively (Figures 5.19 and 5.20). Comparing this T_m with the previous spin diffusion mixing time of an average of 24.5 ms showed that once wood cell walls had been oven dried there was a change in the structure of the cell wall that simple rehydration (for these experiments, with D_2O) could not reverse.

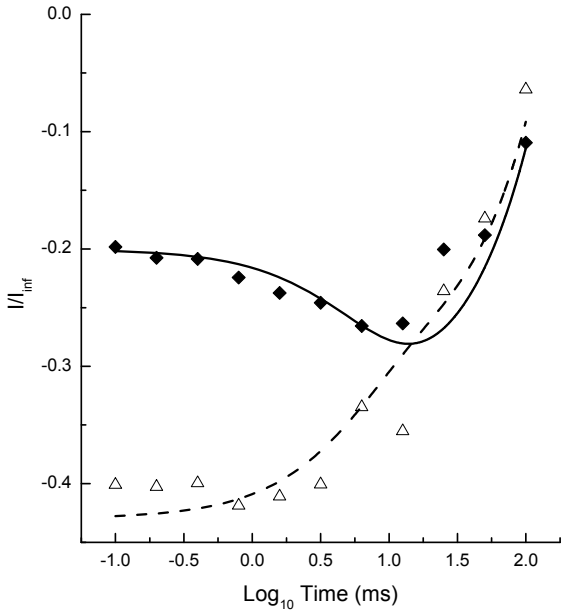

Figure 5.19 *Spin diffusion plot for cellulose (solid symbol) and lignin (open symbol) with modelled fitting (black lines) for oven-dried and D_2O-rewet latewood (0.2 ms contact time).*

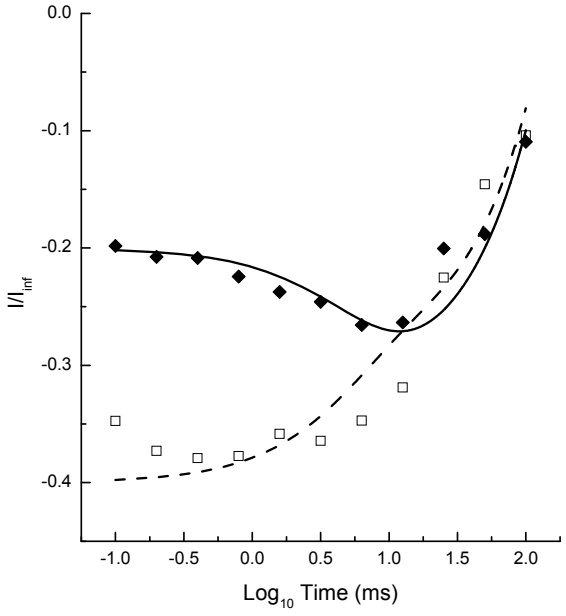

Figure 5.20 *Spin diffusion plot for cellulose (solid symbol) and hemicellulose (open symbol) with modelled fitting (black lines) for oven-dried and D_2O-rewet latewood (0.2 ms contact time).*

Perturbation of wood cell wall-water structure and distribution by multiple drying-rewetting cycles

To further study the effects of drying on the wood cell wall a specimen was subjected to multiple dry-wet cycles.

Never dried wood that had been soaked in D_2O was dried to constant weight at 105°C, and then rewet to saturation with D_2O with four repeats of this cycle. This was carried out in order to maximally perturb the cell wall structure by multiple drying, a process well known to shrink bulk wood material and after bulk material properties (Kininmonth 1976). The final D_2O moisture content for NMR analysis was 175% (rotor plus sample weight 0.7592 g before and 0.7593 g after analysis).

The best-fit T_m for this sample was found to be 7 ms and 3 ms for lignin and hemicellulose respectively (Figures 5.21 and 5.22). Comparing this T_m with the previous spin diffusion mixing times, of an average of 24.5 ms for D_2O exchanged never-dried and an average of 12 ms for oven-dried D_2O rewet latewood, showed that once wood cell walls had been multiply dried, there was an irreversible change to the cell wall nanostructure and rehydration (for these experiments, with D_2O) of the cellulose crystallites was no longer possible

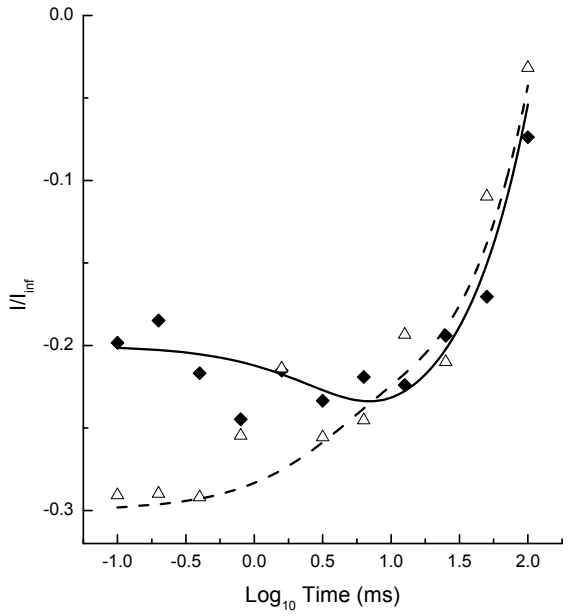

Figure 5.21 *Cellulose (closed symbol) and lignin (open symbol) fitted spin diffusion curves for quadruply oven-dried and D_2O-rewet latewood (0.2 ms contact time).*

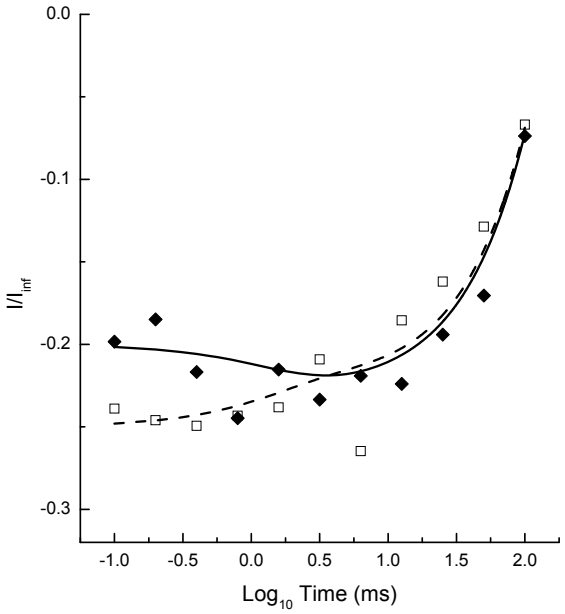

Figure 5.22 *Cellulose (closed symbol) and hemicellulose (open symbol) fitted spin diffusion curves for quadruply oven-dried and D_2O-rewet latewood (0.2 contact time).*

Interpretation of this evidence reinforced the concept of the never-dried wood cell wall model (Model 2, Figure 1.1, Chapter 1 and Model 4, Figure 4.5b, Chapter 4), where a spin diffusion barrier between the cellulose microfibril and the cell wall matrix was created by substitution of H_2O with D_2O, and that this barrier can be collapsed and was unable to reform on rewetting after exhaustive drying.

Results and fitting parameters are summarised in Table 5.3.

Table 5.3 *Best fit T_m values obtained from spin diffusion model fits to proton spin diffusion NMR data of D_2O exchanged latewood specimens.*

Specimen	*%MC*	*Magnetisation source*	*T_m (ms)*	*T_1(H) cellulose* (s)*	*T_1(H) source* (ms)*
Never-dried[a]	140%	Lignin	25	5	475
		Hemicellulose	24	5	550
Never-dried[b]	148%	Lignin	26	5	300
		Hemicellulose	23	5	400
Oven-dried rewet[b]	128%	Lignin	13	5	300
		Hemicellulose	11	5	300
Oven-dried rewet cycled[b]	175%	Lignin	7	5	300
		Hemicellulose	3	5	400

a = 1 ms contact time spin diffusion experiment, b = 0.2 ms contact time spin diffusion experiments.

* = Best fit intrinsic T_1(H) values.

This result is analogous with the findings of Chapter 2, where an increase in the number of drying cycles resulted in a decrease of the observed reversibility of drying induced changes upon rewetting. In the case of Chapter 2 changes were observed in the unit cell parameters, *b* and *γ,* for the cellulose crystallites (Figure 2.22), and in the case of this Chapter, the relevant changes were observed in the spin diffusion mixing time (T_m).

5.7 Conclusions

Two models (Model 3, Figure 4.5a, Chapter 4 and Model 4, Figure 4.5b, Chapter 4) were presented as possible novel representations of the distribution and structure of water in the green wood cell wall and the cell wall after drying. It was shown that both models fit the observed proton spin-diffusion data, with the determining factor being the moisture content history of the wood specimen, *i.e.* in the green, fully-hydrated state or a state derived by drying from green or fibre-saturation point to some reduced moisture content, and re-hydration of the cell wall to a moisture content less than that at fibre saturation point.

The model of the green wood cell wall (Model 2, Figure 1.3, Chapter 1 and Model 4, Figure 4.5b, Chapter 4), in which the surface of the cellulose microfibril is physically separated from the surface of the cell wall matrix by a layer(s) of water has been shown to be the case in never-dried wood. However, on exhaustive drying, the water barrier collapses. When such a dried specimen is rewet, the water is unable to return to the locations it occupied in its never-dried state. This has been presented as Model 3 (Figure 4.5a, Chapter 4), where residual water is assumed to be randomly distributed throughout the matrix. The reasons for the change in water distribution in a dried and rewet wood specimen is a combination of conformational changes to the cellulose crystal surface chains (Chapter 2) and direct hydrogen bonding (precipitation) of glucomannan (hemicellulose) into the cellulose crystal surfaces.

The consequence of this on the bulk material mechanical properties of wood, specifically stress-relaxation, will be examined in the following chapter.

5.8 References

Altaner, C., Apperley, D.C., Jarvis, M.C. (2006) Spatial relationships between polymers in sitka spruce: Proton spin-diffusion studies. Holzforschung. 60:665-673

Donaldson, L. (2007) Cellulose microfibril aggregates and their size variation with cell wall type. Wood Science and Technology. 41:443-460

Gil, A.M., Neto, C.P. (1999) Solid-state NMR studies of wood and other lignocellulosic materials. Annual Reports on NMR Spectroscopy. 37:75-117

Kininmonth, J.A. (1976) Effect of timber drying temperature on subsequent moisture and dimensional changes. New Zealand Journal of Forestry Science. 6(1):101-107

Newman, R.H. (1992) Nuclear magnetic resonance study of spatial relationships between chemical components in wood cell walls. Holzforschung. 46(3):205-210

Salmen, L., Fahlen, J. (2006) Reflections on the ultrastructure of softwood fibers. Cellulose Chemistry and Technology. 40(3-4):181-185

Tanaka, H., Nishi, T. (1986) Spin diffusion in block copolymers as studied by pulsed NMR. Physical Review B. 33(1):32-42

Zumbulyadis, N. (1983) Selective carbon excitation and the detection of spatial heterogeneity in cross-polarization magic-angle-spinning NMR. Journal of Magnetic Resonance. 53:486-494

6 Stress relaxation mechanical testing of wood

6.1 Introduction

It has been shown that the bulk material mechanical behaviour of whole wood is similar to that of individual wood cells (Keckes et al. 2003). A mechanism for stress relaxation *via* permanent deformation of cell wall elements but without significant material damage has been described with an analogy to the 'slip and stick' of Velcro™ (Fratzl et al. 2004). It has been hypothesised that the molecular process of this relaxation mechanism is through hydrogen bonding between the cell wall hemicelluloses and cellulose (Keckes et al. 2003; Kretschmann 2003; Fratzl et al. 2004; Keckes et al. 2005). Although the above experiments were carried out on wetted specimens, no mention is made of the possibility of a contribution from water to the stress relaxation mechanism.

It is known that changes in the relative humidity (and therefore moisture content) rather than just wet versus dry states have an effect on stress relaxation of wood material. A cyclic behaviour was observed in wood material mechanics, with lower humidity resulting in higher stress, and when the wood moisture content increased as a result of increase in humidity to an initial value, the stress decreased (Ebrahimzadeth and Kubat 1993). These specimens were initially at a moisture content of 8.4% prior to humidity cycling which negated any information regarding the effects of such cycling on never-dried wood. However, it did show that the influence of water on stress relaxation was not only exhibited with wood both above and below fibre saturation point, but also the length of time of the moisture content conditioning process, wood had been subjected to. Over periods of weeks, wood appeared to stiffen even at high (93.8%) relative humidity (Ishimaru et al. 2001). However, the wood specimens displaying this behaviour had been previously exhaustively dried and then rewet. This result cannot therefore be interpolated back to comment on the behaviour of wood in its green state.

In the previous chapters, it was shown that wood after drying had a differing cellulose crystal geometry and water distribution in the cell wall if rewet. These differences, and their possible effect on the bulk material macro-mechanical properties, will be presented and discussed.

6.2 Hypothesis

As previously discussed the presence and location of water within the structure of wood cell walls has a marked effect on the properties of the material. It has been shown (Chapter 2) that the hydration state affects the transverse geometry of the microfibril cellulose crystals and that the location and distribution of the water changes when wood is dried and then is rewet (Chapter 5). These effects in concert should therefore have an effect on the macro-mechanical properties of wood that can be tested by lateral stress relaxation experiments. It is hypothesised that there should be large differences in stress relaxation behaviour between never dried and fully dried wood, and a smaller, but measurable, difference between never dried and dried and rewet specimens. To test this hypothesis, a Dynamic Mechanical Thermal Analysis (DMTA) instrument was used to measure the macro-mechanical properties of wood specimens prepared under conditions the same as those used for the cell wall structural studies in previous chapters.

6.3 Instrumental set-up

Samples of latewood (selected as per previous studies in this thesis) were cut into matchstick sized pieces. Dimensions were measured by the average of the ends and the mid-point of the specimens using electronic callipers and of set length (Table 6.1). The specimen size allowed a visual inspection for the presence physical defects in the wood, such as cracks, that may have influenced the mechanical testing.

Table 6.1 *Specimen dimensions and treatments for DMTA stress relaxation analysis.*

Specimen	*Dimensions (W x T, L = 10 mm)*	*Specimen treatment*
1	1.13 x 0.95 mm	Never dried
2	1.30 x 1.15 mm	Never dried
3	1.14 x 1.10 mm	Never dried
4	1.28 x 1.21 mm	Never dried
5	1.18 x 1.04 mm	Never dried
6	0.70 x 0.60 mm	Dried at 105 °C
7	0.70 x 0.60 mm	Dried at 105 °C
8	0.65 x 0.60 mm	Dried at 105 °C
9	1.53 x 1.05 mm	Dried at 105 °C and rewet
10	1.26 x 1.04 mm	Dried at 105 °C and rewet
11	1.21 x 1.03 mm	Dried at 105 °C and rewet

W = width, T = thickness, and L = length.

All samples were analysed using a dynamic mechanical thermal analyzer, DMTA V (Rheometric Scientific Inc.), operating with RSI Orchestrator software v6.5.5. The DMTA was used in an inverted configuration with the load cell pointing downwards.

For the never-dried and dried-rewet specimens the load cell apparatus was placed inside a beaker of distilled water to maintain the specimen in a water saturated condition during testing. For the dried samples, the beaker was left empty. (Figure 6.1). The data-sampling rate was set at 1.2 Hz and data were collected over 1 hour for 701 data points per specimen. All samples were positioned such that the specimen ends were equidistant with respect to the DMTA sample holder clamps. Oven dried specimens were allowed to reach a moisture-content equilibrium on a bench in the room containing the DMTA at a temperature of 20 °C and an RH of 65% for 1 hour prior to analysis.

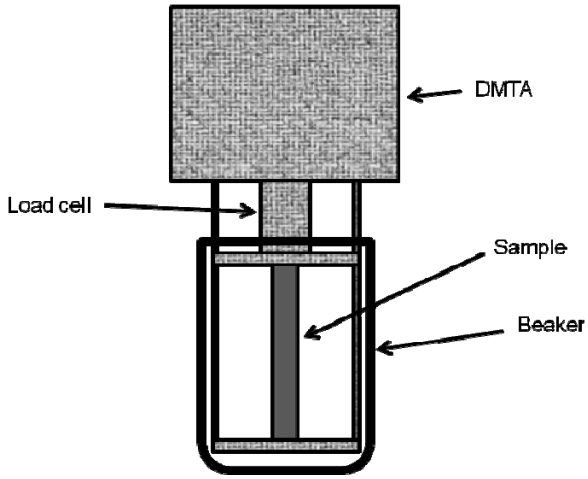

Figure 6.1 *Inverted configuration of the DMTA used for stress relaxation measurements.*

Samples were clamped into the apparatus and kept for 5 minutes before a strain of 0.2% (0.02 mm extension) was applied. The resulting stress was then measured from time = 0 seconds to time = 3600 seconds (1 hour).

6.4 Results

The oven-dried specimens (average of specimens **1** to **5**) reached a maximum stress of 28.6 MPa after 11 seconds after the application of 0.2% strain. The never dried specimens (average of specimens **6** to **8**) and subsequently rewet specimens (average of specimens **9** to **11**) achieved a maximum measured stress of 8.8 MPa and 8.5 MPa respectively after 6 s (Figure 6.2).

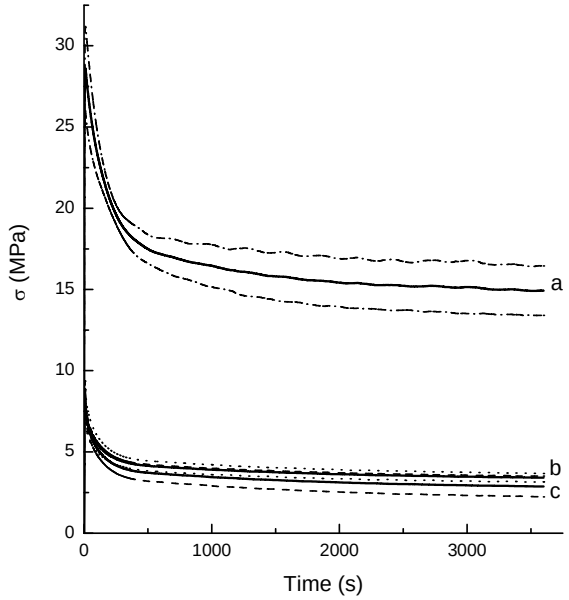

Figure 6.2 *Stress relaxation curves for (a) oven dried, (b) oven dried and rewet, and (c) never dried latewood (dash/dotted lines give the 95% confidence interval for replicates).*

When the stress was normalised it was seen that after 1 hour, the maximal stress the fully dried specimens had on average lost 48% of their initial stress compared to an average loss of 67% and 60% of initial stress for never dried and dried and rewet specimens respectively (Figure 6.3).

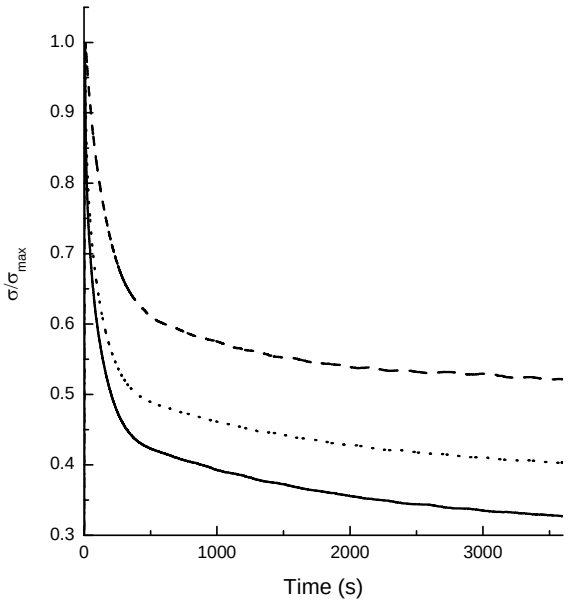

Figure 6.3 *Normalised stress relaxation curves (dashed line = oven dried, dotted line = oven dried and rewet, and solid line = never dried).*

This showed that wood material in the fully hydrated green state was more compliant than in the fully dried state, and there was an indication that once fully dried, some of the elasticity was permanently lost, as shown by the fully-dried and subsequently rewet specimens.

Relatively good fits for the data can be produced by using a Maxwellian type approach and using the sum of exponentials (Grossman 1954) (Equation 6.1).

$$\sigma = \sigma_o \Sigma c_i \exp\{-t / \tau_i\} \qquad 6.1$$

In this equation, σ_o is the initial stress, σ is the stress at time t, and c_i and τ_i are constants.

During the initial stages of the applied strain of 0.2%, the oven-dried specimen behaved differently compared with the never-dried and oven-dried and subsequently rewet specimens (Figure 6.4).

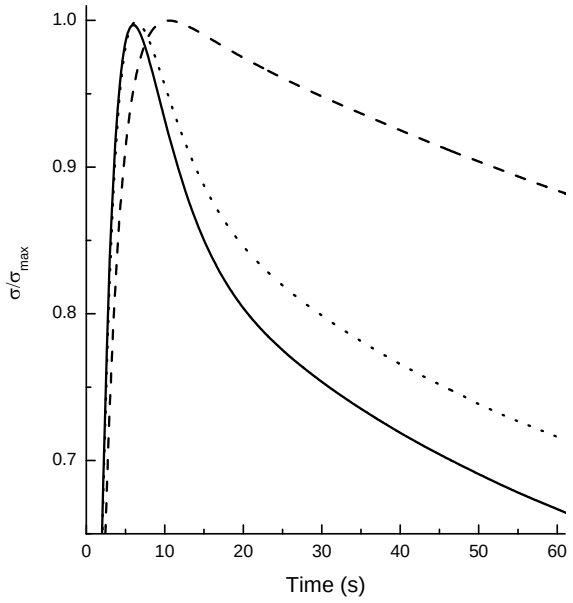

Figure 6.4 *Normalised initial stress relaxation curves (dashed line = oven dried, dotted line = oven dried and rewet, and solid line = never dried).*

The source of the initial differences in stress-relaxation behaviour was difficult to determine, as it was a function of the material and instrumental mechanics adjusting to the individual specimen. The application of the strain was theoretically instant, but in practise required an unspecified period of adjustment within the instrument. As such, the first 30 seconds of data were not used in any further analysis. Of particular interest

in this study was the stress-relaxation response after the 0.2% strain had been applied and the specimen was at 0.2% strain (0.02 mm elongation).

When the data were plotted on a Log time scale, it was clear that there were two distinct relaxation phases, as previously reported (Figure 6.5) (Kubat et al. 1989).

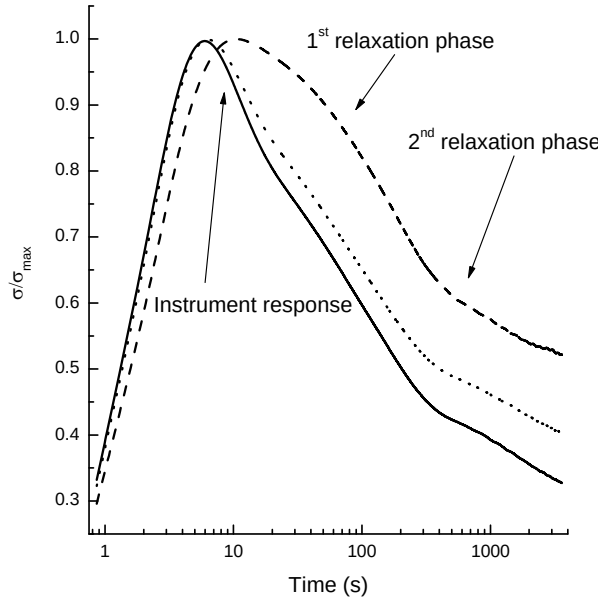

Figure 6.5 *Normalised stress relaxation verse log_{10} time curves (dashed line = oven dried, dotted line = oven dried and rewet, and solid line = never dried).*

After approximately 30 seconds, the stress decay appeared to be in the form of a bi-exponential form. These data were fitted using a bi-exponential function of the form (Equation 6.2, Figure 6.6).

$$\sigma / \sigma_{max} = (c \times exp\{-t / T_f\}) + (c' \times exp\{-t / T_s\}) + (\sigma / \sigma_{max})_{inf} \qquad 6.2$$

In this equation, t = stress-relaxation time (s), T_f and T_s = fast and slow stress-relaxation rate time constants respectively, $(\sigma / \sigma_{max})_{inf}$ = minimum obtained stress-relaxation ratio at infinite time, and c and c' = constants.

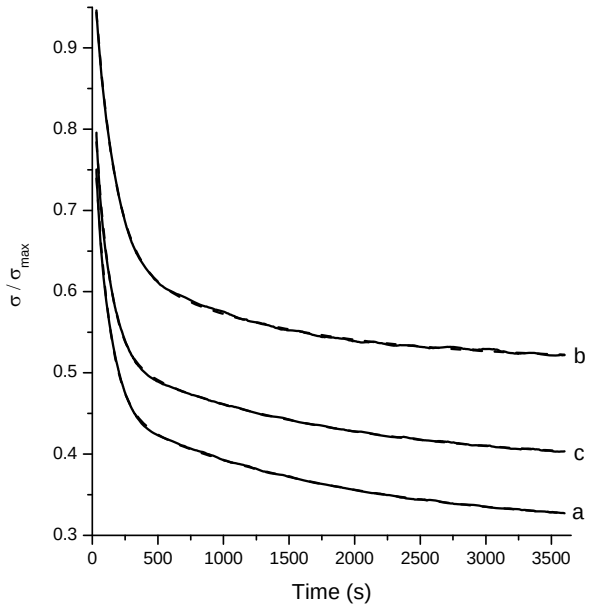

Figure 6.6 *Bi-exponential curve fits of (a) never-dried, (b) oven-dried, and (c) oven-dried and rewet wood specimens at times greater than 30 seconds after 0.2% applied strain (data = solids lines, curve fitting = dashed lines).*

The time constant parameters and remaining stress at infinite time obtained from a bi-exponential fit are given in Table 6.2.

Table 6.2 *Bi-exponential decay time constants for stress-relaxation of never-dried, oven-dried, and oven-dried & rewet wood.*

Specimen treatment	*Decay constant (T_f, s) [proportion]*	*Decay constant (T_s, s) [proportion]*	*$(\sigma / \sigma_{max})_{inf}$*	*RMS error*
Never-dried	108 [28%]	1776 [72%]	0.31	0.002
Oven-dried	145 [25%]	1245 [75%]	0.52	0.001
Oven-dried & rewet	107 [28%]	1604 [72%]	0.39	0.002

During the first stress-relaxation phase, the oven-dried specimen had a slower relaxation compared with that of the never-dried and rewet specimens. The never-dried and rewet specimens showed similar relaxation behaviour. In the second stress-relaxation phase, the oven-dried specimen showed slower relaxation than either of the never-dried or the rewet specimens. However, in the second relaxation phase, the rewet specimen showed a slower relaxation rate than the never-dried specimen, resulting in more remaining stress at the end of the 1 hour of the experiment (Figure 6.7).

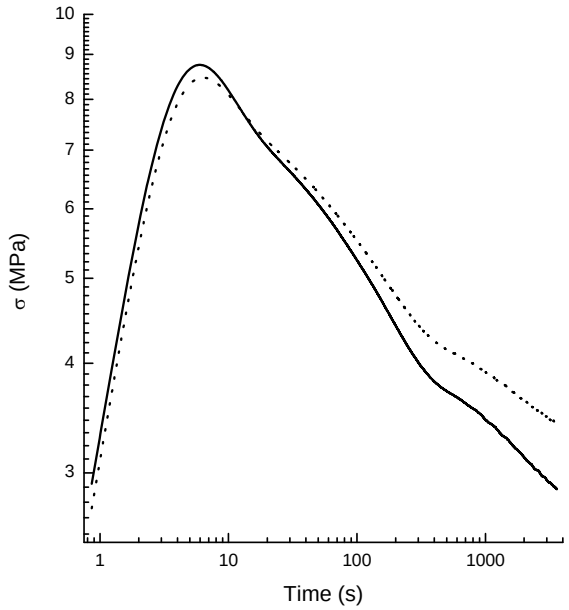

Figure 6.7 *Log_{10} stress relaxation verse log_{10} time curves (dashed line = oven dried, dotted line = oven dried and rewet, and solid line = never dried).*

6.5 Conclusions

The cambium and sapwood of living trees exist in a stable state, being fully saturated with water. Drying induces an unstable state (Ishimaru et al. 2001). This statement is extended to consider the role that water plays in the mechanical properties of the wood. During strain, it has been shown previously that the cell wall microfibril cellulose crystal dimensions elongate in the direction of the fibre repeat (004), but decrease in the crystal sheet hydrogen-bonding plane (200) (Peura et al. 2007). In contrast, as has been shown in Chapter 2, the change in the moisture content of wood was shown to have an effect on the transverse geometry of the cellulose crystal unit cell, but with no significant change to the fibre repeat distance. Chapter 5 presents evidence that not only the moisture content, but also the distribution of the water in the wood cell wall has an effect on the overall cell wall cellulose microfibril and hemicellulose-lignin matrix structure.

As the proportions of the fast and slow relaxation phases for each specimen are similar, it is likely that the mechanisms involved are also similar.

The presented stress-relaxation data showed no significant difference in the relaxation behaviour of never-dried and fully-dried and rewet specimens in the first phase of the relaxation process. This would indicate that the initial relaxation is independent of the distribution of the water within the cell wall, and not significantly related to a water layer being present about the cellulose microfibril. However, as the oven-dried specimen

has a different first relaxation phase behaviour, this indicates that the quantity and distribution of water in the cell wall maintains a major role in stress relaxation. The initial slower rate of relaxation of the oven-dried specimen may be due a dehydrated matrix being stiffer compared with the water swollen matrix present in the never-dried and dried and then rewet specimens. As such, this initial relaxation phase may represent a reorganisation of the matrix, and a relaxation of any elongation of the cellulose crystallites. An elongation of the fibre repeat distance has been mentioned as a possible relaxation process (Keckes et al. 2003), and the matrix has been shown to have an effect on such a deformation of cellulose crystallites (Peura et al. 2007).

In the second relaxation phase, the oven-dried specimen has the fastest relaxation rate, perhaps indicating slippage of cellulose microfibrils in the matrix may be occurring. If this were the case, then the hydrogen bonding between the cellulose crystallite surface and hemicellulose-lignin matrix would have an effect on the rate of relaxation. This can be seen in the dried and then rewet specimen, which has an intermediate relaxation time between oven-dried and never-dried. The never-dried specimen shows the slowest relaxation rate, which is interpreted as being due the water layer proposed between the cellulose microfibril surface and matrix, taking some of the stress by reorganising the hydrogen-bonding of water rather than slippage being the only mechanism for stress relaxation. In the case of the dried and then rewet specimen, the rewetting process is understood not to have restored the water to its original green state (refer to Chapter 5) and this is seen as a relaxation rate intermediate between never-dried and oven-dried states.

Although it is not possible to determine the actual mode of stress-relaxation in the two phases, it can be seen that there are significant differences in the stress as calculated at infinite time. The never-dried specimens relieve 69% of maximum stress caused by the application of 0.2% strain; the oven-dried specimens relieve 48% and the dried and then rewet specimens 61% of their maximum stress. After 1 hour of relaxation, the specimens were close to the predicted maximum stress relaxation. The oven-dried specimens and dried and subsequently rewet specimens are proposed to have more stress locked in upon application of a strain due to changes in structure in the cell wall during drying, whereas the never-dried wood material structure allows a major part of stress relaxation through a mechanism proposed to be through exchange of water molecules at the cellulose crystal surface with more mobile water molecules in a water mediated ‘slip and stick’ mechanism.

6.6 References

Ebrahimzadeth, P.R., Kubat, D.G. (1993) Effects of humidity changes on damping and stress relaxation in wood. Journal of Materials Science. 28:5668-5674

Fratzl, P., Burgert, I., Gupta, H.S. (2004) On the role of interface polymers for the mechanics of natural polymeric composites. Physical Chemistry Chemical Physics. 6:5575-5579

Grossman, P. (1954) Stress relaxation in wood. Nature. 173:42-43

Ishimaru, Y., Oshima, K., Iida, I. (2001) Changes in the mechanical properties of wood during a period of moisture conditioning. Journal of Wood Science. 47:254-261

Keckes, J., Burgert, I., Fruhmann, K., Muller, M., Kolling, K., Hamilton, M., Burghammer, M., Roth, S.V., Stanzl-Tschegg, S., Fratzl, P. (2003) Cell-wall recovery after irreversible deformation in wood. Nature Materials. 2(810-814)

Keckes, J., Burgert, I., Muller, M., Kolln, K., Hamilton, M., Burghammer, M., Roth, S.V., Stanzl-Tschegg, S.E., Fratzl, P. (2005) In-situ WAXS studies of structural changes in wood foils and in individual wood cells during mircotensile tests. Fibre Diffraction Review. 13:48-51

Kretschmann, D. (2003) Velcro mechanics in wood. Nature Materials. 2:775-776

Kubat, D.G., Samuelsson, S., Klason, C. (1989) Stress relaxation in wood (Scots pine veneer). Journal of Materials Science. 24:3541-3548

Peura, M., Kolln, K., Grotkopp, I., Saranpaa, P., Muller, M., Serimaa, R. (2007) The effect of axial strain on crystalline cellulose in norway spruce. Wood Science and Technology. 41:565-583

7 Conclusions

7.1 Conclusions

Wood as a material exhibits properties that allow it to deform beyond its plastic limit without degradation of its mechanical properties. The hypothesis that water plays a functional role in the nano-structure and mechanical properties of wood cell walls was proposed and tested. Wood material in various hydration states and moisture content histories was examined to search for effects on the cellulose crystallites, macromolecular interactions of cellulose and the matrix, and the material mechanical properties in order to understand this behaviour further. A summary of the findings from the experimental work to test this hypothesis are given below.

It was found that there were changes in the cellulose microfibril crystallites as reflected in changes to the cellulose unit cell parameters as modelled for cellulose Iβ when the moisture content of the wood material was changed. Changes to the unit cell parameters of *b*, the direction of intra-chain hydrogen bonding layer, and *γ*, the offset of the chains above and below a given chain layer were observed. This showed that the cellulose crystal chains packed closer together along the H-bonded planes upon drying. No significant changes to the unit cell parameters of *a*, intra-layer distance, and *c*, the fibre repeat distance were observed. The degree of divergence of the unit cell parameters, *b* and *γ*, on drying wood material from the never-dried state was dependant on the severity of the drying process. Both parameters showed a decrease with increasing severity of drying indicating that during drying conformational changes take place on the surface chains of the cellulose crystal. This allows the chains in the b direction to pack more efficiently and this in turn has the effect of reducing the angle *γ*. The observed degree of recovery of the unit cell parameters of dried samples when rewet was found to be also dependant on the drying method. Air-dried specimens showed almost complete recovery of the unit cell parameters *b* and *γ*, while the oven dried and quadruply oven-dried showed only partial recovery after rewetting. The change in the unit cell parameters can be attributed to the hydration state of the cellulose microfibril surface and given their large surface area to volume ratio, the forces imposed by the hydration state on the cellulose crystal structure. On rewetting, the partial recovery of the unit cell parameters *b* and *γ* has been attributed to an irreversible conformational change, dependant on the temperature of drying, to the surface chains of the cellulose crystal from a *gauche-trans* / *gauche-gauche* (*gt*/*gg*) conformation to a cellulose crystallite interior like *trans-gauche* (*tg*) conformation and the precipitation and hydrogen bonding of hemicelluloses onto the cellulose crystallites.

This conformation change and precipitation of the matrix, probably the hemicellulose, onto the cellulose surface reduces the number of available hydrogen bonding sites on the cellulose crystallite surfaces to hydrogen bond with water. This effect on wood material drying may explain the reduction in the equilibrium moisture content (EMC) observed in forcibly dried wood, such as kiln-dried.

From X-ray diffraction data, it was possible to construct a model of the wood cell wall assuming direct contact between cellulose and the matrix. Cell wall molecular interactions have been attributed with imparting the mechanical properties of wood. The reasons for this behaviour have been discussed in terms of the molecular Velcro® model although the mechanism for the hooks and loops had only been suggested as a possible explanation. Using NMR spin diffusion techniques, the role that water played in the transference of stresses and recovery of material properties after the cessation of the stress was examined. Two models were presented, one in which the water was localised around, thought not exclusively, the cellulose crystallites (Model 4, Figure 4.5b, Chapter 4), and another where the water was randomly distributed throughout the cell wall (Model 3, Figure 4.5a, Chapter 4). In the first model, the molecular nature of the Velcro® would be mediated by the water layer(s) between the cellulose crystallite surface and the matrix, and in the second model, the Velcro® would act, as initially suggested in the literature, by direct cellulose-hemicellulose interactions. By using time constants from spin diffusion experiments rather than calculating intermolecular distances, the need for precise spin diffusion coefficients for such heterogeneous material as wood was avoided. The model of the wood cell wall predicted a spin-diffusion time constant of 1.7 ms for direct cellulose-matrix contact. It was found that never dried wood had a time constant of 25 ms and quadruply oven-dried and rewet specimens, a time constant of 3 ms. This indicated that in the case of never-dried wood, the water forms a barrier between cellulose and the matrix acting as the Velcro® allowing the wood to respond to stresses without mechanical damage occurring. Nothing can be said regarding the number of water layers that make up the barrier, only its presence in never-dried wood. In the case of quadruply oven-dried wood, after rewetting, the water does not reform the barrier between cellulose and matrix. This may be due to the chains on the surface of the cellulose crystallites undergoing a conformational change reducing their hydrophilicity. This, in conjunction with the precipitation of hemicellulose onto cellulose crystallite surfaces, has the effect of stiffening the Velcro® and reducing the flexibility of the structure to respond to stresses. It is concluded that both Model 3 (Figure 4.5a, Chapter 4) and Model 4 (Figure 4.5b, Chapter 4) are both acceptable in explaining the observed behaviour of wood under dry-wet cycling conditions, with Model 3 (Figure 4.5a, Chapter 4) suitable for never

dried wood and Model 4 (Figure 4.5b, Chapter 4) for oven-dried and rewet wood. Given that the dried and then rewet wood specimens were saturated with water when studied and that there was no evidence for the existence of a water barrier between cellulose and the matrix in these specimens, it was also concluded that oven-dried wood at any moisture content is different from never dried with regards to not only the moisture content, but importantly the water distribution and water structure within the cell wall.

Stress relaxation experiments showed the effect that hydration state and importantly the moisture history has on the ability of the wood material to respond to applied strain. It was found that never dried wood was less stressed by the application of strain, and was able to relieve the induced stresses more efficiently than did oven-dried wood. Oven dried wood once rewet showed a stress relaxation behaviour similar to that of never dried wood, with the exception that it was unable to relieve as much of the induced stress as never dried wood over a similar time period. The difference between the never dried and dried and rewet specimens was explained in terms of loss of the water layer(s) between cellulose and the matrix and the precipitation of hemicelluloses into the cellulose crystallite surfaces, increasing the overall stiffness, and reducing the ability of the cell wall to transfer stress as effectively.

It has been shown that the properties of wood result from a complex interaction at all levels of the cell wall architecture and that water must be included as an integral part when describing the overall wood structure. As such, the composition of the cell wall should be considered as *cellulose*, *hemicelluloses*, *lignin*, and *water* when modelling its properties. In addition the moisture history of the wood must be taken into account, as the not only amount but the distribution and structure of the water within the cell wall has implications for the bulk materials mechanical properties.

7.2 Future work

To further explore and understand the effects of moisture content on observed changes to the unit cell parameters of cellulose, the work presented in this thesis and the methodologies should be extended to investigate different types of cellulose sources, such as other species of softwoods, hardwoods, and non-wood cellulose. By using cellulose crystals of differing sizes and cellulose with and without a surrounding matrix will advance understanding the role that surface water molecules play in changes to the unit cell parameters under various moisture contents.

It has also been shown that the water barrier between the cellulose crystal surface and the cell wall matrix can be irreversibly compromised, but at what moisture content is this barrier breached to allow the matrix to associate directly with the cellulose. The moisture content at which this occurs could be investigated by preparing a range of wood specimens dried from a green state to accurately known moisture contents and including differing numbers oven drying cycles.

It has been suggested in this thesis that one of the drivers for changes to the hydrophobicity of the cellulose crystallites when dried was due to the conformational change of the cellulose surface crystals from *gt*/*gg* to a cellulose crystal interior-like *tg* conformation. This could be tested by the use of proton resonance spin editing (PRSE) of ^{13}C CP-MAS NMR experiments to focus on the NMR resonances originating from the cellulose C4 (Newman and Hemmingson 1994). The cellulose C4 resonance is split into peaks that represent the interior (*tg*) and surface (*gt/gg*) cellulose chains. It would be expected that changes to the cellulose crystal surfaces to an interior-like conformation would translate to a shift in the proportions of C4-surface and C4-interior NMR resonances.

A practical outcome, of the new knowledge of the structure of the hydrated wood cell wall and changes to cellulose crystallite structure with changes in cell wall moisture content, could be the design and implementation of novel wood drying, and perhaps wood cell wall modification technologies.

7.3 References

Newman, R.H., Hemmingson, J.A. (1994) Carbon-13 NMR distinction between categories of molecular order and disorder in cellulose. Cellulose. 2:95-110

Appendix A – General sampling procedures for obtaining specimens of *Pinus radiata*

A.1 Sampling procedures

All specimens of *Pinus radiata* wood were taken from the SSE (150°) face of mature tree stand grown in Rotorua in the North Island of New Zealand (41° 55' S, 176° 16' E, 280 m a.s.l.) at an approximate height of 1.3 m (Figure A.1).

Figure A.1 *Example of sampling position of wood specimens.*

The outer bark was first removed using a chisel followed by removal of the outer cambial tissue layer until the woody tissue was revealed. Then a cut approximately 3 mm deep was made and a strip of wood *ca.* 20 mm wide and 50-60 mm long was excised (Figure A.2).

Figure A.2 *Representative sampling area of exposed woody tissue, ca. 20 x 50-60 mm.*

All specimens were immediately placed in a container of distilled water. The specimens were soaked in fresh distilled water for 24 hours with one further exchange of the distilled water to remove the water-soluble cell wall components present.

The wet specimens were separated using a scalpel into earlywood and latewood bands, the latewood typically appearing significantly darker than the earlywood. This sectioning was carried out while maintaining the specimens in a bath of distilled water. Small sub-specimens of these sections were confirmed as predominately earlywood or latewood using field emission scanning electron microscopy (FESEM).

Specimens were prepared for FESEM by first drying in air for 2 hours, followed by drying under vacuum for a further hour. Field-emission scanning electron microscope (FESEM) images were obtained using a Jeol JSM-6700F instrument. Specimens were fastened onto a support with a 12 mm diameter disc of carbon tape. The support and the specimens were coated with chromium under a $10^{-4}/10^{-3}$ mbar vacuum and images were acquired with an accelerating voltage of 3 kV.

In a partial tree ring FESEM micrograph the earlywood can be seen at the top and the latewood at the bottom of Figure A.3.

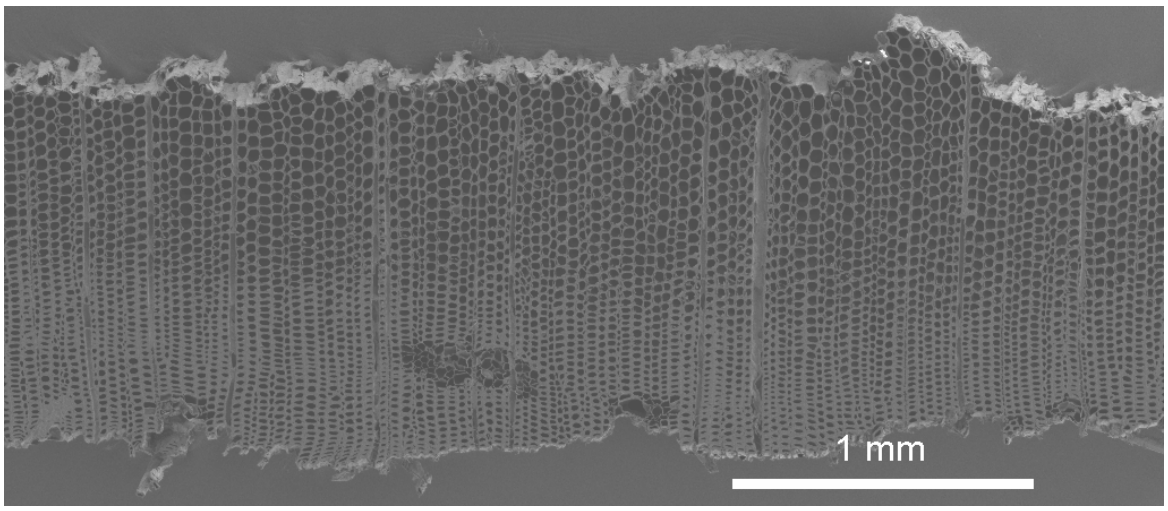

Figure A.3 *Partial tree ring from a mature Pinus radiata tree taken at 1.3 m with earlywood at the top and latewood at the bottom (25 x magnification).*

Latewood material was chosen for this study due to its higher proportion of cell wall relative to total volume. The earlywood has a larger overall cell diameter but a much thinner cell wall compared to latewood (Figure A.4).

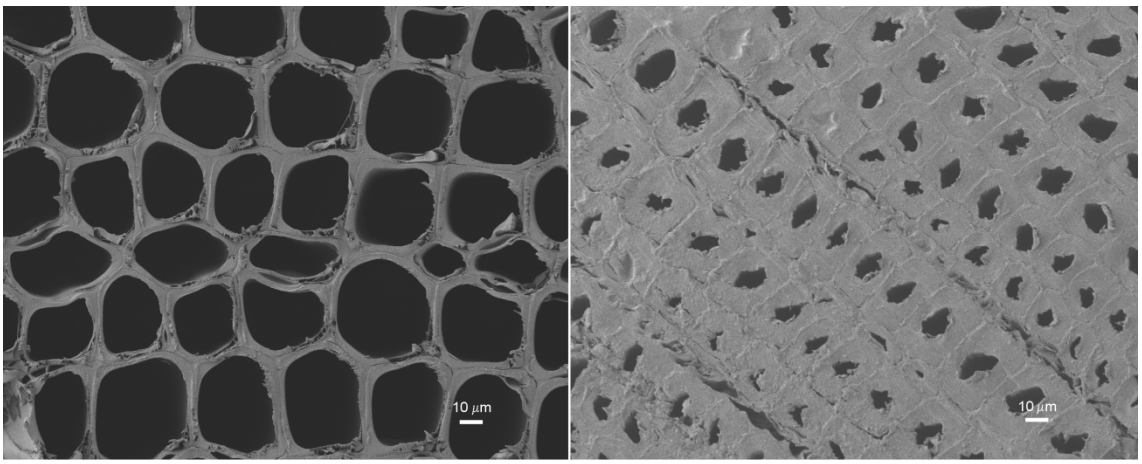

Figure A.4 *Examples of earlywood (left) and latewood (right) (500x magnification).*

Latewood is has been defined as those wood cells where the double radial cell wall thickness (DRW, lumen to lumen cell wall thickness) is equal to or exceeds the diameter of the lumen diameter (LD) (Mork 1928) (Figure A.5).

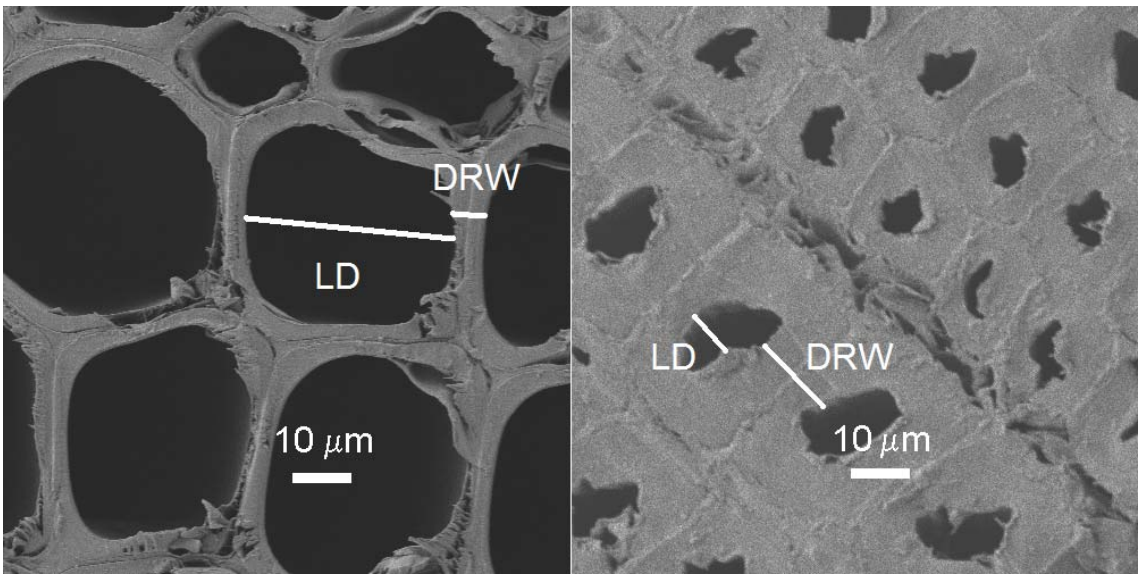

Figure A.5 *Earlywood (left) and latewood (right) determination by the application of Mork's definition (LD = lumen diameter, DRW = double radial cell wall radial thickness, 500x magnification).*

Latewood is then defined as when the ratio of DRW / LD ≥ 1. The example cells chosen in Figure B.5 result in for earlywood (LD = 33 μm and DRW = 6 μm) a ratio of 0.2, and for latewood (LD = 8 μm and DRW = 14 μm) a ratio of 1.8. Due to the non-uniform shape of cells, cell wall thicknesses, and lumen diameters even between cells in direct contact with each other, at best this method gives an arbitrary cut-off point for the identification earlywood *vs.* latewood.

Latewood and earlywood sections were then cut into specimens 15 mm to 20 mm wide, 40 mm in length, and 2 mm thick. One specimen of latewood was cut to same width and length as given above, but was cut on the diagonal along the face to give thicknesses varying from 3 mm at the top to 1 mm at the bottom (see Appendix C.5).

All specimens were stored in a Schott bottle filled with distilled water, and kept in a refrigerator at 4 °C until needed.

A.2 References

Mork, E. (1928) Die qualitat des fichtenholzes unterbesondere rucksicht nahme auf schied- und papierholz. Papier Fabrikant. 48:741-747

Appendix B – Preliminary synchrotron X-ray analysis

B.1 Initial synchrotron studies at the Stanford Synchrotron Radiation Laboratory (SSRL), U.S.A.

A scoping study was carried out by Dr Bridget Ingham from the New Zealand Synchrotron Group Ltd on the author's behalf. This work was carried out at the Stanford Synchrotron Radiation Laboratory (SSRL), the U.S.A. The objective of this study was to test an encapsulation method based on commercial Kapton® adhesive tape.

Six specimens were provided, three of never-dried *Pinus radiata* wood, and one each of each air-dried, oven-dried, and oven-dried, subsequently rewet *Pinus radiata* wood. The specimens of wood were a random mixture of late and earlywood (refer to Appendix A for sampling details). Each specimen was approximately 10 mm square and 2 mm thick. They were encased in Tesa® 51408 tape prior to leaving New Zealand. As detailed in Chapter 2, Tesa® 51408 tape is a self-adhesive Kapton® tape commonly used in high temperature masking applications.

The specimens were analysed on "Beamline 11-3" operating with a wavelength of 0.9752 Å collecting a diffractogram over a range of $1<Q<6$ Å^{-1}. Each specimen had data collected for 10 seconds and 10 scans were taken and averaged together. The specimens were orientated so that the (200) reflections were in the direction of the beam-stop arm. Diffractograms were transformed into polar coordinates and the Kapton® background subtracted. A slice of the polar coordinates was then taken and the scattering converted from units of Q (= $2\pi/d$, Å^{-1}) as supplied into diffraction angles (2θ, degrees).

The ($1\bar{1}0$), (110), and (200) diffraction peaks can clearly be seen (Figure B.1), although they are considerably broadened as compared with the simulation or the algal cellulose (refer to Chapter 2, Figures 2.8 & 2.10). The results showed that synchrotron based X-ray radiation provided excellent signal to noise. However, interpretation of the results in terms of moisture content showed little differences between the specimens. The explanation for this lay in the time between the transport of the specimens from New Zealand to the USA, and the analysis time was approximately two months. Hindsight

would indicate that the specimens had undergone some degree of drying and consequently the cell wall hydration state reorganised over this period.

The study showed that the Tesa 51408 tape proved no obstacle to obtaining excellent X-ray diffractogram in transmission mode, but also suggested that specimens should not be encapsulated until closer to the time of the WAXS experiment.

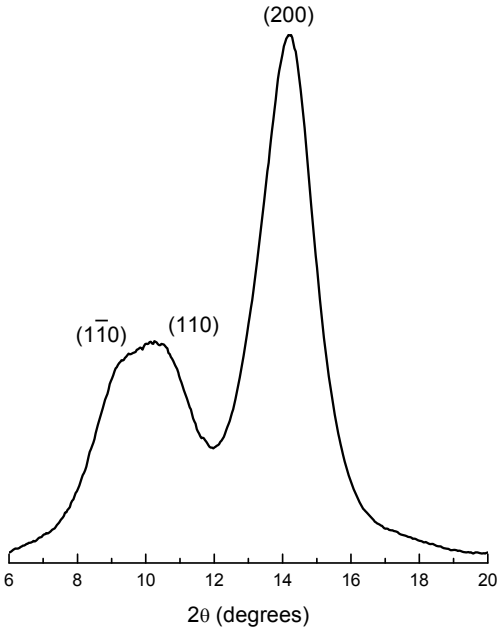

Figure B.1 *X-ray diffraction pattern of air-dried wood (specimen 10) obtained from the Stanford synchrotron.*

Appendix C - WAXS methodology development

C.1 Reproducibility of X-ray diffractograms within specimen

Each diffractogram presented represents an average of 25 individual diffractograms acquired from each specimen. The 25 diffractograms were obtained using a 5 x 5 rastered grid with spacings of 1 mm between each sampling point (specimen **1a**, Figure C.1).

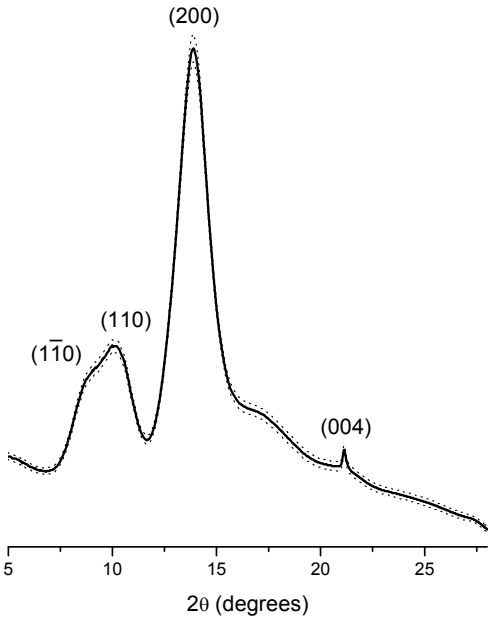

Figure C.1 *Average diffractogram of 25 points taken from a specimen of never-dried latewood (specimen **1a**, dotted lines = 95% C.I.).*

The error in 2θ was estimated by taking the centre of the (200) peak and measuring the deviation of the apex between diffractograms of the never-dried latewood specimen **1a**. This gave a negligible error of *d*(200) = 0.393*8* ± 0.000*1* nm (95% C.I.) when calculated from all 25 diffractograms obtained for the specimen. For the same (200) peak the intensity of the signal varied by 2.2%. The variation in peak intensities is most noticeable in the areas under which the water peaks are located indicating that some of the intensity variation is due to slight differences in moisture content across the specimen.

Averaging 25 diffractograms, however, gave no significant improvement in signal to noise ratio as compared with a single shot diffractogram. This result showed the quality of the Australian synchrotron optics and detector (specimen **1a**, Figure C.2).

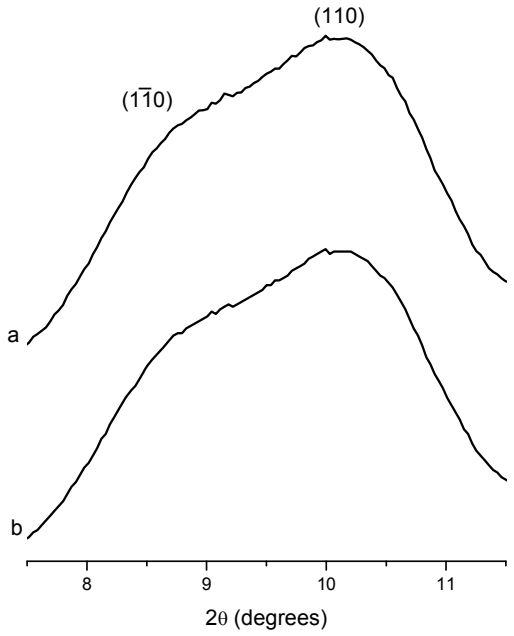

Figure C.2 *Expansion of a diffractogram of never-dried latewood (specimen **1a**) showing no significant improvement in signal to noise between (a) a single diffractogram and (b) an average of all 25 diffractograms taken from a single specimen.*

Even so, averaging over a wider area than a single X-ray shot, with beam dimensions of 200 µm x 100 µm, it was important to avoid experimental artefacts caused by the possibility of abnormal wood cell walls, *i.e.* those cells that do not represent the average due to physical damage for example. From SEM examination of wood specimens, it has been shown (Appendix A) that the wood cell diameters are *ca.* 40 µm x 30 µm, meaning that the synchrotron X-ray beam strikes 16 to 17 latewood cells. By taking an average of 25 diffractograms, over 400 wood cells are used, averaging out local differences in cell wall orientation and composition.

C.2 Investigation of X-ray damage to wood specimens

It has been previously reported that X-rays interact with water in wood and produce hydroxyl radicals that may damage or change the cellulose crystal structure (Muller 2008). To investigate this as a potential source of artefact in this study, a specimen of never-dried wood encased in Kapton® was subjected to multiple 1-second X-ray exposures on the same sampling spot, and the resulting diffractograms were collected during each exposure. One hundred exposures were used with a 1-second interval between each exposure. The resulting diffractograms for the 1st, 25th, 50th, 75th, and 100th exposures is given as Figure C.3 (specimen **1a**).

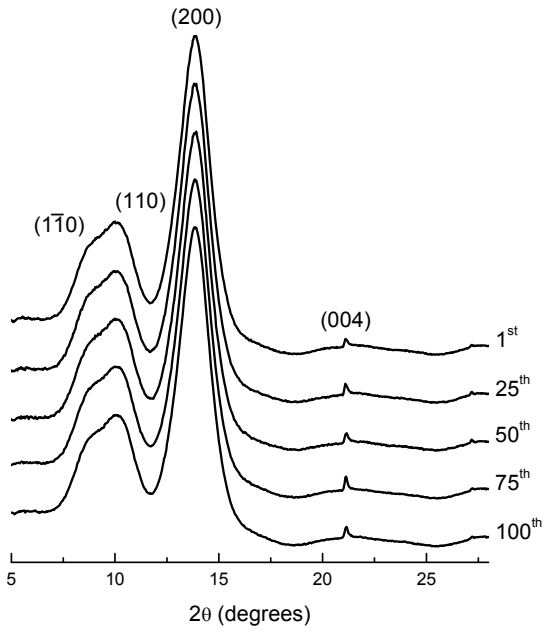

Figure C.3 *Multi-shot X-ray experiments showing no significant change to diffractograms over 100 individual one second X-ray exposures (specimen **1a**, normalised).*

There was no significant change in the diffractograms from the 1st to the 100th exposure of the specimen to the X-ray beam observed. This can be seen in the scatter plot of the WAXS diffractogram intensities relative to each other. The diffractogram from the 1st exposure correlates with all of those preceding to a high degree (Figure C.4).

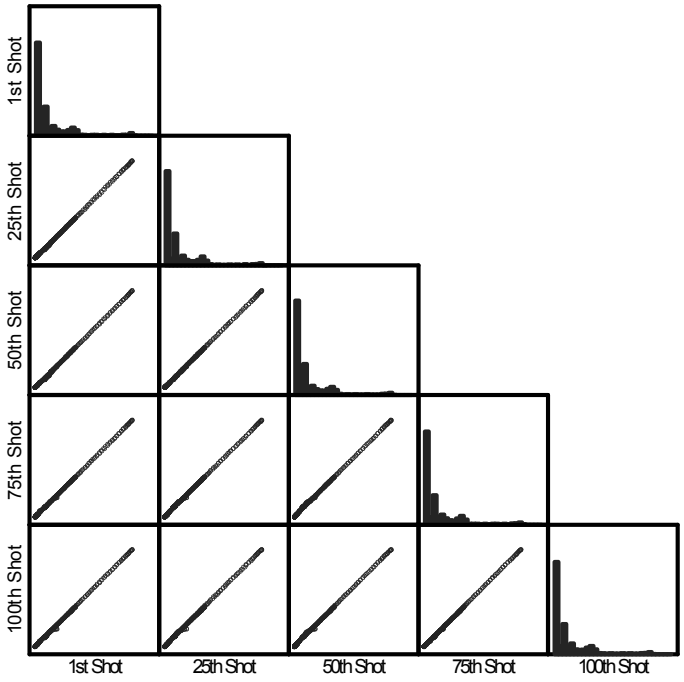

Figure C.4 *Scatter plot of multi-shot X-ray experiment.*

The diffractograms presented in the main body of the thesis are the result of an average of 25 one 1-second X-ray exposures. The 25 exposures are rastered in a 5 by 5 grid so that each exposure is sampling different point on the specimen. Any changes seen in the diffractograms are therefore due to experimental perturbations not to X-ray induced damage or modification to the cellulose crystal structure.

C.3 *In situ* air-drying of a never dried wood specimen

A specimen of never-dried wood (specimen **1a**) was adhered to a piece on Kapton® tape only on one side to allow air-drying to occur. This specimen was then placed on a weighing balance (Mettler Toledo, PB1501-L, 1 decimal place accuracy) in then exposed to the X-ray beam, and diffractograms were collected at 1-minute intervals for approximately 12 hours. Sampling points were rastered over a 12 x 12 grid (144 sampling points) spaced 1 mm apart. Due to the level of accuracy of the weighing balance differentiation of the %MC was not possible between the last two moisture contents, these values are marked with an asterisk. The initial %MC was 126% measured 1 minute after placement on the specimen holder. After 44 min, the %MC was 103%, after 2 hr 02 min 58%, after 7 hr 24 min 13%*, and after 14 hr 38 min 13%* (Figure C.5). A temperature of 25 °C was recorded in the X-ray hutch although the relative humidity was unknown. The changes in the diffractograms seen to occur were similar to those seen for the air-dried specimen prepared beforehand in New Zealand, showing a migration of the $(1\bar{1}0)$ and (110) peaks towards each other.

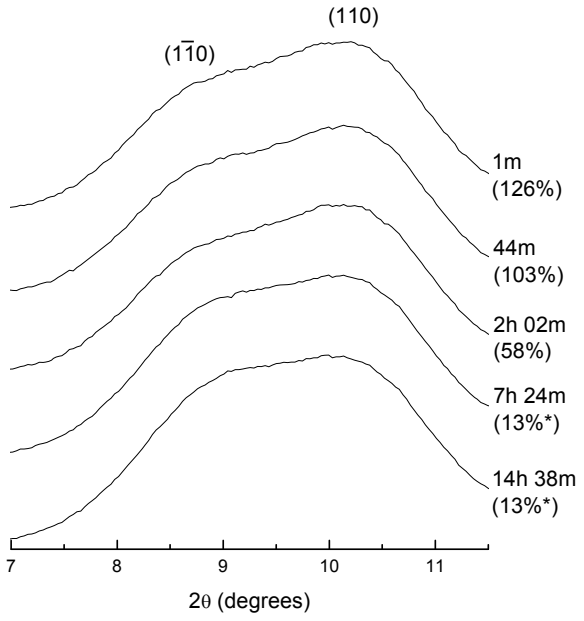

Figure C.5 *Specimen of never-dried wood air-drying overnight (specimen **1**, normalised).*

Over the time of the experiment, the diffraction peak associated with water could be seen to decrease as air-drying progressed (specimen **1**, Figure C.6).

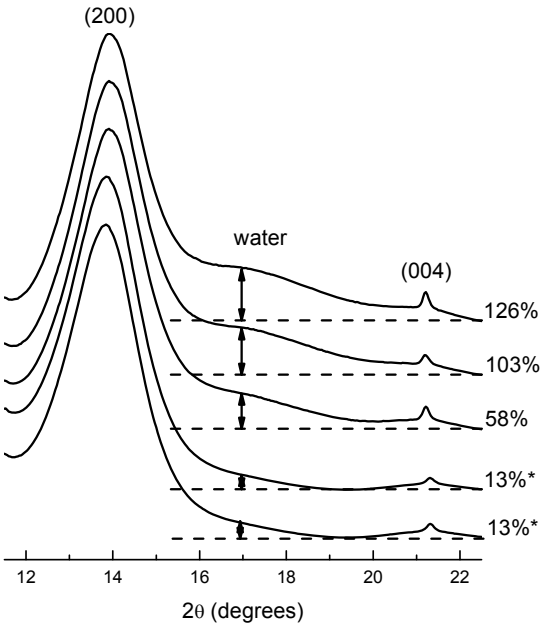

Figure C.6 *In-situ air-drying of never-dried wood monitored by X-ray diffraction. * Due to the level of accuracy of the weighing balance differentiation of the %MC was not possible (specimen **1**, normalised).*

One noticeable effect of the drying process is the decrease in the intensity of the water peak. The water peak due to its broadness overlaps with that of the cellulose (200) peak. This overlap may in part be the cause of the observed shift to lower 2θ values of the (200) cellulose peak on drying, rather than entirely actual changes to the *d*-spacing of the (200) plane as previously reported by Sugino (Sugino et al. 2007) (specimen **1**, Figure C.7).

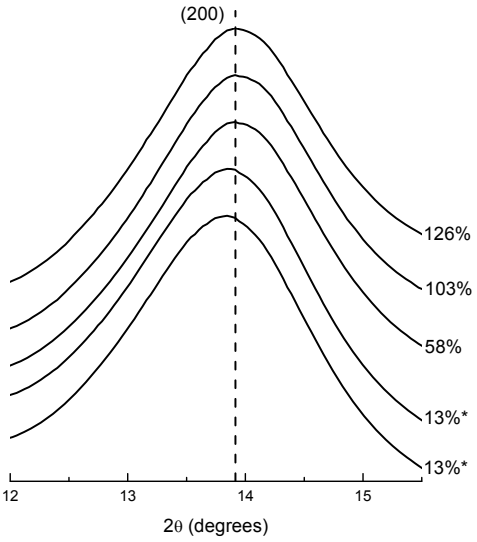

Figure C.7 *Cellulose (200) peak showing a shift to lower 2θ values on air-drying (specimen **1**, normalised).*

C.4 X-ray diffractograms of Latewood and Earlywood

Latewood was chosen as the specimens most likely to give the best signal to noise for both X-ray and NMR experiments due to having the largest amount of cell wall material per unit volume. X-ray (Nomura and Yamada 1972) and NMR (Newman 2004) studies have shown that other than compositional amounts of cell wall components, there was no difference in the cellulose crystals between latewood (LW) and earlywood (EW). Two specimens each of both never-dried latewood (specimen **1a**) and never-dried earlywood (specimen **C1**) taken from different trees were analysed. No significant difference in positions or shape of the $(1\bar{1}0)$, (110), or (200) cellulose peaks, however, the EW shows a slightly worse signal to noise (Figure C.8), satisfying the conclusion that cellulose crystallinity is invariant between earlywood and latewood in never-dried wood material.

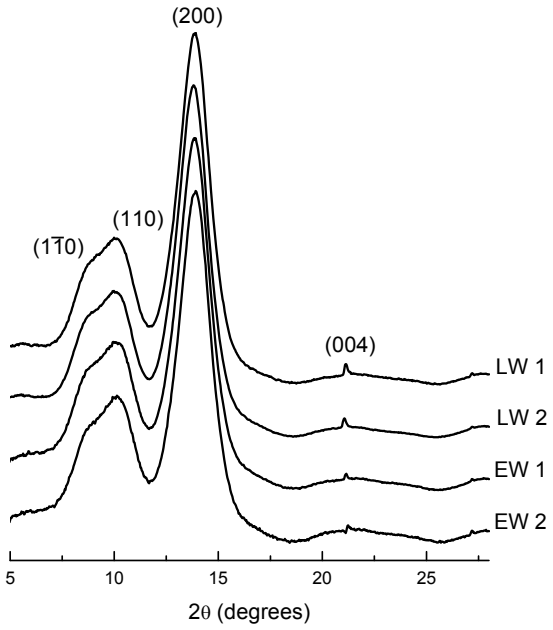

Figure C.8 *Diffractograms of specimens of never-dried latewood (specimen **1a**, LW 1 & LW 2) and never-dried earlywood (specimen **C1**, EW 1 & EW 2) (normalised).*

C.5 Effect of specimen thickness

The synchrotron source of X-ray radiation allowed the analysis of not only wet specimens but also of specimens millimetres thick. The effect of specimen thickness was examined using two different thicknesses, 1 mm and 3 mm. This was carried out on a single never-dried specimen that had been cut on a diagonal giving varying thickness from top to bottom (specimen **2**). No significant difference other than signal intensity was observed for the cellulose $(1\bar{1}0)$, (110), (200), or (004) peaks between the

two specimen thicknesses (Figure C.9). Although specimens were carefully prepared to have a uniform thickness of 2 mm, it would seem that this is not a necessary requirement when using a synchrotron light source.

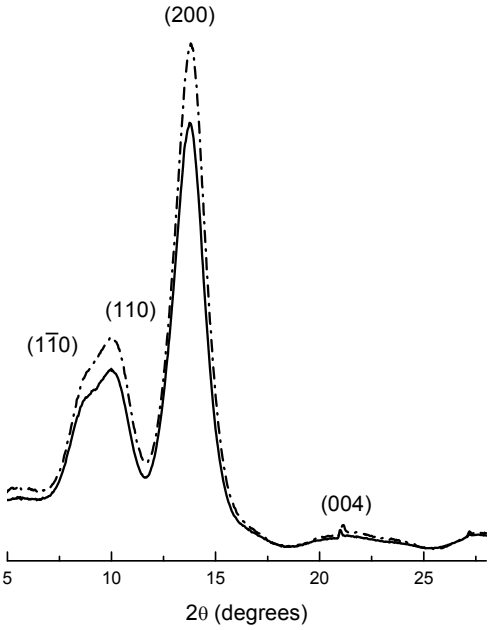

Figure C.9 *Diffractogram of never-dried wood (specimen **2**) cut at thicknesses of 1 mm (solid line) and 3 mm (dashed–dotted line).*

Even with a specimen thickness of 2 mm there would still be an expected parallax error due to diffractions originating from the edge closest the X-ray beam hitting the detector at a different 2θ value from those originating on the outer edge of the specimen. The detector was located 250 mm from the specimen and 2θ values were calculated based on this distance. However, the specimens, being 2 mm thick, meant diffractions occurred from distances of 250 mm to 248 mm from the detector (i.e. 249 mm ± 1 mm). The (200) peak for a never-dried specimen was found to occur at a 2θ value of 13.9104°, based on a specimen distance of 250 mm from the detector. Using 248 mm as the distance to the detector, the same (200) peak would give a 2θ value of 13.8034°. This has the effect of broadening the (200) peak by *ca.* 0.1° and giving a range of possible *d*-spacings for the *d*(200) from 0.394 nm to 0.397 nm, although the apex could be determined to better than ±0.001 nm. Variations in specimen thicknesses were estimated to be no more than ±0.2 mm, so these introduced an uncertainty smaller than ±0.001 nm. The error in calculated *d*-spacings was therefore taken as ±0.002 nm.

C.6 Effect of thermal treatment

At temperatures of *ca.* 100 °C, the components of the matrix soften (54 °C – 142 °C, hemicellulose; 77 °C – 128 °C, lignin), unlike cellulose (222 °C – 250 °C) (Nakano 2005). To examine at the effects of softening of the matrix on the cellulose crystallites without the influence of drying, specimens were boiled in water.

Four never-dried specimens were boiled in 250 mL of water for 3 hours. After this time, two specimens were removed and placed immediately into an ice bath. The other two specimens were allowed to cool to room temperature. One each of the specimens which had been quench-cooled (specimen **C3**), and one of the specimens which had been allowed to slowly cool to room temperature (specimen **C4**) were then allowed to air-dry for 3 days at 23 °C and 42-46% relative humidity. After this time, the air-dried specimens were rewet to saturation by immersion in water. See Table 2.1 (Chapter 2) for a list of specimens.

Never-dried (specimen **1a**) and boiled wood (specimen **C2**) specimens that were not allowed to dry showed no significant difference in their diffractograms (Figure C.10). This indicated that a processing of softening and then re-setting of the matrix components does not cause or allow the cellulose crystallites to change conformation.

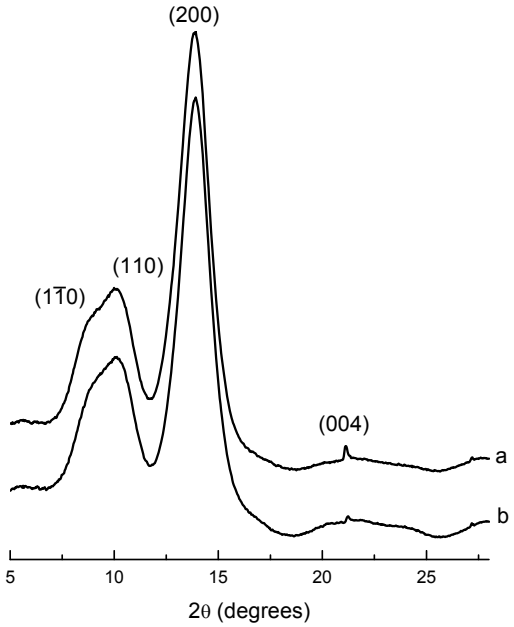

Figure C.10 *(a) Never dried wood (specimen **1a**) and (b) never dried wood boiled (specimen **C2**) in water for 3 hours (normalised).*

No significant differences in the obtained diffractograms for air-dried specimens of wood (specimen **3**), boiled wood (specimen **C4**), and ice cooled boiled wood (specimen

C3) were observed (Figure C.11 a, b & c). Likewise air-dried specimens of wood, boiled wood, and ice cooled boiled wood when rewet showed similar diffractograms (Figure C.11 d, e & f). Again, either subjecting wood to temperatures at which matrix components soften then slow or fast cooling followed by air-drying or air-drying and rewetting had no significant effects on the cellulose crystallites (Figure C.11).

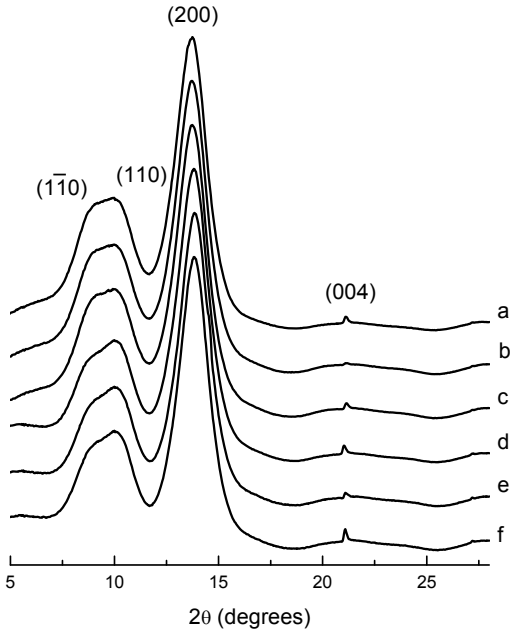

Figure C.11 *(a) Air-dried wood (specimen **3**), (b) air-dried boiled wood (specimen **C4**), (c) air-dried boiled wood quench cooled in ice (specimen **C3**), (d) rewet air-dried wood (specimen **3a**), (e) rewet air-dried boiled wood (specimen **C4**-rewet), and (f) rewet air-dried boiled wood quench cooled (specimen **C3**-rewet) (normalised).*

C.7 Glycerol preservation of never-dried wood specimens

Glycerol replaces the water, but unlike water, it does not undergo significant evaporation at ambient temperatures, thus keeping the wood cell walls in a swollen state and thereby conserving the specimen. This approach was investigated for the maintenance of wood cell wall turgidity of specimens for international travel, such as in our case Trans-Tasman, for the synchrotron studies. Glycerol has been reported to maintain *Pinus sylvestris* cell walls in a swollen state after vacuum drying, and glycerol was found to be superior to polyethylene glycol (PEG 200 and PEG 1500), or pentaerythritol (Wallstrom and Lindberg 1999).

To test this, a specimen of never-dried wood was soaked in 100 mL of glycerol (ReagentPlus®, Sigma-Aldrich®) overnight, and then the glycerol was exchanged for a fresh 100 mL and then left for a further 6-hour soak period. After this time, the

specimen was removed and excess surface glycerol blotted. The specimen was then placed in a sealable plastic bag.

Glycerol-soaked never-dried wood (specimen **C5**) showed a diffuse halo of glycerol in a similar position to that of the (200) reflection from cellulose (Figure C.12). As the glycerol diffraction appeared as an isotropic band in the diffractogram, it was possible to carry out background subtraction as used previously (*i.e.* 90° to grain minus 60° to grain).

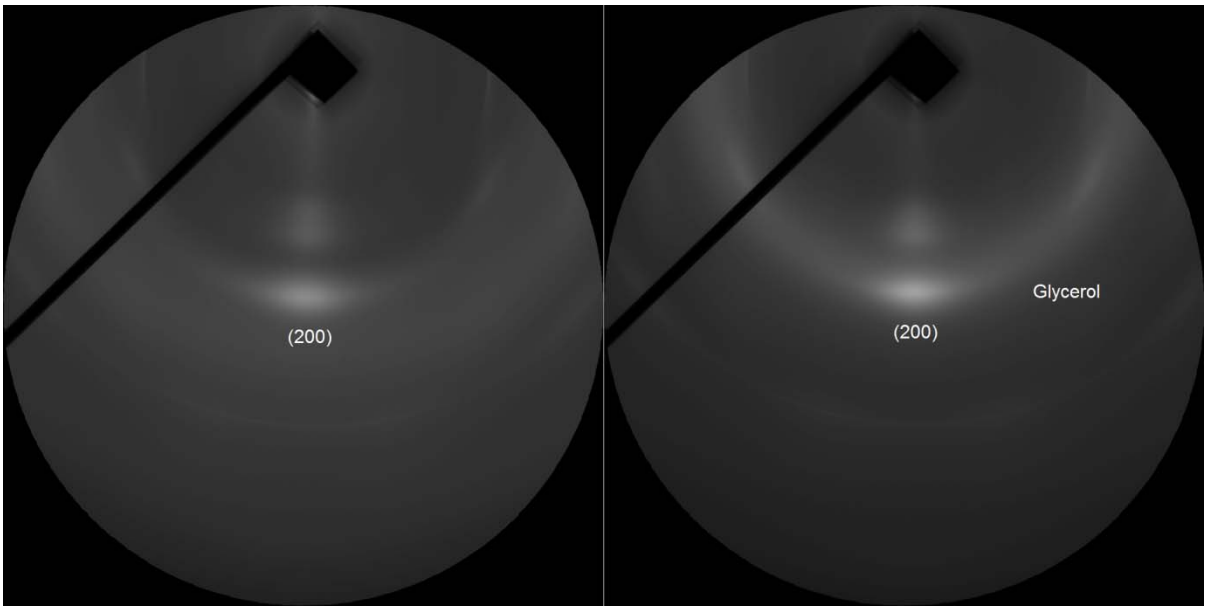

Figure C.12 *WAXS diffractograms of (left) never-dried wood and (right) glycerol soaked never-dried wood (specimen **C5**).*

Figure C.13 shows diffractograms of glycerol soaked wood orientated 60° and 90° with respect to the direction of the grain. The diffractogram orientated 60° to the grain shows a broad peak centred on a 2θ value of 13.0°.

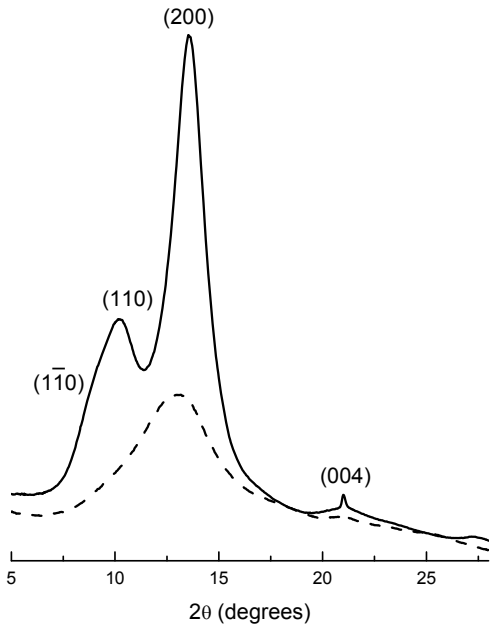

Figure C.13 *WAXS diffractogram of wood soaked in glycerol (specimen **C5**, 60° to grain = dashed line, 90° to grain = solid line).*

The X-ray diffractogram of glycerol soaked never-dried wood showed significant differences when compared to never-dried wood. A depression of the intensity of the (1$\bar{1}$0) peak and a shift of the (200) peak to a lower 2θ value can be seen (Figure C.14). The reasons for this shift are unknown, but may either be due to a consequence of a change in cellulose crystal structure, or maybe due to the glycerol background not being isotropic, and creating an artefact when subtracted.

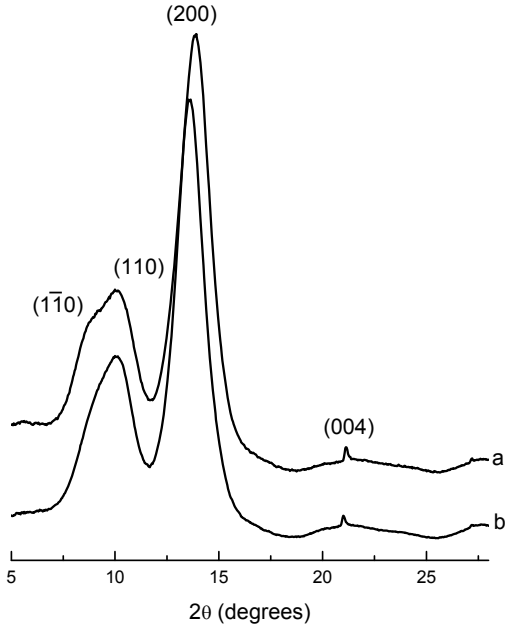

Figure C.14 *(a) Never-dried wood (specimen **1a**) and (b) glycerol soaked never-dried wood (specimen **C5**) specimens (normalised).*

Glycerol treatment of wood specimens, while an appropriate to keep wood cell walls in a swollen state, has an undesirable effect on the cellulose diffractogram. Glycerol therefore is not appropriate as a preservation chemical for green wood specimens destined for X-ray studies.

The method presented in the main body of the thesis of wrapping never-dried specimens in wet cotton, then placing in a sealable plastic bag was concluded to be the preferred method for the preservation of the green state for wood specimens in a form suitable for international travel.

C.8 References

Muller, M. (2008) Radical formation in wood by X-ray interaction with water. Hill, S.J. Auckland, New Zealand, 3rd New Zealand - German Cell Wall Symposium

Nakano, T. (2005) Effects of quenching on relaxation properties of wet wood. Journal of Wood Science. 51:112-117

Newman, R.H. (2004) Homogeneity in cellulose crystallinity between samples of *Pinus radiata* wood. Holzforschung. 58:91-96

Nomura, T., Yamada, T. (1972) Structural observation on wood and bamboo by X-ray. Wood Research. 52:1-12

Sugino, H., Sugimoto, H., Miki, T., Kanayama, K. (2007) Fine structure changes of wood during moisture adsorption and desorption process analyzed by x-ray diffraction measurement. Mokuzai Gakkaishi. 53:82-89

Wallstrom, L., Lindberg, K.A.H. (1999) Measurement of cell wall peneration in wood of wtaer-based chemicals using SEM/EDS and STEM/EDS technique. Wood Science and Technology. 33:111-122

Appendix D – Alternative explanation of the presence of cellulose IV_I in red meranti (*Shorea* spp.*)*

D.1 Cellulose IV_I in red meranti (*Shorea* spp.)

During wood specimen drying, the most significant changes seen in the WAXS diffractograms show hydrogen bonding within cellulose sheets (*b* unit cell dimension) and of unit cell angle, *γ* (refer to Chapter 2, Figure 2.20). The effect of a decrease in the angle *γ* in the cellulose I unit cell is to create a structure closer to that of cellulose IV_I with a *γ* of 90° (Gardiner and Sarko 1985). It has been suggested that cellulose IV_I does not exist, but may be just an extreme structural variation of cellulose Iβ (Okano and Koyanagi 1986; Newman 2008). A study of red meranti wood concluded that the form of cellulose present was cellulose IV_I (Nishimura et al. 1982). Nishimura *et al* concluded the presence of cellulose IV_I based on the ratio of (002) to (004) peak intensities and the observation of no cellulose I $(1\bar{1}0)$ and (110) peaks in their diffractogram. However, oven-dried specimens presented in this thesis of cellulose I show a similar diffractogram profile to that of cellulose IV_I offered by Nishimura (refer to Figures 2.14a & 2.20b, Chapter 2). A peak integral ratio [R = integral(002) / integral(004) for diffractograms parallel to the grain] of 0.26 was obtained for a never-dried wood specimen (Figure D.1).

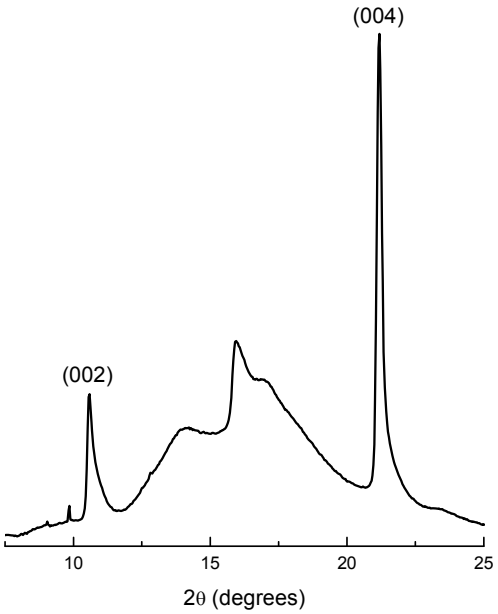

Figure D.1 *Diffractogram of never-dried wood along the direction of the grain.*

A comparison of the R value and unit cell angles (γ) obtained in this study with those found previously (Nishimura et al. 1982) is presented as Table D.1.

Table D.1 *Values of R [intensity (002) / intensity (004)] and γ the unit cell angle (Nishimura et al. 1982).*

Specimen	*R*	*γ (°)*
Cellulose I	0.03	97
Cellulose II	0.5	117.2
Cellulose III_I	2.0	121.9
Cellulose III_{II}	0.5	121.1
Cellulose IV_I	0.12	90
Cellulose IV_{II}	0.66	90
Akamatsu	0.05	≠ 90
Red meranti	0.12	= 90
Never-dried *Pinus radiata* [a]	0.26	99.2
4x oven-dried *Pinus radiata* [a]	---	96.8

a = data from this thesis (Table 2.3)

The R value obtained in this thesis is seen to be significantly different than that reported for cellulose I bringing into doubt the robustness of the R parameter for determination of cellulose in non-ideal specimens. The (002)/(004) ratio (R) has been considered similar in the case of cellulose I and cellulose IV_I (Hayashi et al. 1975), again making R determination not a definitive method of identification of cellulose form. It can also be seen that the unit cellulose angle (*γ*) is subject to variation in heterogeneous systems and that it decreases during the drying process.

Diffractograms for cellulose I obtained in this thesis when compared to the diffractogram of red meranti reported by Nishimura suggests that rather than the presence of cellulose IV_I being the only conclusion, there is an alternative explanation, that of the presence of a dehydrated form of cellulose I in the red meranti specimen used. No indication is given by Nishimura of the moisture history of the specimen. None of the observed features ascribed to cellulose IV_I as the form of cellulose in red meranti cannot be also explained in terms of dehydrated cellulose I.

This present result further supports the conclusion that cellulose IV_I is an artefact derived from an extremely dried wood material, and further reinforces the conclusion that the moisture-content history of wood specimens used for cellulose crystallinity study is important.

D.2 References

Gardiner, E.S., Sarko, A. (1985) Packing analysis of carbohydrates and polysaccrides. 16. The crystal structures of celluloses IV_I and IV_{II}. Canadian Journal of Chemistry. 63:173-180

Hayashi, J., Sufoka, A., Ohkita, J., Watanabe, S. (1975) The confirmation of existences of cellulose III_I, III_{II}, IV_I, and VI_{II} by the x-ray method. Polymer Letters Edition. 13:23-27

Newman, R.H. (2008) Simulation of X-ray diffractograms relevant to the purported polymorphs cellulose IV_I and IV_{II}. Cellulose. 15:769-778

Nishimura, H., Okano, T., Asano, I. (1982) Fine structure of wood cell walls III. On the natural occurence of cellulose IV_I in red meranti. Mokuzai Gakkaishi. 28:484-485

Okano, T., Koyanagi, A. (1986) Structural variation of native cellulose related to its source. Biopolymers. 25:851-861

Appendix E – Efficiency of the exchange of protons with deuterons in wood

E.1 Introduction

The introduction of a spin diffusion barrier was a requirement for the NMR experiments. Presence of water allows very rapid spin diffusion, both providing a “flip-flop” network and also by physical diffusion of the water molecules themselves. It was therefore necessary to replace the water with deuterated water in order to create a proton diffusion spin barrier. An experiment was carried out to investigate the conditions for isotropic exchange. The goal was to replace the water that occurs in the cell wall not just the water present in the lumens.

E.2 Experimental

All experiments were carried out on a Bruker Avance DRX200 (^{1}H 200.13 MHz) and analysed using a standard proton NMR pulse sequence (tip angle 30^o, recycle decay 1 s, 4 transients). Into a 10 mm NMR tube a stick of never dried of *Pinus radiata* (1.2394 g) was placed (Figure E.1) and the proton NMR spectrum recorded. The integral of this peak was set to 100. To this tube 5.6594 g of D_2O was added, and the sample was observed at intervals over a time period. After certain times the resulting H_2O/D_2O mixture was decanted and replaced by fresh neat D_2O. This gave fresh D_2O replacement times of 100, 164 (4.2829 g), 245 (4.3214 g), and 1539 minutes. At the end of this time the solution was decanted and the NMR signal of the wood alone was measured.

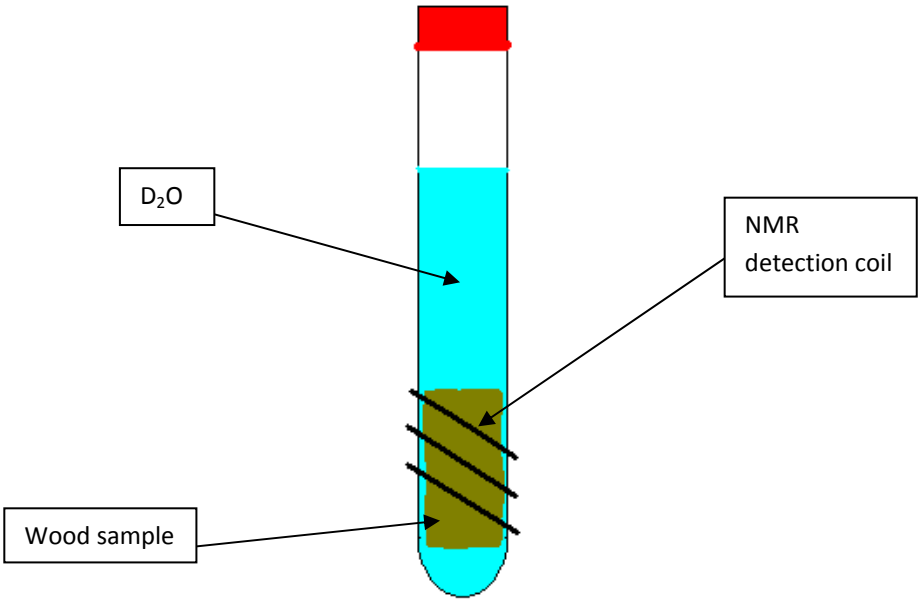

Figure E.1 *Experimental setup for the monitoring of D_2O exchange in wood.*

E.3 Results and Discussion

The H_2O initially contained in the wood structure was over time diluted by the process of diffusion, and mixes with liquid outside the NMR coil. This appeared as a reduction in the proton NMR signal (Table E.1 and Figure E.2).

Table E.1 *Decrease in H_2O proton intensity of a never-dried wood sample soaked in D_2O.*

Time (min)	H_2O/HDO (integral)
0**	100.00
2	94.13
4	88.51
9	81.79
16	75.09
25	69.61
36	65.75
49	62.33
64	59.69
81	58.49
100	56.91
100*	20.37
102	18.82
104	18.25
109	17.35
116	16.60
125	15.90
136	15.25
149	14.76
164	14.37
164*	5.11
245	3.58
245*	2.08
1295	1.52
1299	1.06
1419	1.00
1449	0.98
1539	0.09
1539**	0.02

*Solution was replaced with fresh neat D_2O.

**Wood sample with no solution present.

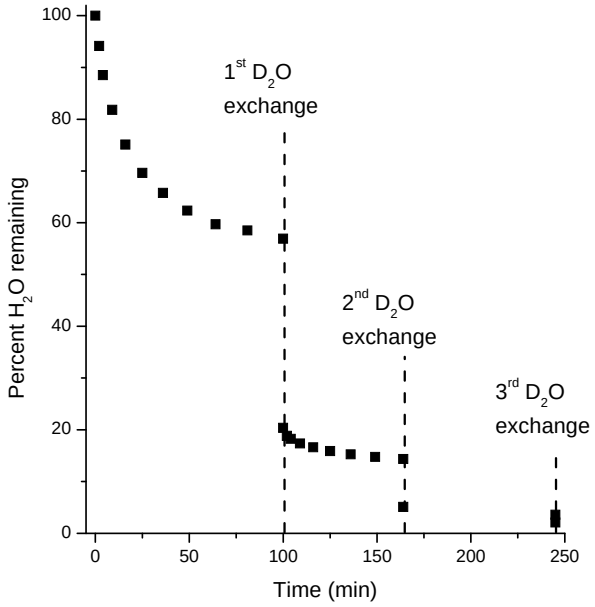

Figure E.2 *Proton NMR signal decrease of NDW in a D_2O solution, first ca. 4 hours.*

After analysis the sample was dried to constant weight at 105 ^oC (0.3153 g), from this the initial %MC of 293% was calculated (%MC = wet weight / dry weight x 100). After *ca.* 24 hours the NMR signal integral was 0.02 (compared with the original 100). The relationship that NMR proton signal integration is linear with proton concentration was applied (Equation E.1).

$$W_r = (I_f / I_i) \times W_w \qquad E.1$$

In this equation, W_r is the weight of the water remaining after some exchange time, W_w is the weight of water in the never-dried wood, I_i is the initial NMR signal integration before D_2O is added, and I_f is the final NMR signal integration after removal of D_2O/H_2O mixture, *i.e.* wood only.

Using this relationship with the data presented in Table E.1 the calculated remaining water wass;
(0.02 / 100) x 0.9241 g = 0.0002 g water remaining after approximately 24 hours with three exchanges of fresh D_2O during this time.

Fibre saturation point of the wood cell wall is usually taken to be 30% moisture content (Tiemann 1906), and this would translate to be 0.0946 g of water in this particular sample. The amount of water remaining in the sample was just a fraction (0.0002 g) of the calculated fibre saturation point. This would indicate that both lumen and cell wall water was undergoing D_2O exchange during the soaking period.

E.4 Conclusions

Proton solution state NMR was a simple method to monitor the removal of H_2O and replacement with D_2O in a never-dried wood specimen and showed that D_2O exchange was occurring not only in the lumen but also in the cell wall.

E.5 References

Tiemann, H.D. (1906) Effect of moisture upon the strength and stiffness of wood. Agricultural and Forest Service Bulletin. 70:82-84